

2011

Homodyne detection for laser-interferometric gravitational wave detectors

Tobin Thomas Fricke

Louisiana State University and Agricultural and Mechanical College, tobin.fricke@ligo.org

Follow this and additional works at: http://digitalcommons.lsu.edu/gradschool_dissertations



Part of the [Physical Sciences and Mathematics Commons](#)

Recommended Citation

Fricke, Tobin Thomas, "Homodyne detection for laser-interferometric gravitational wave detectors" (2011). *LSU Doctoral Dissertations*. 3623.

http://digitalcommons.lsu.edu/gradschool_dissertations/3623

**HOMODYNE DETECTION FOR LASER-INTERFEROMETRIC
GRAVITATIONAL WAVE DETECTORS**

A Dissertation

Submitted to the Graduate Faculty of the
Louisiana State University and
Agricultural and Mechanical College
in partial fulfillment of the
requirements for the degree of
Doctor of Philosophy

in

The Department of Physics and Astronomy

by

Tobin Thomas Fricke
B.S., University of California, Berkeley, 2003
M.A., University of Rochester, 2005

December, 2011

For my parents, who have always supported and encouraged me.

Acknowledgements

It has been a privilege to be a part of the nascent field of gravitational wave astronomy at this exciting time, perhaps at the cusp before an era of discovery. It would be impossible to properly acknowledge all of the great people I have encountered and who have influenced me during my time in graduate school, but I will nonetheless try to name the main characters.

Thank you to Adrian Melissinos, my advisor at the University of Rochester, for your energy and creativity, and for getting me involved with gravitational waves in the first place.

To Rana Adhikari, my mentor at Caltech and a driving force behind Enhanced LIGO, for showing me how to align the mode cleaner and cut the can off of photodiodes.

To Valery Frolov at LIGO Livingston, a tireless commissioner and uncompromising scientist, for mentoring me and for countless late night hours in the control room.

To Gabriela González, my advisor at Louisiana State University, for adopting me as a student and guiding me through the graduate school process with the utmost patience, and for letting us drink Jorge's whiskey.

And to Rai Weiss, a role model for us all.

Thank you also to my fellow graduate students and friends, among them Kate Dooley, Stefanos Giampapis, Ryan Dahl, Lisa Togler, Kris Yirak, Aimee Slaughter, Bree Lupia, Matthew Bryant, and Sarah DeRosier. To my cohort at LSU: Anamaria Effler, Ryan DeRosa, Chad Hanna, Jeff Kissel, Jake Slutsky, Rupal Amin, and Sarah Caudhill. To Rob Ward, Marie-Hélène, Jeff Smith, Dan Busby, Phil Willems, Steve Vass, and John Miller for making my stay at Caltech an enjoyable one. And to everyone else who worked on the Enhanced LIGO project or continues to work towards the detection of gravitational waves.

Finally, the boilerplate: this work was supported by the National Science Foundation under grant PHY-0905184. LIGO was constructed by the California Institute of Technology and Massachusetts Institute of Technology with funding from the National Science Foundation and operates under cooperative agreement PHY-0757058. This dissertation has LIGO Document number LIGO-P1000010.

Table of Contents

Acknowledgements	iii
List of Tables	vii
List of Figures	viii
Abstract	x
1 Introduction	1
1.1 Gravitational Waves	1
1.2 Generation of Gravitational Waves	3
1.3 The Hulse-Taylor Pulsar	4
1.4 Detectors	4
1.4.1 Laser Interferometers	4
1.4.2 Other Detectors	5
1.4.3 Detector Products	6
1.5 Sources of Gravitational Waves	6
1.6 LIGO	7
1.6.1 Summary of Changes Made for Enhanced LIGO	8
1.7 The Future	9
1.8 This Dissertation	10
2 The LIGO Detector	11
2.1 An Interferometric Gravitational Wave Detector	11
2.2 The Michelson Interferometer	12
2.3 Resonant Cavities	14
2.4 Michelson with Fabry-Perot Arms	15
2.5 Power Recycling	15
2.6 The Coupled Cavity Pole	15
2.7 Interferometer Sensing and Control	17
2.7.1 The Pound-Drever-Hall Technique	18
2.7.2 Generalization of the PDH Technique	19
2.8 Noises	20
2.9 Heterodyne Shot Noise	21

3	DC Readout	23
3.1	Principle of DC Readout	23
3.2	Motivation for DC Readout	25
3.3	Implementation of DC readout	26
3.3.1	Interferometer Lock Acquisition	28
3.4	Calculation of the Optical Gain	28
3.5	Selecting the DARM Offset	30
3.5.1	Decrease in Arm Power Due to Off-Resonance Operation	31
3.5.2	Decrease in Power Recycling Gain Due to Intentional Offset	31
3.5.3	Nonlinearity of the DC Error Signal	32
4	Output Mode Cleaner	34
4.1	Introduction	34
4.2	Physical Design of the Cavity	34
4.3	Requirements	36
4.4	Choosing the OMC Finesse	37
4.5	Choosing the OMC Length and Geometry	38
4.6	OMC Feedback Control Systems	38
4.6.1	Length Sensing and Control (LSC)	39
4.7	Input Beam Alignment Sensing and Control (ASC)	40
4.7.1	QPD Alignment	40
4.7.2	Dither Alignment	41
4.7.3	Drumhead Dither OMC Alignment System	41
4.8	Scattering	43
4.9	Beam Diverter	47
4.10	The Front End	47
4.10.1	Photodiodes	47
4.10.2	Electronics	47
5	DC Readout Performance and Noise Couplings	49
5.1	Sensitivity	49
5.1.1	Measured and Expected Sensitivity	50
5.2	Laser and Oscillator Noise Coupling Mechanisms	51
5.2.1	Laser Noises	54
5.2.2	Oscillator Noises	56
5.3	Laser and Oscillator Noise Coupling Measurements	57
5.3.1	Laser Noise Coupling Measurements	57
5.3.2	Oscillator Noise Coupling Measurements	60
5.4	Beam Jitter Noise	60
6	Conclusion	65
	Bibliography	66

Appendix A: Table of Abbreviations	74
Appendix B: Determination of LIGO Cavity Lengths and Mirror Reflectivities	76
B.1 Arm Length	76
B.2 Bandwidth	77
B.3 Test Mass Reflectivities	77
B.4 Power Recycling and the Recycling Mirror	78
B.5 Power Recycling Cavity Length	78
B.6 The Schnupp Asymmetry	79
Appendix C: Fabry-Perot Cavities	81
C.1 Fabry-Perot Field Equations	81
C.2 The Cavity Pole	82
C.3 Phase Gain	83
C.4 Intra-Cavity Power Buildup	85
C.5 Finesse (\mathcal{F})	85
C.6 Impedance Matching	86
C.6.1 Critically-Coupled Cavities	86
C.6.2 Over-Coupled Cavities	88
Appendix D: The Optical Spring	89
Appendix E: Additional Notes	93
E.1 The Jacobi-Anger Identity	93
E.2 Comparison of Phase Modulation (PM) and Amplitude Modulation AM	93
E.3 Comparison of Phase Modulation (PM) and Frequency Modulation (FM)	94
E.4 Calibration	95
E.5 Only the Signal Field Matters	95
E.6 Optical Phase Conventions	95
E.7 Gaussian Beams	96
E.8 Laser Modes	96
E.9 Shot Noise	97
Vita	98

List of Tables

4.1	Output mode cleaner properties (designed and measured)	36
5.1	Interferometer parameters used in the shot noise model.	51

List of Figures

1.1	Effect of a gravitational wave on a ring of test particles	3
1.2	EXPLORER bar detector	5
1.3	Aerial photo of LIGO Livingston Observatory	8
2.1	Michelson interferometer	12
2.2	Phasor diagram of DC readout	13
2.3	Three mirror cavity	16
2.4	The coupled-cavity pole	16
2.5	Pound-Drever-Hall setup	18
2.6	Pound-Drever-Hall error signal	19
2.7	Illustration of cyclo-stationary shot noise	22
3.1	Comparison of DC readout with balanced homodyne detection	24
3.2	DARM fringe	25
3.3	Frequency-domain fields in DC and RF readouts	27
3.4	Enhanced LIGO interferometer layout	29
3.5	Residual DARM motion	32
4.1	Beam spot at the interferometer output port	35
4.2	OMC diagram and photograph of installation	36
4.3	Output Mode Cleaner photograph	37
4.4	Cartoon view of dither locking	39
4.5	Modal decomposition of a displaced Gaussian	41

4.6	Drumhead dither system	42
4.7	Measurement of OMC backscatter	44
4.8	Length Sensing and Control (LSC) control screen	46
5.1	Shot noise sensitivity limit (measured and expected)	52
5.2	Radio- and audio-frequency sidebands	53
5.3	Components of laser intensity noise contribution to DC readout	55
5.4	Laser intensity noise coupling (measured and modeled)	58
5.5	Laser frequency noise coupling (measured and modeled)	59
5.6	Oscillator amplitude noise coupling (measured and modeled)	61
5.7	Oscillator phase noise coupling (measured)	62
5.8	Example of linear and bilinear beam jitter coupling	63
C.1	Fabry-Perot Cavity	81
C.2	Pole-zero map of Fabry-Perot cavity reflectivity	83
C.3	Cavity buildup versus detuning	86
C.4	Cavity amplitude reflectivity plotted in the complex plane	87
D.1	Optical spring transfer function (numerical and analytic)	92
E.1	Scattering matrix	95

Abstract

Gravitational waves are ripples of space-time predicted by Einstein's theory of General Relativity. The Laser Interferometer Gravitational-wave Observatory (LIGO), part of a global network of gravitational wave detectors, seeks to detect these waves and study their sources.

The LIGO detectors were upgraded in 2008 with the dual goals of increasing the sensitivity (and likelihood of detection) and proving techniques for Advanced LIGO, a major upgrade currently underway. As part of this upgrade, the signal extraction technique was changed from a heterodyne scheme to a form of homodyne detection called DC readout. The DC readout system includes a new optical filter cavity, the output mode cleaner, which removes unwanted optical fields at the interferometer output port.

This work describes the implementation and characterization of the new DC readout system and output mode cleaner, including the achieved sensitivity, noise couplings, and servo control systems.

Chapter 1

Introduction

1.1 Gravitational Waves

Almost all of humanity's knowledge of the universe is derived from observations of electromagnetic waves. The effort to detect gravitational waves (GWs) seeks to expand this knowledge by observing an entirely different field, and to further verify the correctness of the theory of general relativity.

Any theory of gravity that avoids instantaneous action at a distance must feature some kind of gravitational waves. Even Newtonian gravity can be modified to account for propagation delays from massive bodies that are the sources of attraction[1]. Gravity as we know it, however, is described by the general theory of relativity. In general relativity, spacetime is treated as a four-dimensional manifold with some intrinsic curvature. This curvature is generated by the presence of mass and energy. In the absence of forces, particles follow geodesic trajectories on this manifold. Quintessentially, "Space tells matter how to move; matter tells space how to curve" [2].

This relationship between matter and curvature is made formal through the Einstein field equation, which equates (up to units) the Einstein tensor (G), encoding curvature, with the Stress-Energy tensor (T), encoding the matter and energy contents:

$$G = \frac{8\pi G}{c^4} T \quad (1.1)$$

where G is (Newton's) universal gravitational constant and c is the speed of light.

To perform calculations, we typically need to work in some coordinate basis. Thus one will work with $G_{\mu\nu}$, where μ and $\nu \in 0, 1, 2, 3$ are coordinate indices. In this notation, the Einstein tensor is given by $G_{\mu\nu} = R_{\mu\nu} - \frac{1}{2}Rg_{\mu\nu}$, where $R_{\mu\nu}$ is the Ricci curvature tensor, R is the Ricci scalar, and $g_{\mu\nu}$ is the spacetime metric. The metric plays a central role here, as it both encodes the curvature and implicitly defines the coordinate system.

To reveal the mechanism of gravitational waves, we are interested in vacuum ($T = 0$) solutions of the Einstein field equations in the weak-field limit. In the weak-field limit, we can write the metric $g_{\mu\nu}$ as the sum of the flat-space Minkowski metric $\eta_{\mu\nu}$ and a small

perturbation $h_{\mu\nu}$:

$$g_{\mu\nu} = \eta_{\mu\nu} + h_{\mu\nu}$$

This is the regime of linearized gravity. Calculating out the Einstein field equation keeping only terms of first-order in h and choosing the transverse-traceless gauge, one finds[3] a wave equation for h :

$$\left(\nabla^2 - \frac{1}{c^2} \frac{\partial^2}{\partial t^2} \right) h_{\mu\nu} = 0$$

where $h_{\mu\nu}$ has, for a wave propagating along the z axis, the form:

$$[\mathbf{h}(z, t)] = \begin{pmatrix} 0 & 0 & 0 & 0 \\ 0 & h_+ & h_x & 0 \\ 0 & h_x & -h_+ & 0 \\ 0 & 0 & 0 & 0 \end{pmatrix} \cos(2\pi f(t - z/c))$$

Here we see several of the essential points of gravitational waves:

- there are two independent components (polarizations),
- they travel at the speed of light, and
- they are manifest as a transverse tidal force on inertial objects.

In the transverse traceless gauge, inertial objects reside at fixed coordinates. To see the effect of a gravitational wave, suppose inertial test masses reside at coordinates 0 and L_0 along the x axis, and suppose a gravitational wave is incident along the z axis. The proper length between two points is given by

$$L = \int \sqrt{-g_{\mu\nu} dx^\mu dx^\nu}$$

Integrating along the x axis, and assuming that the metric takes the form $g = \eta + h$, we find

$$L = \int \sqrt{g_{xx}} dx \tag{1.2}$$

$$= L_0 \sqrt{1 + h_+} \tag{1.3}$$

$$\approx L_0 \left(1 + \frac{1}{2} h_+ \right). \tag{1.4}$$

The gravitational wave lengthens the path by $\Delta L = \frac{1}{2}h_+$. Half a period later, the wave will shorten the path length by the same amount. Simultaneously, a similar path along the y axis will see a ΔL of the opposite sign. This oscillatory transverse stretching and compressing is depicted in figure 1.1. Because the change in optical path length has the form of a change in length per unit length, it is often described as a *strain*.

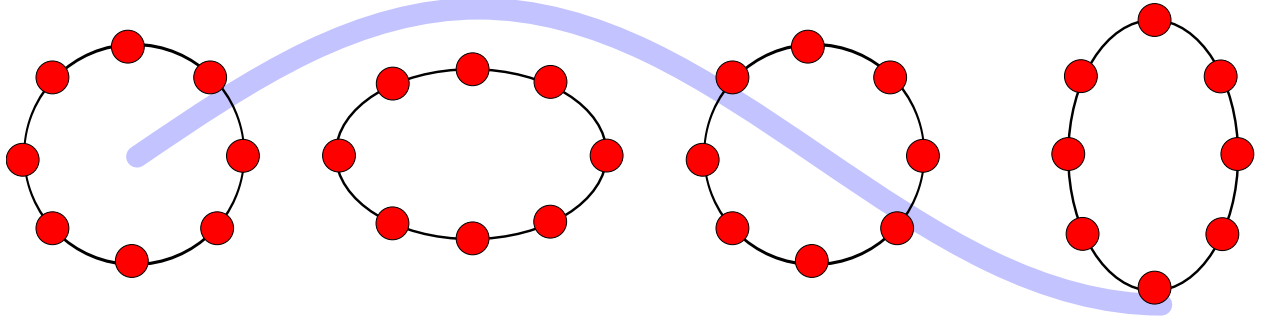


Figure 1.1: Effect of a gravitational wave (traveling into or out of the page) on a ring of non-interacting inertial test particles, with the gravitational wave waveform superimposed.

A photon traveling from one test mass to another will see this change in proper length, assuming that the gravitational wave phase (and thus the metric) changes negligibly in the time required by the photon to make the trip. This is the basis of laser interferometric gravitational wave detectors: if we can arrange mirrors as inertial test masses, then we can imprint the gravitational wave onto the phase of laser light.

1.2 Generation of Gravitational Waves

Conservation of energy and momentum forbid changes in the monopole and dipole moments of an isolated mass distribution. The leading multipole term leading to gravitational wave radiation is therefore the quadrupole moment, which is forbidden by no conservation law. For instance, two objects in orbit around one another exhibit a time-varying quadrupole moment.

A typical GW source of interest is a pair of massive objects revolving around their common center of mass in a binary orbit. Maggiore[4] gives the strain in the two polarizations h_+ and h_\times due to two objects in a circular, binary orbit as

$$h_+(t) = \frac{4G\mu\omega^2 R^2}{r c^4} \frac{1}{2} (1 + \cos(\theta)^2) \cos(2\omega t) \quad (1.5)$$

$$h_\times(t) = \frac{4G\mu\omega^2 R^2}{r c^4} \cos(\theta) \sin(2\omega t) \quad (1.6)$$

where r is the distance to source, μ is the reduced mass of the binary system, R is the radius of the binary orbit, θ is the angle between the normal of the orbital plane and the line of sight to the observer, and 2ω is the gravitational wave frequency. Some points to note include:

- The gravitational wave strain drops only as $1/r$ with distance from the source, in contrast to the inverse square law by which electromagnetic observations suffer.
- The gravitational wave frequency is twice the orbital frequency.

- The emission is surprisingly isotropic.
- Most of the GW emission is along the rotational axis of the binary system; these GWs are circularly polarized. Emission in the plane of the binary system is linearly polarized. This is as one would expect from basic symmetry considerations.

To get a sense of the scale of the phenomenon, we can plug in some numbers. A binary system in the Virgo cluster orbiting at 50 Hz where each object is a one-solar-mass star would produce an expected strain on earth of the order $h \sim 10^{-21}$ – an almost preposterously small effect, making GW detection a significant challenge.

1.3 The Hulse-Taylor Pulsar

The emission of gravitational waves by a binary star system has already been confirmed through indirect observation. In 1974, Hulse and Taylor discovered a radio pulsar that is a member of a binary star system[5, 6]. The electromagnetic emissions of the pulsar allowed the orbital parameters of the binary system to be precisely tracked over a long period of time. As the system spins, energy is radiated away from the orbital system in the form of gravitational waves. Measurement of the orbital period through pulsar tracking over 30 years shows that the orbit is decaying exactly as predicted by general relativity¹

1.4 Detectors

The first attempts to detect gravitational waves used resonant bar detectors[11, 12]. In such a detector, a large cylinder of a metal alloy with a very high mechanical Q-factor is suspended in a vacuum chamber and cooled to cryogenic temperatures. A passing gravitational wave couples mechanical energy into the bar, ringing up the fundamental mechanical mode of the bar. Sensitive displacement sensors (later bars used SQUIDs) read out this mechanical displacement. Resonant bars are inherently narrow-band devices, sensitive to gravitational waves within a narrow linewidth about their fundamental resonance.

Bar detectors do have the advantage that they are small enough that they can be moved or re-oriented. The ALLEGRO bar detector at LSU [9] was rotated to modulate its overlap function with the nearby LIGO Livingston observatory, and the data was analyzed for coincident events between LIGO and Allegro[13]. A typical cryogenic resonant bar detector setup is depicted in figure 1.2.

1.4.1 Laser Interferometers

Inaugurated by an initial study by Rai Weiss[14] and experiments by Robert Forward[15] in the 1970’s, laser interferometers are now the instrument of choice in the search for gravita-

¹Another binary system containing pulsars was discovered in 2004. In this system *both* objects are pulsars[7, 8].

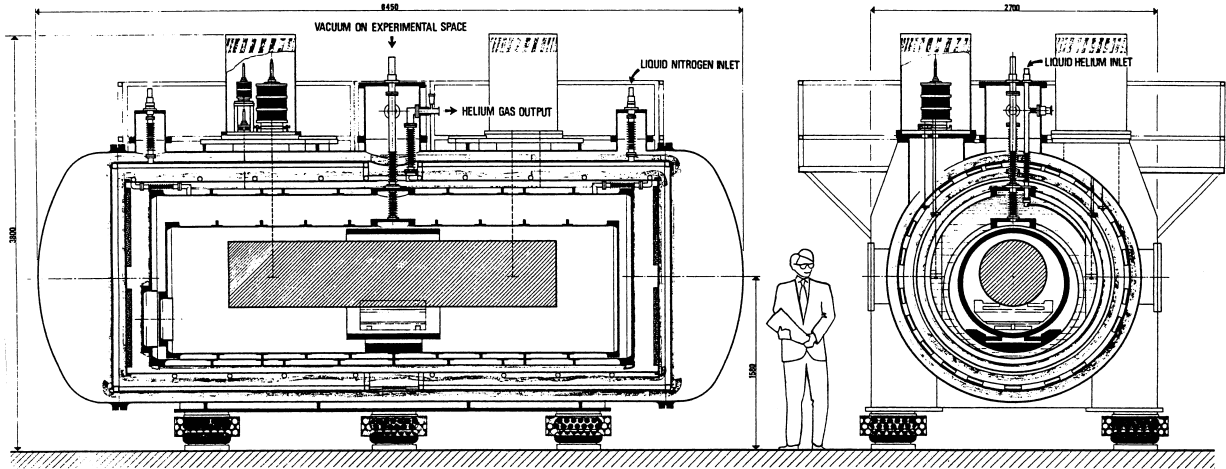


Figure 1.2: Depiction of the cryostat of the EXPLORER bar detector, which has operated at CERN since 1990. EXPLORER was oriented in parallel to the ALLEGRO detector at LSU[9] to enable searches for coincident detections. Illustration adapted from [10].

tional waves. A gravitational wave will modulate the optical path length of light traveling between inertial test masses. This path length modulation can be detected by a laser interferometer. In terrestrial interferometers, large ($\sim 10\text{kg}$) glass cylinders serve as both super-polished mirrors and inertial test masses. These optics are hung as pendula to allow inertial freedom of the pendular resonance frequency and enclosed in a large, high-vacuum enclosure.

Large laser-interferometer gravitational wave detector installations include LIGO[16] in the United States, VIRGO[17] in Italy, and GEO600[18] in Germany. The operation of laser interferometer gravitational wave detectors is the focus of this work and is detailed in the following chapters.

1.4.2 Other Detectors

There are a few other mechanisms by which gravitational waves may be detected, or by which their influence may be observed.

Pulsars serve as extremely reliable clocks, beaming a sequence of pulses towards earth whose arrival times can typically be predicted to better than a microsecond. The path of the electromagnetic waves traveling from the pulsar to earth acts in some ways like an arm of a laser interferometer: gravitational waves passing transversely to the Earth-Pulsar baseline will modulate the optical path length, producing perturbations in the arrival time of the pulsar pulses—perturbations which are correlated between observations of distinct pulsars. Pulsar timing arrays seek to analyze these correlated residuals to find evidence of gravitational waves; Hobbs [19] anticipates that pulsar timing analysis will yield detections of gravitational waves in the nanohertz regime (period 3-30 years) in the next 5-10 years.

Primordial gravitational waves will also leave their imprint on the polarization of the cosmic microwave background radiation. Many CMB polarization experiments are currently underway (e.g. [20]), searching for the faint “B-modes” in the microwave polarization.

1.4.3 Detector Products

The data produced by a gravitational wave detector consist of the calibrated strain time series $h(t)$ (current detectors are sensitive to only a single polarization) along with auxiliary data streams which convey the state of the detector and its environment. These auxiliary data streams are used for both detector debugging and for vetoing of candidate signals which are coincident with local environmental disturbances[21, 22].

1.5 Sources of Gravitational Waves

Anticipated sources of gravitational waves can be conveniently categorized as *continuous* or *transient*, and as *modeled* or *unmodeled*. There is some overlap in this division. Associated with each potential source of gravitational waves are *search efforts* which search the data produced by extant gravitational wave detectors for evidence of GWs from that source.

- **compact binary coalescence** — Pairs of compact objects (black holes or neutron stars) in binary orbits are expected to lose energy through gravitational waves, causing the orbit to decay until the objects finally begin to interact and merge into a single object. This inspiral process will generate a characteristic chirp signal, followed by the complex merger process and then ringdown.
- **continuous wave** — Rapidly spinning objects will generate essentially monochromatic signals, which are in turn doppler-shifted by the relative motion of the Earth and the source. The search for these signals is sometimes called the pulsar search, since the primary source in this category is expected to be rapidly spinning neutron stars (such as pulsars). The search, in turn, is divided into searches for known pulsars and unknown pulsars. Pulsars which are known electromagnetically can be targetted directly, whereas unknown pulsars require a brute-force search of the parameter space. Currently this is attacked in part through the distributed computing project Einstein@Home. Interestingly, the pulsar search works equally well for analyzing radio telescope data; several previously unknown radio pulsars have been discovered by feeding Aricebo data into the Einstein@home project[23].
- **bursts** — Transient cataclysmic events such as supernovae will generate bursts of gravitational waves whose waveforms are not known in advance.
- **stochastic background** — In the same manner as the cosmic microwave background radiation, a cosmological background of gravitational waves is expected to exist. This is perhaps the most exotic anticipated source of gravitational waves, since its detection

will inform us of the state of the universe at an age far earlier than has yet been probed. Sadly, the cosmological background is almost certainly too weak to detect in the foreseeable future.

The cacophony of unresolved astrophysical sources also combines to produce a gravitational wave stochastic background.

The stochastic background search is fully coherent. In its simplest form, the search simply computes the correlation between pairs of gravitational wave detectors. This can be done in either an all-sky search or in a sky-position-dependent search. Typically, some power-law gravitational wave spectrum is assumed. The signal processing strategy for the detection of a stochastic background is described by Allen and Romano in [24].

Improvements in search sensitivity can be achieved by incorporating knowledge of the expected signal waveform or spectrum; integrating over a long period of time (for continuous sources); and by looking for coincidence or coherence between multiple detectors.

The global network of gravitational wave detectors is operated as a sensor array, an interferometer composed of many interferometers.

1.6 LIGO

Ground was broken on the first of the two LIGO observatories in 1994. After years of construction and then detector commissioning, the three detectors at the two observatories (at Hanford, WA; and Livingston, LA, pictured in figure 1.3) reached their design sensitivity[25] in 2004[26]. Having reached this milestone, the attention turned to collecting data for astrophysical observation rather than instrument development. By October 2007, the LIGO project accomplished the goals of what is now known as “initial LIGO,” having collected 1 year of observational data with all three detectors online simultaneously, over the course of the 5th science run (known as S5).

It had always been intended that this initial generation of LIGO would be followed by a programme of improvements[27]. The next generation of LIGO detectors is “Advanced LIGO,” which will feature significantly more effective (and more complex) seismic isolation, an increase of $20\times$ in laser power, in addition to other improvements.

Rather than spend the entire time before the onset of Advanced LIGO taking observational data in the Initial LIGO configuration, it was decided to implement an intermediate series of upgrades in a project that came to be called “Enhanced LIGO”[28, 29, 30]. The goals of enhanced LIGO were to both increase the chances of an early discovery (by increasing the detector sensitivity), and to gain early experience with Advanced LIGO technologies.

The observational data collected so far has been analyzed (and continues to be analyzed) for evidence of gravitational waves. Although no gravitational waves have yet been detected, these searches have set the tightest upper limits to date on GW emission. Results of searches for compact binary inspirals[31, 32], unmodeled bursts[33, 34], known pulsars[35], periodic



Figure 1.3: Aerial photo of the LIGO Livingston Observatory, containing the L1 detector. The main building in the center of the photo contains the beamsplitter; the two 4 km arms reach out to the right of the photo. Photo by Greg Grabeel and the author.

sources[36], GWs associated with a gamma-ray burst[37], a particular neutron star[38], and the stochastic background[39] have recently been published. The gamma-ray burst paper[37] illustrates the value of the LIGO observational results despite not having actually detected any GWs. The electromagnetically observed sky position of gamma ray burst 070201 was coincident with the spiral arms of the Andromeda galaxy (M31); the *non-detection* of GWs associated with the event led to the conclusion that it did not occur in M31, but much further away.

1.6.1 Summary of Changes Made for Enhanced LIGO

Detector upgrades during Enhanced LIGO included:

- An increase in laser power. The initial LIGO laser, an Nd:YAG NPRO capable of producing < 10 Watts of laser power at a wavelength of 1064 nm, was replaced with the Advanced LIGO laser front-end, built by Laser-Zentrum Hannover[40], with an output power of 35 W.
- The input optics were redesigned to handle the higher input power [41, 42].
- A new thermal compensation system was implemented to compensate for the greater amount of thermal lensing that would be induced by the higher operating power[26, 43].

- An output mode cleaner was installed, supported by a prototype of the advanced LIGO in-vacuum seismic isolation system [44]
- The Angular Sensing and Control system was redesigned to cope with angular instabilities introduced at high power [45, 46]
- Readout of the gravitational wave channel was changed from RF readout to DC readout.

The state of the LIGO detectors before these modifications is described in [16] as well as numerous PhD dissertations, notably Rana Adhikari's [47] and Stefan Ballmer's [26]. Robert Ward's dissertation details the implementation and evaluation of DC readout at the LIGO 40 meter prototype interferometer in Pasadena [48]. During the same time as Enhanced LIGO, DC readout was simultaneously and independently implemented at GEO[49, 50].

1.7 The Future

It is hoped that Advanced LIGO and Advanced VIRGO, currently under construction, will bring the first direct detection of gravitational waves and begin the era of regular detection and gravitational wave astronomy. Beyond the 'Advanced' detectors, several next-generation interferometers are also in the works.

Technological development of terrestrial laser interferometers is a vibrant field. The Advanced detectors are anticipated to be limited almost everywhere by quantum mechanical noises, making gravitational wave detectors an active field for work in quantum optics. The next generation of terrestrial gravitational wave detectors will be limited by near-field gravity—"Newtonian noise" from density waves in the surrounding environment. The path forward will be to move underground (where this effect is smaller); measure, predict, and subtract the Newtonian noise contribution using a seismic sensor array; or to move into space. The Einstein telescope [51] is a proposed system of three interferometers with arms forming an equilateral triangle, to be installed in tunnels deep under Europe.

Going into space makes feasible the use of extraordinarily long arms and yields complete freedom from terrestrial noise, allowing access to very low frequency gravitational waves. The Laser Interferometer Space Antenna (LISA) design is composed of three spacecraft forming an equilateral triangle, the whole constellation in solar orbit[52]. These spacecraft will house truly inertial test-masses, floating within an internal vacuum enclosure while external microthrusters keep the spacecraft centered around the test mass, a configuration known as a drag-free satellite [53]. The gravitational wave channel is derived using time-delay interferometry. The proposed LISA design is sensitive to gravitational waves in the range 10^{-4} to 10^{-1} Hz (period of 3 hours down to 10 seconds).

1.8 This Dissertation

LIGO, is, of course, a team effort, conducted by the LIGO Laboratory and by the LIGO Scientific Collaboration, of which I am a member. The success of LIGO is due to the hard work of hundreds of people over the course of several decades. I came to LIGO Livingston Observatory in January 2008 where I worked with the commissioning team to commission the enhancements to the L1 detector (i.e. make it work) with a specific focus on DC readout and the output mode cleaner (OMC), which are the focus of this work. This dissertation describes the implementation of DC readout and an output mode cleaner during Enhanced LIGO. My personal scientific contributions to the project are concentrated in chapter 5.

In Chapter 2, I explain the principles and practice behind the sensitivity of the LIGO detectors. I show how the machine converts gravitational wave-induced phase modulation into a modulated optical field while offering a large amount of immunity to other effects.

In Chapter 3, I describe DC readout, the newly implemented scheme for recovering the gravitational wave signal from the optical fields exiting the interferometer.

Chapter 4 introduces the output mode cleaner, its design and control, and the general idea of mode cleaners.

Finally, in Chapter 5, I present results demonstrating the performance of this system, including measurements and models of the transfer functions of laser and oscillator noises, and verification that the noise floor of the enhanced detector is well understood.

Chapter 2

The LIGO Detector

2.1 An Interferometric Gravitational Wave Detector

The purpose of the LIGO detectors is to measure the faint oscillations of spacetime imparted by far-away astrophysical processes. Through clever design and careful engineering, these machines are capable of resolving these tiny perturbations from the much louder sea of noise on the surface of the Earth[54].

As described in the preceding chapter, a passing gravitational wave modulates the optical path length of light passing between inertial test masses. To exploit this effect and build a detector around it, we need to arrange to have inertial test masses. We need to be able to tell the difference between phase perturbations due to the gravitational wave and phase perturbations inflicted by our light source. We need to eliminate sources of phase variations that would be louder than the effect we wish to measure.

The essential points are:

- We approximate inertial test masses by hanging the optics as pendula. These act as inertial masses above the pendulum resonance.
- We build a Michelson interferometer for its common-mode noise rejection. A suitably-polarized gravitational wave will modulate the arm lengths differentially, while laser frequency noise appears as a common mode modulation. Suppress the frequency noise by feeding back to the laser.
- To enhance the effect from a passing gravitational wave, we make the arms as long as possible. To further enhance the response, we have the light travel this path many times by using resonant cavities.
- To increase the optical response to a gravitational wave, we increase the light power in the interferometer by using power recycling.

The following sections describe these principles in further detail.

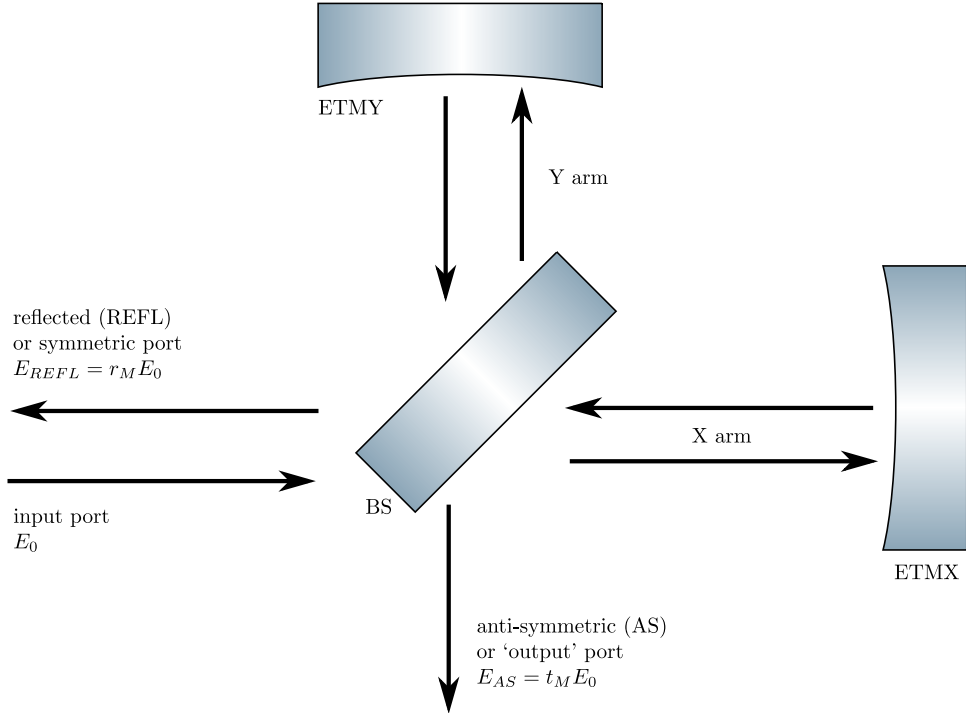


Figure 2.1: Michelson interferometer. This figure introduces some of the common nomenclature for the ports and optics of the Michelson interferometer. ETM stands for ‘end test mass.’

2.2 The Michelson Interferometer

Contemplating the effect of a gravitational wave on a ring of test particles (figure 1.1), it is easy to imagine constructing a Michelson interferometer (figure 2.1) with its beamsplitter in the center of the circle and with two of the test particles forming the end mirrors of the Michelson. More importantly, the Michelson allows us to separate the differential motion of the two arms from the common motion, which is indistinguishable from laser frequency changes.

If we assume a perfect (lossless, 50/50) beamsplitter, the transmission and reflection coefficients for the Michelson are:

$$t_M = \frac{1}{2} (r_x \exp\{i2\phi_x\} - r_y \exp\{i2\phi_y\}) \quad (2.1)$$

$$r_M = \frac{1}{2} (r_x \exp\{i2\phi_x\} + r_y \exp\{i2\phi_y\}) \quad (2.2)$$

where $r_{\{x,y\}}$ are the amplitude reflectivities of the x- and y-arm mirrors, and $\phi_{\{x,y\}}$ are the phases accumulated as the light travels from the beamsplitter to end mirrors. It is useful

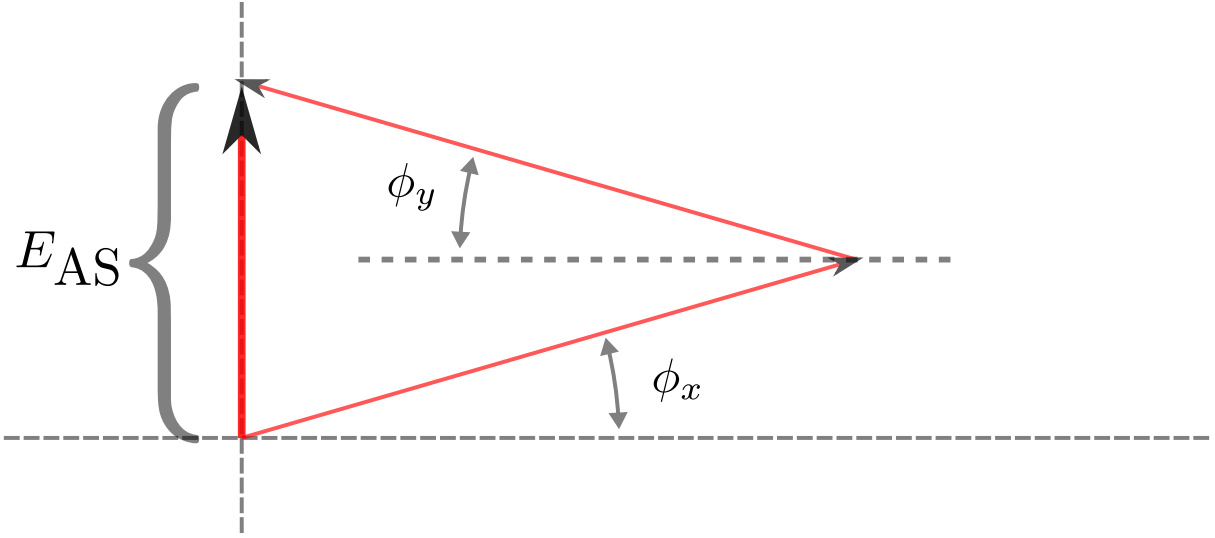


Figure 2.2: Phasor diagram of the fields at the output port due to the two arms of the Michelson. Differential motion of the mirrors at the ends of the arms causes equal but opposite rotation of the two phasors, which modulates the amplitude of the resultant electric field at the output port (E_{AS}).

to change our variables to express these quantities in terms of the differential and common reflectivities and phases. Making the substitutions

$$\phi_- = \phi_x - \phi_y \quad (2.3)$$

$$\phi_+ = (\phi_x + \phi_y)/2 \quad (2.4)$$

and

$$\Delta r = r_x - r_y \quad (2.5)$$

$$r = (r_x + r_y)/2 \quad (2.6)$$

yields

$$t_M = e^{i2\phi_+} (ir \sin \phi_- + (\Delta r/2) \cos \phi_-) \quad (2.7)$$

$$r_M = e^{i2\phi_+} (ir \cos \phi_- + (\Delta r/2) \sin \phi_-) \quad (2.8)$$

The intent is for the arm reflectivities to be identical (so $\Delta r \rightarrow 0$), and to operate near the *dark fringe* ($\phi_- \rightarrow 0$) so that the input field does not couple directly to the output port (i.e. $t_M \rightarrow 0$). Given this configuration, there are two salient points concerning gravitational wave detection:

- Variations of the differential phase ϕ_- *linearly couple* to the *field amplitude* at the output port. This can be seen via equation 2.7 or the phasor diagram in figure 2.2.

- Variations of the common phase ϕ_+ do not couple to the field at the output port, so long as we operate near $\phi_- = 0$ and the contrast defect (Δr) is small.

The field at the output port is thus sensitive to suitably polarized gravitational waves but insensitive to laser frequency noise¹.

Ultimately, we can not measure optical field amplitudes directly, because the field itself oscillates at $c/(1064 \text{ nm}) \approx 300 \text{ THz}$, much too quickly to measure directly. Instead we measure the power, i.e. the envelope of the optical field. We compute the power at the anti-symmetric and reflected ports by taking the squared magnitude of the field amplitudes. Using $P_{AS} = P_{BS} |t_M|^2$ and $P_{REFL} = P_{BS} |r_M|^2$:

$$P_{AS} = P_{BS} (r^2 \sin^2 \phi_- + (\Delta r/2)^2 \cos^2 \phi_-) \quad (2.9)$$

$$P_{REFL} = P_{BS} (r^2 \cos^2 \phi_- + (\Delta r/2)^2 \sin^2 \phi_-) \quad (2.10)$$

The power transmitted through the Michelson at the dark fringe is the *contrast defect*,

$$c_d = \frac{P_{AS}}{P_{BS}} = \frac{1}{4} (\Delta r)^2. \quad (2.11)$$

The linear relationship between ϕ_- and the electric field at the output port leads to a quadratic relationship between ϕ_- and the output port power. We will turn to the task of recovering a linear signal in section 2.7, but first we will consider methods to magnify the effect of a gravitational wave on ϕ_- .

2.3 Resonant Cavities

One approach to increasing the phase imparted by the GW to the light in the arms of the interferometer would be to arrange for the light to make multiple traversals of the arm length. This could be in the form of a delay line (where the optical path makes several zig-zags down the arm length in a definite number of bounces), or a resonant cavity (made by facing two partially-transmissive mirrors at each other, resulting in an effective number of bounces). Resonant cavities were chosen for the LIGO arms.

The basic setup of a Fabry-Perot cavity is shown in Figure C.1. Light entering the cavity interfered with light already circulating in the cavity. If, after making a round-trip through the interior of the cavity, the circulating light returns to its original phase (and spatial distribution), constructive interference will occur and the light will resonate in the cavity. If the mirrors have high reflectivity, then the light inside the cavity will survive for many round-trips inside the cavity. Any deviation from the required 2π radians of round-trip phase will be magnified on each bounce.

The theory of the Fabry-Perot cavity is derived in appendix C. For the purpose of this chapter, we need only the fact that changing the intra-cavity phase results in a much greater

¹An orthogonally polarized gravitational wave, whose strain ellipse is rotated 45° , will modulate ϕ_+ but this detector sacrifices sensitivity to that polarization in order to gain common-mode noise immunity.

change in the phase of the light reflected from the cavity; the ratio of these phase changes is the *phase gain*, given by $g_\phi = r'_c/r_c$, where r_c is the cavity reflectivity on resonance, and r'_c is its derivative with respect to changes in intra-cavity phase. The numerical values for r_c and r'_c in terms of the individual mirror reflectivities (for a lossless cavity) are (as derived in appendix C or given in [55]):

$$r_c = \frac{r_1 - r_2}{1 - r_1 r_2} \quad r'_c = \frac{(1 - r_1^2) r_2}{(1 - r_1 r_2)^2} \quad (2.12)$$

We typically work in the *long wavelength approximation*, in which we assume that the gravitational wave strain (or cavity length) changes slowly compared to the time required by light to travel from one mirror of the cavity to the other. Because light and gravitational waves travel at the same speed, this requires that the GW wavelength be much longer than the interferometer arm length.

2.4 Michelson with Fabry-Perot Arms

By replacing the end mirrors of our Michelson interferometer with Fabry-Perot cavities, the sensitivity to phase differences increases by a factor of the phase gain.

We now have

$$t_M = e^{i2g_\phi\phi_+} \left(r_c i \sin g_\phi \phi_- + \frac{\Delta r}{2} \cos g_\phi \phi_- \right) \quad (2.13)$$

where Δr now gives the difference between the reflectivities of the two arm *cavities*.

For Enhanced LIGO, the phase gain is approximately 140.

2.5 Power Recycling

The Michelson interferometer tuned to a dark fringe for the laser carrier sends most of the laser power back towards the laser. Instead of discarding this power, it can be sent back into the Fabry-Perot Michelson interferometer. This is done by adding an additional mirror, the *power recycling mirror*, that forms a resonant cavity with the rest of the interferometer. Choosing the reflectivity of the power recycling mirror to match the effective reflectivity of the rest of the interferometer makes this cavity critically coupled; ideally all of the laser carrier is coupled into the interferometer and very little is reflected. Most of the light stays in the interferometer until it is lost to scattering or absorption.

2.6 The Coupled Cavity Pole

The combination of the arm cavities and the power recycling cavity acts in some ways like a single cavity with a much longer storage time than either the arms or the PRC individually.

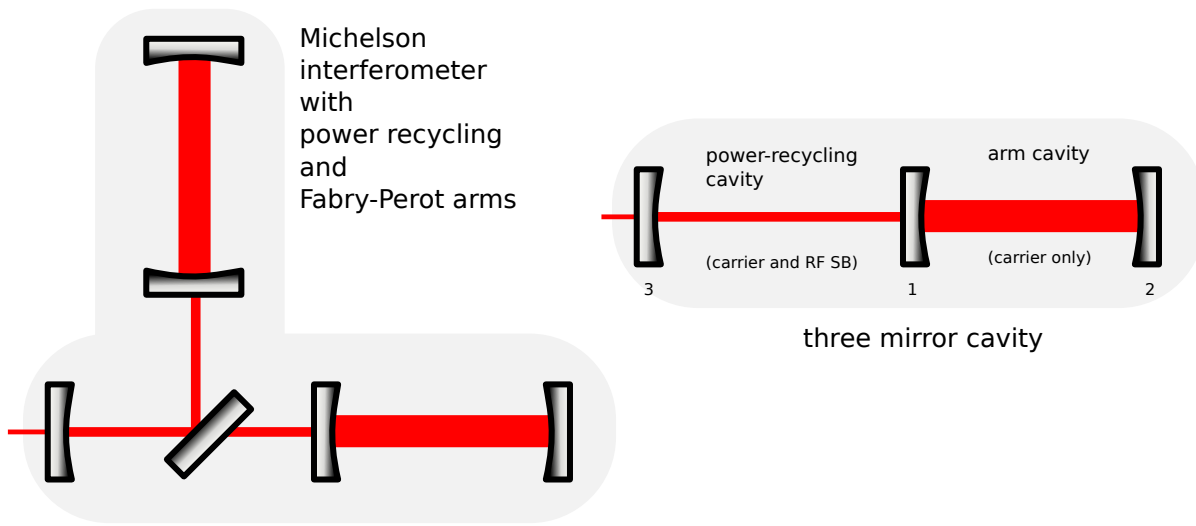


Figure 2.3: It is sometimes convenient to condense the two arms of the Power-Recycled Fabry-Perot Michelson interferometer into a single ‘virtual arm’ for the purpose of analysis.

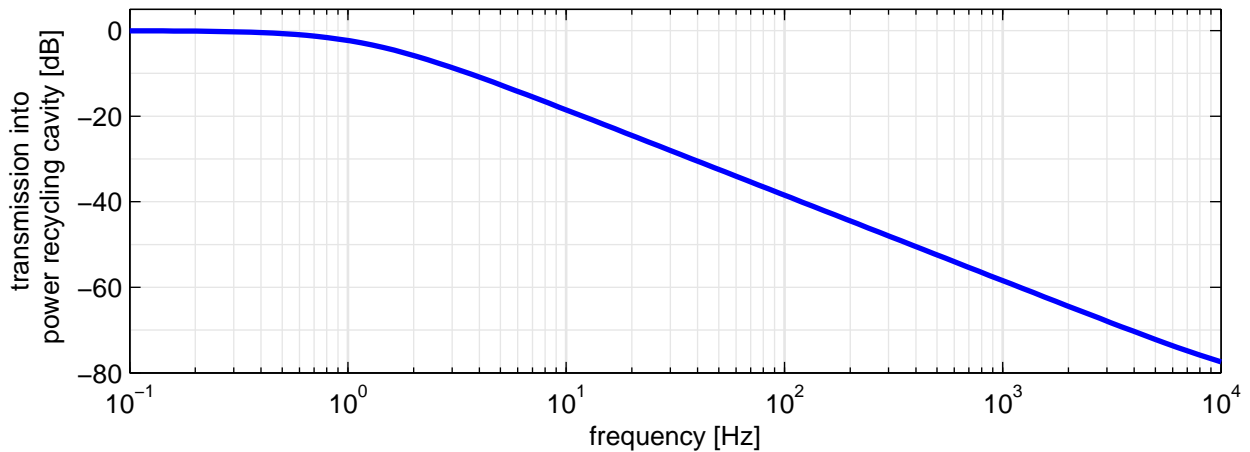


Figure 2.4: Transfer function from laser intensity fluctuations incident on the interferometer to laser intensity fluctuations inside the power recycling cavity. Fluctuations around the laser carrier above the coupled-cavity pole are attenuated.

This produces a filtering effect that will prove essential when we discuss DC readout later on.

Because the two arm cavities are made to be as nearly identical as possible, and because the Michelson is operated very close to the dark fringe, we can condense the two arm cavities into a single cavity for the purpose of analysis (depicted in figure 2.3). In considering the effect of amplitude or frequency perturbations of the input field, the power-recycled Fabry-Perot Michelson can be considered as a three mirror cavity.

It is useful to regard the cavity as acting as a linear operator on the input fields. To find the transfer function of the coupled cavity, we can simply substitute the cavity reflectivity function $r_c(\phi)$ given in equation C.6 into itself, with suitable substitutions. When this is done, it is found that the transfer function from fields at the interferometer input to the field just inside the PRC can be well described by a single pole at low frequency, the coupled cavity pole. There is no closed-form solution for the exact value of the coupled-cavity pole[56], but a very good approximation results if we first compute the reflectivity of the shorter cavity on resonance, and substitute this into the expression for the cavity pole of the larger cavity. Doing this, we find

$$f_{cc} \approx \frac{1}{2\pi} \nu_0 \log \left(\frac{r_3 - r_1}{1 - r_1 r_3} r_2 \right) \quad (2.14)$$

where f_{cc} is the frequency of the coupled cavity pole, ν_0 is the free spectral range of the arm cavity, and $r_{\{1,2,3\}}$ are the reflectivities of the ITMs, ETMs, and recycling mirror, respectively.

The coupled cavity pole in Initial/Enhanced LIGO is approximately 1 Hz. Astoundingly, this means that any amplitude or phase noise around the laser carrier (itself oscillating at 300 THz!) will be attenuated by $1/f$ above 1 Hz (see figure 2.4), making the carrier light circulating in the interferometer some of the ‘quietest’ light available anywhere. One of the motivations of DC Readout (chapter 5) is to exploit this effect fully.

2.7 Interferometer Sensing and Control

The power-recycled, Fabry-Perot Michelson optical configuration (collectively referred to as “the interferometer”) described above exhibits the desired sensitivity to gravitational waves and immunity to common mode noise. However, it only does so when the Fabry-Perot cavities are held on resonance, and the Michelson is held to the dark fringe. The need to sense the state of the interferometer and to use feedback control to keep it at the desired operating point is known as *interferometer sensing and control* (ISC). The initial LIGO sensing and control scheme is described in [57] and [58]. A pedagogical introduction is provided in [59].

The *control* aspect has not yet been mentioned. To allow actuation on the optics, the test masses are each equipped with five small magnets (four on the face and one on the side) which fit into solenoids mounted to the suspension structure. This electromagnetic drive allows forces to be exerted on the optics to control their position and orientation.

The initial LIGO detectors were designed to use, as much as possible, proven technologies. The proven technique for sensing the length/frequency mismatch of an optical cavity was

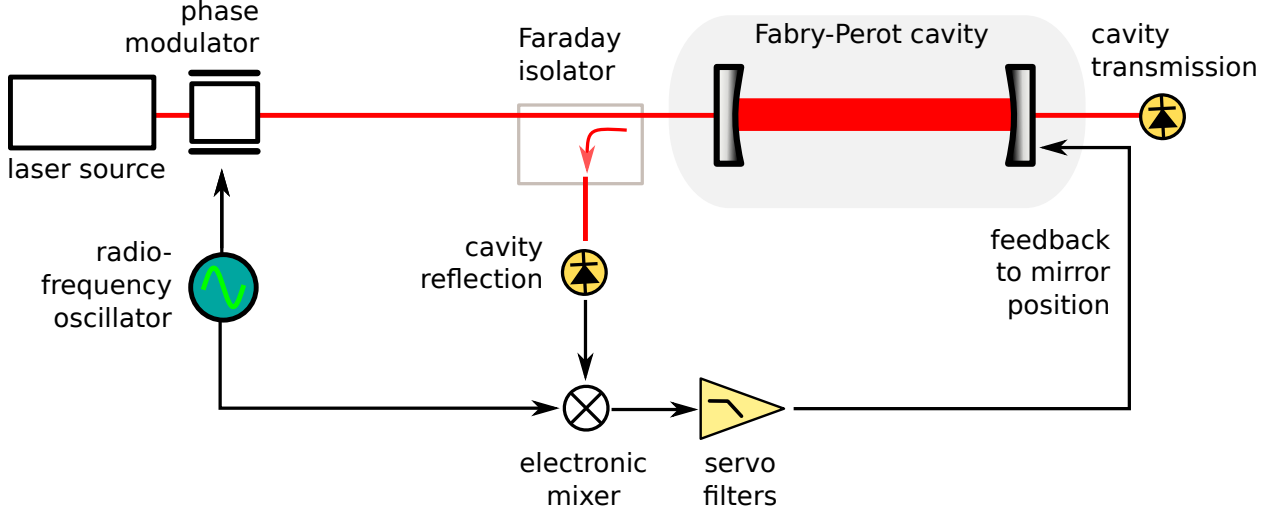


Figure 2.5: In the basic Pound-Drever-Hall setup, a phase modulator is used to produce RF sidebands well outside of the cavity bandwidth. The light reflected from the cavity is incident on a photodiode, the signal from which is demodulated to produce an error signal indicating the mismatch between cavity length and laser carrier frequency. Through feedback, the cavity can be ‘locked’ to the resonance. The technique can be generalized to sense and control much more complex interferometers.

the Pound-Drever-Hall (PDH) technique[60, 61], sometimes called reflection-locking, which can be used to lock the frequency of a laser to the length of a cavity, or vice versa.

2.7.1 The Pound-Drever-Hall Technique

In the basic PDH setup, the laser light incident on a resonant cavity is first phase-modulated at a frequency well outside of the bandwidth of the cavity, such that the phase-modulation sidebands are nearly anti-resonant in the cavity when the carrier is resonant. The light reflected from the cavity is directed onto a photodiode and an error signal is produced by demodulating this photodiode signal. The basic setup is depicted in figure 2.5.

The phase modulation may be expanded in terms of sidebands using the Jacobi-Anger expansion (see section E.1):

$$\exp \{i\Gamma \cos \Omega t\} = \sum_{n=-\infty}^{\infty} (i^n) J_n(\Gamma) \exp\{in\Omega t\} \quad (2.15)$$

$$= J_0(\Gamma) + iJ_1(\Gamma)e^{i\Omega t} - iJ_{-1}(\Gamma)e^{-i\Omega t} + \dots \quad (2.16)$$

From this expansion we see that phase modulation at a frequency Ω results in the creation of an infinite number of sidebands around the laser carrier, spaced at multiples of Ω , and whose amplitudes are given by the Bessel functions. The magnitude of the modulation (Γ , in radians) is known as the *modulation depth*. We typically use a small modulation depth, so

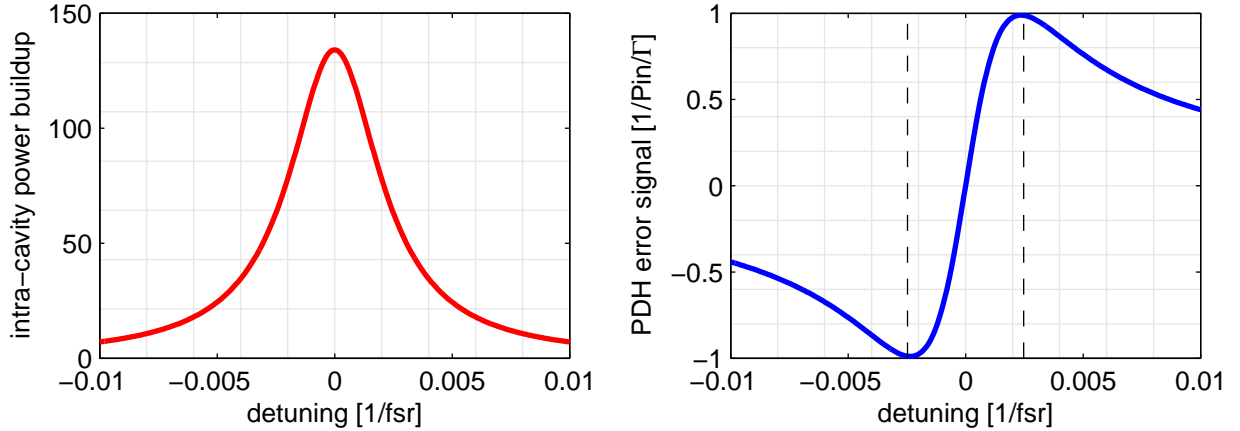


Figure 2.6: (a) Power buildup inside a resonant cavity relative to the incident power, as a function of cavity detuning (deviation from resonance). (b) The Pound-Drever-Hall error signal as a function of detuning (in watts relative to the incident power and the modulation depth). The dashed lines indicate the region in which PDH provides a usable error signal with which to lock the cavity. The cavity modeled here has parameters similar to the initial LIGO arm cavities.

that only the first-order sidebands are significant. These first-order sidebands are displaced from the carrier by the modulation frequency $\pm\Omega$ and have amplitude $J_1(\Gamma)$.

Upon reflection from a cavity the phases of the carrier and the two sidebands will be rotated. This phase rotation converts the phase modulation to amplitude modulation, which is observed by the photodiode. Typically, the laser frequency or the cavity length is adjusted to hold the carrier on resonance. Near the resonance, there is a very large change in reflected phase for a small change of detuning (mismatch between the cavity length and laser frequency); the RF sidebands, on the other hand, are typically far from resonance and experience very little phase change. As a result, a small perturbation from resonance will turn the cavity into an FM-to-AM converter. The resulting amplitude modulation can be sensed by a photodiode and demodulated to produce an error signal indicating how far the cavity is from resonance. The PDH error signal is depicted in figure 2.6.

2.7.2 Generalization of the PDH Technique

To sense and control the entire Power-Recycled, Fabry-Perot Michelson interferometer, the PDH scheme can be generalized to sense all degrees of freedom by providing one or more pairs of RF sidebands, and sensing and demodulating the light at various interferometer ports. In the remainder of this dissertation, however, we are concerned only with sensing the differential arm degree of freedom (DARM), which contains the gravitational wave signal.

2.8 Noises

No discussion of detector operation is complete without consideration of the noises which limit detection. The noise sources relevant to laser interferometer gravitational wave detectors are articulated in Rai Weiss's original design study[14] and Rana Adhikari's dissertation[47]. It is often useful to divide noises into *displacement noises* (which correspond to real displacement of the mirrors or intra-cavity phase modulation) and *sensing noises* (which arise in the sensing of the interferometer state). Displacement noises include:

- **seismic noise** – this refers to any motion of the mirrors due to local ground motion. Below ~ 40 Hz, the initial/enhanced LIGO noise floor is entirely limited by seismic noise (the so-called ‘seismic wall’).
- **thermal noise** – thermally excited motion in the test mass suspensions and the high-reflectivity coatings produces displacement noise[62, 63], which currently limits the sensitivity in the range 40 - 100 Hz.
- **quantum radiation pressure noise** – the Poisson statistics of the light circulating in the arm cavities generates a white-noise random force, producing a $1/f^2$ displacement spectrum. This noise source has not yet been observed, since its influence is masked by the other low-frequency noises.
- **technical radiation pressure noise** – variations in light intensity create varying radiation pressure forces.
- **residual gas noise** – any residual gas in the vacuum enclosure will displace the optics through Brownian motion, in addition to creating spurious phase modulation of the light.

Sensing noises include:

- **shot noise** – white noise due to Poisson statistics of light arriving at the detection photodiode. This is the limiting noise source at high frequency ($f \gtrsim 200$ Hz).
- **dark noise** – This is the name given to any electronics noise present when there is no light incident on the photodetectors. The electronics are generally designed such that dark noise is never limiting.

Some difficult-to-categorize noises:

- **upconversion** – for instance, the magnetic actuation system appears to suffer from Barkhausen noise. Large actuators lead to random noise due to the random, quantized flipping of magnetic domains. The result is that large actuators at low frequency lead to elevated noise at higher frequencies. Nonlinear effects such as this are lumped into the category of ‘upconversion’.

- **cross-couplings** – Imperfections in the diagonalization of the control system lead to noise in one degree of freedom being impressed on another. For example, actuation on the angular degrees of freedom can lead to perturbations of the differential arm length via imperfect angular actuation. As a result, there is the hazard of the angular control signal contaminating the gravitational wave channel with noise. One way to cope with this is to steeply cut off feedback of the offending control signal below the detection band.

2.9 Heterodyne Shot Noise

I conclude this chapter with a discussion of the shot-noise-limited sensitivity of a detector using heterodyne readout.

When a constant optical power P is incident upon a photodetector, we expect to observe Poisson shot noise in the resulting photocurrent. This shot noise has a white (flat) power spectrum, with amplitude spectral density $\sqrt{2Ph\nu}$, where $h\nu$ is the energy of an individual photon.

In the heterodyne readout system, the power on the photodiode is *not* constant; instead, the power varies sinusoidally at a frequency $2f_{mod}$ due to the beat between the upper and lower RF sidebands. At any given instant, a measurement of the rate of photon arrival will return a value from the Poisson distribution with mean $P/(h\nu)$, which has standard deviation $\sqrt{P/(h\nu)}$. A measurement of power therefore will give $P \pm \sqrt{h\nu P}$, where P is varying sinusoidally with time. This is an example of cyclostationary noise; a sample realization is depicted in figure 2.7. When considering a long time series ($t \gg 1/f_{mod}$), the signal will appear to have a noise floor determined by its average power. On closer examination, however, we see that the noise comes in bursts.

The bursty nature of this noise becomes a problem when we consider demodulation. Comparing the demodulation waveforms ($\cos 2\pi f_{mod}t$ and $\sin 2\pi f_{mod}t$) to the envelope of the noise, we see that one demodulation quadrature systematically samples the highest variance portions of the timeseries, while the other quadrature samples the lowest variance portions (see figure 2.7). The result[64] is that the shot noise ASD in a demodulated signal is

$$\sqrt{2h\nu\bar{P}\left(\frac{1}{2} - \frac{1}{4}\cos 2\theta\right)} \quad (2.17)$$

where \bar{P} is the average power on the photodiode and θ is the demodulation phase.

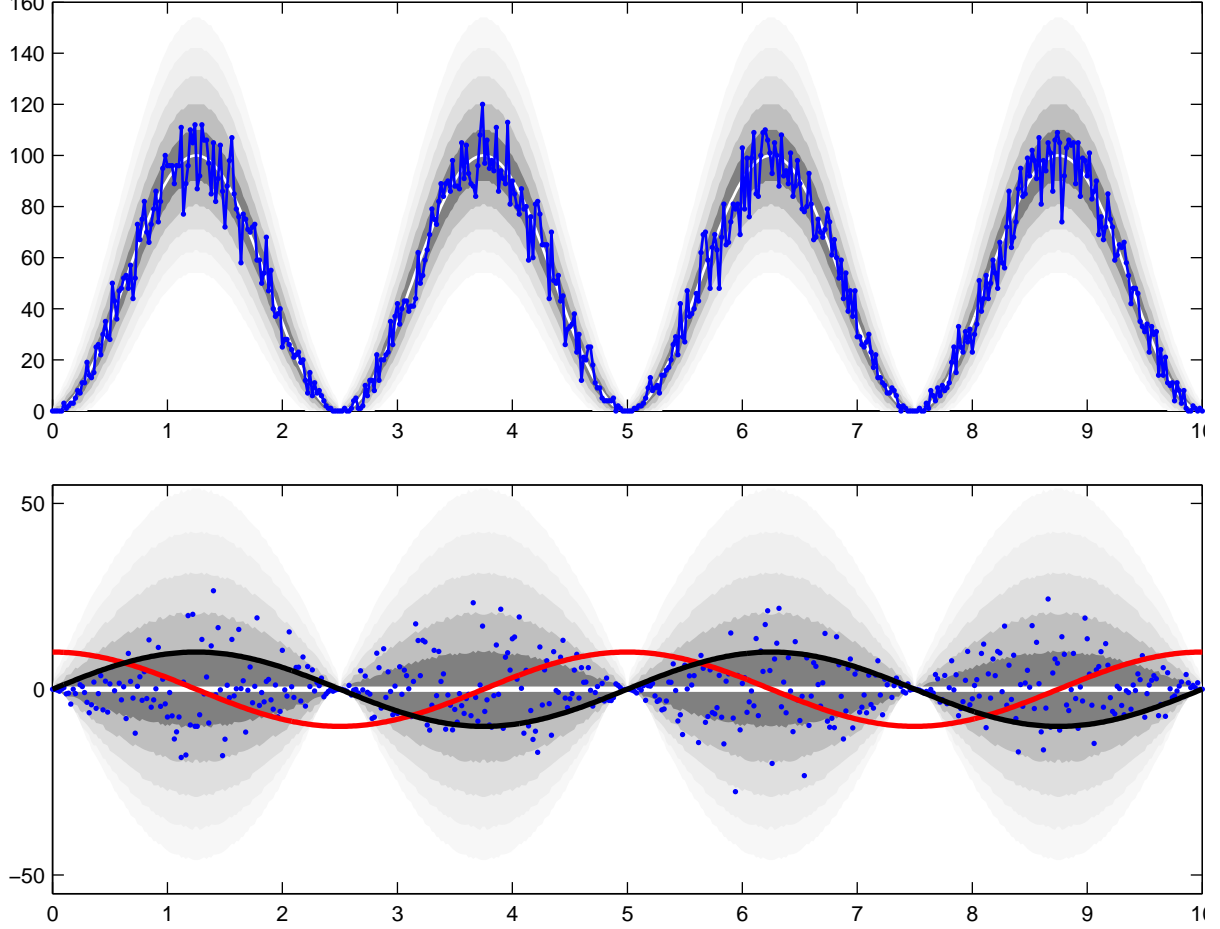


Figure 2.7: (a) Model of shot noise in the presence of sinusoidal power modulation, as occurs in optical heterodyne detection. The photodiode sees a power modulation at $2f_{mod}$ (white) due to the beat between the upper and lower modulation sidebands at $f_{carrier} \pm f_{mod}$. The gray levels represent the 1σ , 2σ , \dots , 5σ ranges for a Poisson distribution. The blue dots are a sample realization of this noise. (b) Subtracting the mean from (a) leaves only the noise; its bursty nature is obvious. Shown in black and red are the I and Q demodulation waveforms, respectively. It is clear that the in-phase demodulation (I) samples regions of the time series with higher variance than the quadrature phase (Q). This leads to a higher variance (shot noise level) in the I signal and a lower one in the Q signal relative to what one would expect from a naïve assumption based on the average power considered over a whole period of the waveform.

Chapter 3

DC Readout

The initial LIGO detectors used RF heterodyne detection, inspired by the Pound-Drever-Hall technique, to sense all interferometer length degrees of freedom and most angular degrees of freedom. During Enhanced LIGO, we changed the sensing of the gravitational wave channel (DARM) to a form of homodyne detection called DC readout. In this chapter I explain the motivation for and theory behind DC readout.

3.1 Principle of DC Readout

A homodyne readout system differs from a heterodyne system by using a local oscillator at the same (optical) frequency as the field being measured. A typical homodyne detection system combines a local oscillator (LO) field and a signal field via two different ports of a beamsplitter (depicted in figure 3.1(a)). The two PD signals are subtracted to recover the signal. This arrangement suffers from a number of technical difficulties[65], including the need to control the phase of the LO beam, and to maintain the alignment of the signal and LO beams.

DC readout¹ creates the homodyne local oscillator by putting a small offset into the Michelson or DARM degree of freedom, moving the interferometer slightly off of the dark fringe. The resulting carrier light at the interferometer output port acts as a local oscillator. This differs from the typical homodyne arrangement in that the two fields are automatically coincident² The principle disadvantages of DC readout over the 2-port homodyne arrangement are that DC readout requires introducing an intentional microscopic offset of the arms,

¹The name ‘DC readout’ probably came about simply in distinction to ‘RF readout’, with DC (from ‘direct current’) being a reference to its baseband nature. It is also kind of a pun since ‘direct conversion’ is another name for homodyne detection.

²It is no longer necessary to use two photodiodes, but doing so allows greater power handling capacity, and allows for the formation of a diagnostic ‘nullstream’. The nullstream is formed from the difference of the two PD signals and ideally contains only the uncorrelated component of the PD signals. The sum of the two PD signals provides the intended signal.

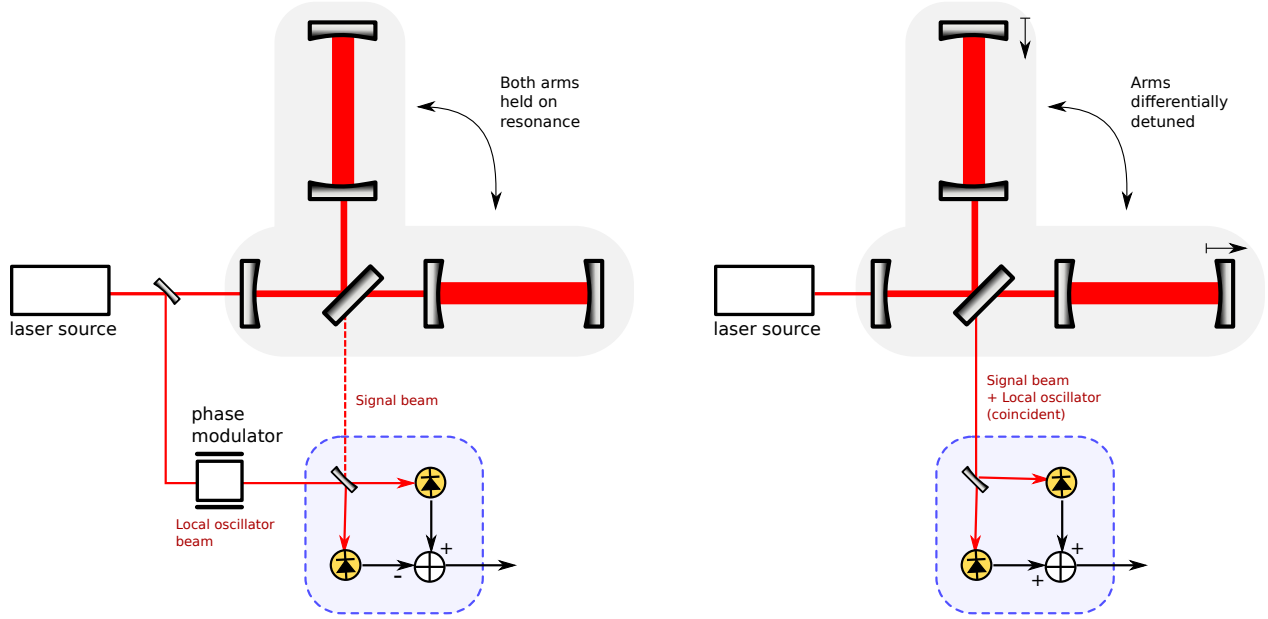


Figure 3.1: Left: a traditional ‘balanced photodiode’ homodyne detection arrangement. Right: DC readout with two photodiodes.

which can increase noise couplings, and that DC readout provides little control of the phase of the local oscillator.

One way to intuitively understand DC readout is that simply moving away from the quadratic point of the fringe (depicted in figure 3.2), a linear relationship from DARM variations to power variations is introduced. The frequency domain picture of the fields at the output port in both heterodyne and homodyne readouts is depicted in figure 3.3; we see that, in homodyne readout, the baseband signal at the photodiode is a result of a beat between the (no longer completely suppressed) carrier and the sidebands impressed by the gravitational wave.³

The true beauty of DC readout is that it exploits the filtering action of the compound interferometer to produce the local oscillator; any fluctuations in the amplitude or frequency of the input laser field are attenuated by the coupled cavity pole before reaching the output port.

³We might ask how phase modulation induced in the arms is converted to amplitude modulation at the AS port. The answer is that the Michelson rotates the carrier by 90 degrees due to the i in the Michelson transmission (equation 2.7).

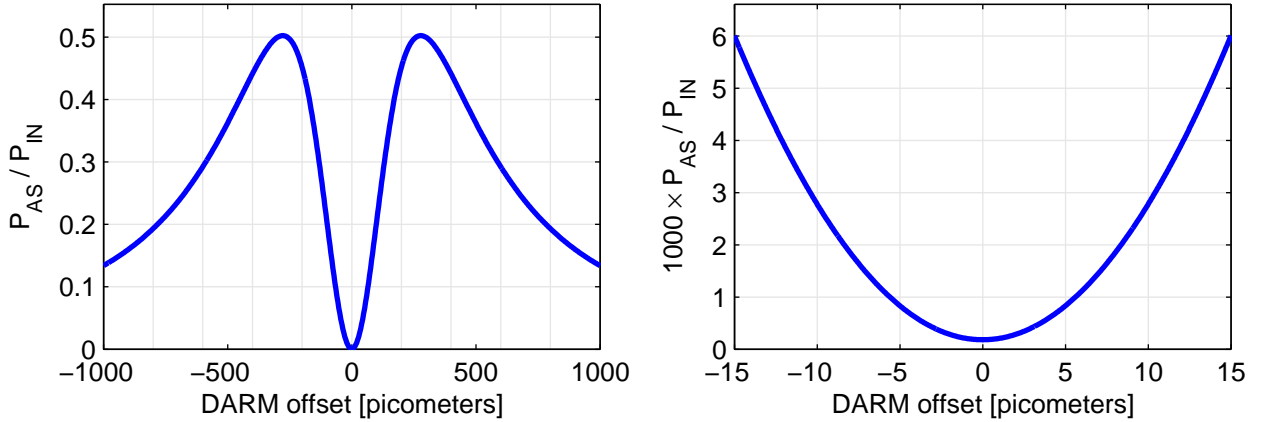


Figure 3.2: Power at the output port (P_{AS}) relative to the interferometer input power (P_{IN}), as a function of the DARM offset, in picometers ($1 \text{ pm} = 10^{-12} \text{ m}$). Left: The DARM fringe differs from the $P_{BS} \sin^2 kx$ of a simple Michelson since P_{BS} itself depends on the DARM offset. For comparison recall that the full fringe width (from one resonance to the next) is $\lambda \approx 10^{-6} \text{ m}$. Right: Detail. For small offsets, the fringe appears quadratic. DC readout operates with an intentional static DARM offset in order to create a linear relationship between DARM perturbations and P_{AS} . The small but nonzero minimum power at zero offset is the contrast defect.

3.2 Motivation for DC Readout

The RF readout technique was used successfully in initial LIGO to achieve the instruments' design sensitivity. A number of reasons, outlined below, motivated the switch to DC readout with an Output Mode Cleaner (OMC):

Improved Noise Couplings

The combination of the power recycling cavity and the arm cavities acts as a single resonant cavity with an effective linewidth of approximately 1 Hz around the laser carrier. Intensity and frequency noise around the laser carrier are reflected from the interferometer. The RF sidebands, which are not resonant in the arms, experience no such filtering in the band of interest. DC readout exploits this filtering by using the carrier light that has circulated in the interferometer as the local oscillator. The result is that coupling of noises on the input beam to the gravitational wave readout can be greatly reduced.

Spatial Overlap

Imperfect spatial overlap of the signal beam (resonant in the arm cavities) and the RF sideband beam (resonant in the power recycling cavity) reduced the optical gain, elevating the shot-noise-limited noise floor. For instance, a measurement in 2003 found only half

the expected optical gain[66]. This was alleviated in part through the use of a thermal compensation system (TCS), which projected light from a CO₂ laser onto optics to adjust their effective radii of curvature, compensating for thermal lensing. By the start of S5 in 2005, no elevation in the shot noise level was observed[26]. However, spurious fields still caused problems by producing a large signal in the uncontrolled quadrature of the heterodyne readout (AS_I); left uncontrolled, this signal would saturate the photodiode electronics. This was partially mitigated by an electronic servo which cancelled this signal in the photodiode head.

Both DC readout and an OMC mitigate problems with the spatial overlap of the LO and signal beams. In DC readout, the local oscillator and the signal beams are resonate in the same cavities, so spatial overlap comes naturally. With either DC or RF readout, an OMC, matched to the spatial mode of the signal beam, can be used to select the signal beam and the part of the LO with good spatial overlap.

Excess Power

To cope with the excess power due to higher-order modes at the interferometer output port, initial LIGO split the light at the detection port onto four detection photodiodes. Scaling the interferometer input power would require a commensurate increase in the number of photodiodes at the output port and their associated electronics. An output mode cleaner reduces the power that needs to be detected.

Homodyne SNR Advantage

Homodyne detection confers a fundamental improvement in signal-to-noise ratio compared to RF readout at shot-noise-limited frequencies by a factor $\sqrt{3/2}$ (for the same power circulating in the interferometer). The extra noise in heterodyne detection is a result of cyclostationary shot noise[64] due to the interference between the upper and lower RF sidebands.

Squeezed Vacuum Injection

Squeezed vacuum injection is an attractive means to decrease the photon quantum noise in future interferometers by manipulating the quantum state of the vacuum field that enters the interferometer through the output port. Squeezed vacuum injection is more feasible in conjunction with homodyne detection than with RF readout, since it requires squeezing in only the audio band rather than at both audio and RF frequencies[67, 68]. Shot noise reduction via squeezed vacuum injection has been demonstrated at GEO[69] and an effort is currently underway to implement it at LIGO Hanford[70].

3.3 Implementation of DC readout

The Enhanced LIGO optical plant is depicted in figure 3.4. The initial LIGO configuration was modified by adding an output mode cleaner (described in the next chapter) and DC

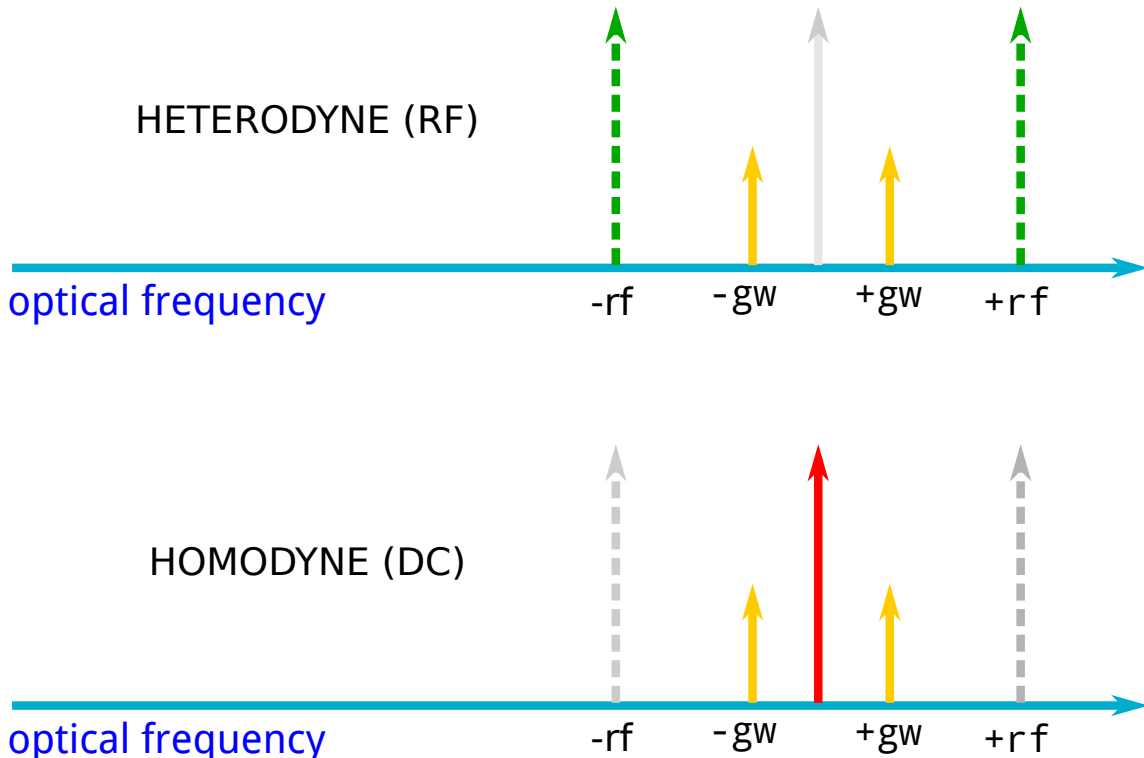


Figure 3.3: Depiction of the fields in DC and RF readouts. (a) In RF readout, the laser carrier is suppressed by operating the Michelson on a dark fringe for the carrier. Differential phase modulation in the arms becomes amplitude modulation of the (suppressed) carrier, depicted as the audio-frequency sidebands at $\pm f_{gw}$. The photodiode sees a beat between the GW signal and the RF sidebands. In homodyne readout, a carrier-frequency local oscillator is introduced—in DC readout this is done by introducing a microscopic asymmetry between the two arms. The RF sidebands are no longer needed and are removed by the output mode cleaner. The GW-induced sidebands appear as amplitude modulation on the carrier, which is sensed directly by the photodiodes.

photodiodes. A beamsplitter directs 97% to this new path and the remaining 3% to the old RF heterodyne output chain, which was still used for lock acquisition and automatic alignment. An additional computer system was added to acquire the signals from the DC photodiodes and to control the OMC.

3.3.1 Interferometer Lock Acquisition

Initial lock acquisition of the Enhanced LIGO interferometers is the same as in Initial LIGO[71]. Once the interferometer is locked using the heterodyne readout schemes, the DARM offset is introduced to allow carrier light to be transmitted to the output port. The Output Mode Cleaner is then locked to this carrier light. Once the OMC is locked to the carrier, control of DARM is transferred to the DC readout system. After this transition, a few other changes are made to engage the OMC alignment servoes and to put the readout electronics into low noise mode. At this point the interferometer has reached its operation configuration and astrophysical data-taking (“science mode”) begins.

3.4 Calculation of the Optical Gain

The ratio of signal produced (in Watts) to displacement of DARM (in meters) is the *optical gain*. In DC readout, we can find the optical gain for slow DARM variations by simply taking the derivative of the power at the anti-symmetric port with respect to changes in DARM.

From the prior chapter, take the expression for the power at the output of a Michelson:

$$P_{AS} = P_{BS} \left(r_c^2 \sin^2 \phi_- + (\Delta r/2)^2 \cos^2 \phi_- \right) \quad (3.1)$$

Taking the derivative with respect to ϕ_- , we find

$$\frac{dP_{AS}}{d\phi_-} = 2P_{BS} \left(r_c^2 - (\Delta r/2)^2 \right) \cos \phi_- \sin \phi_- \quad (3.2)$$

Immediately we see that any contrast defect ($\Delta r \neq 0$) will diminish the optical gain. Assuming $r \gg \Delta r$, we can neglect the contrast defect and get simply

$$P_{AS} = P_{BS} r_c^2 \sin^2 g_\phi kx \quad (3.3)$$

where $k = 2\pi/\lambda$ is the wavenumber, x is the DARM displacement, and g_ϕ is the phase gain.

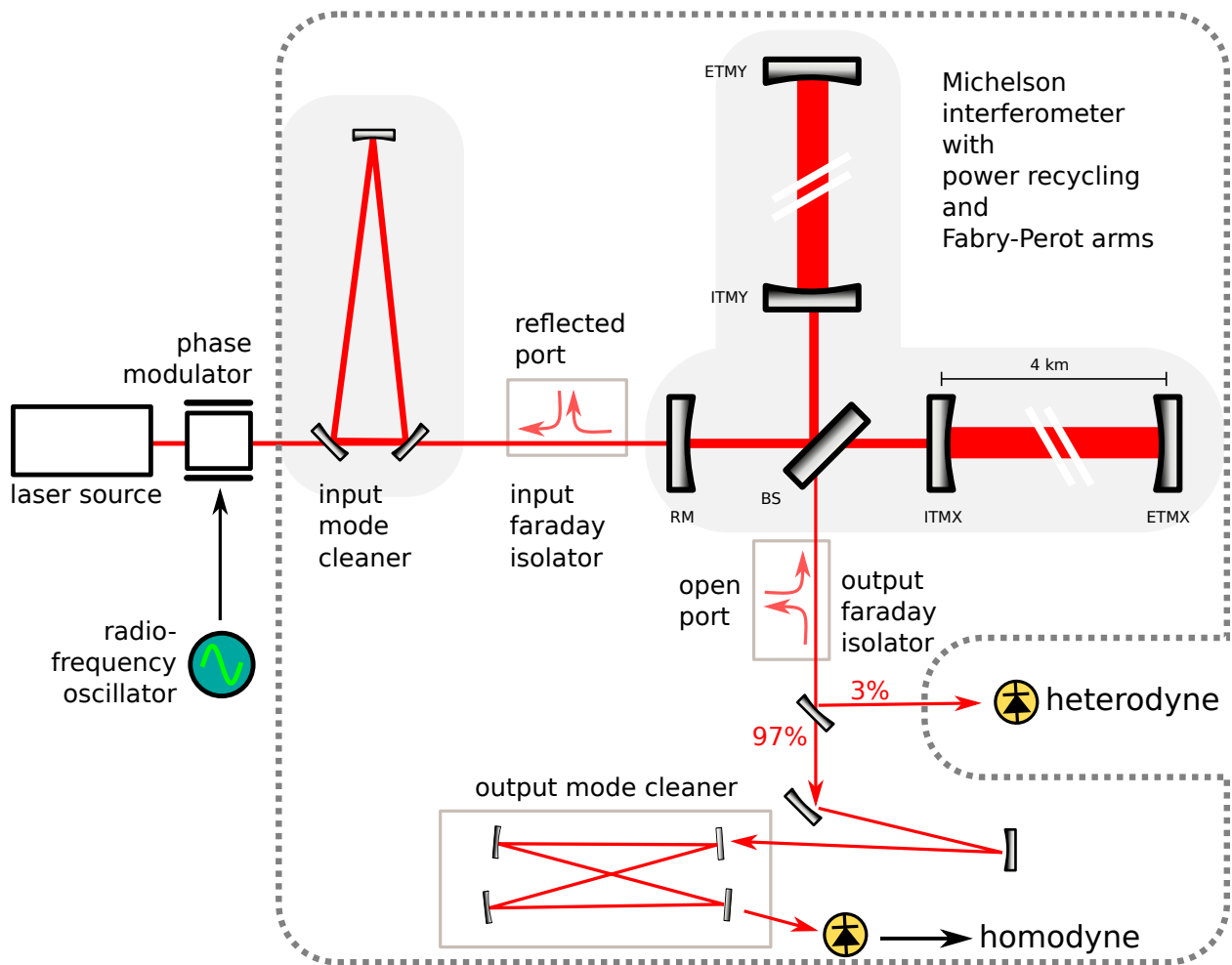


Figure 3.4: Enhanced LIGO interferometer layout (not to scale). The dotted line represents the vacuum enclosure.

Taking the derivative, we find the optical gain

$$S_{DC} = \frac{\partial P_{AS}}{\partial x} \quad (3.4)$$

$$= 2P_{BS}r_c^2 \sin(g_\phi kx) \cos(g_\phi kx) g_\phi k \quad (3.5)$$

$$= 2r_c g_\phi k \sqrt{P_{BS} P_{AS}} \cos(g_\phi kx) \quad (3.6)$$

$$= 2r_c' k \sqrt{P_{BS} P_{AS}} \cos(g_\phi kx) \quad (3.7)$$

The cosine term is very near unity and can be neglected. Also, the phase gain dies off with the cavity pole; and P_{BS} is related to the input power P_{IN} via the power recycling gain g_{cr}^2 . Putting this together, we get:

$$S_{DC}(f) = 2g_{cr}r_c' k \sqrt{P_{IN} P_{AS}} \left(1 + i \frac{f}{f_c}\right)^{-1} \quad (3.8)$$

We see that the optical gain scales with the square root of both input power and the power at the AS port (assuming that the power recycling gain g_{cr} remains constant, which is approximately true for small offsets). From this we can conclude several properties of DC readout immediately:

- Because the optical gain and the shot noise ASD both scale with $\sqrt{P_{AS}}$, the shot-noise-limited sensitivity is insensitive to the particular DARM offset we use.
- The sensitivity of the detector improves with the square root of the input power.
- The frequency response of the interferometer is the same in DC readout as in RF readout, up to a scaling factor. (Both are shaped simply by the cavity pole.)

3.5 Selecting the DARM Offset

The particular DARM offset used to implement DC readout must satisfy a number of conditions. On one hand, the DARM offset cannot be too small:

- The LO field should be of much greater magnitude than the contrast defect field, i.e. we must have $r_c^2 \sin^2 \phi_- \gg (\Delta r/2)^2 \cos^2 \phi_-$, i.e. $\tan \phi_- \gg (\Delta r)/(2r)$. If this condition is not met, then the SNR will suffer from the contrast defect shot noise contribution.
- The phase offset must be sufficiently large that the response to a normal range of DARM motion remains linear. In particular, the DARM offset must be much larger than any expected DARM excursion. The observed residual DARM motion is depicted in figure 3.5; we use 0.1 pm as an upper limit on the residual DARM motion.
- The power on the detection photodiode must be large enough such that the shot noise exceeds the electronics noise of the readout.

On the other hand, there are also upper limits to the magnitude of the DARM offset, including:

- The power loss at the AS port must be sufficiently small such that the power recycling gain is not diminished excessively. Excess power loss will lead to diminished shot-noise-limited SNR.
- The power on the detection photodiodes cannot be too high. Too much power on the photodiodes usually produces excess noise or reduced quantum efficiency, or will even burn the photodiode.
- Larger offsets generally increase all of the (laser and oscillator) noise couplings and increase the magnitude of optical spring effects. To keep noise couplings small, offsets should generally be kept as small as possible.
- The cavity detuning should be small compared to the cavity pole to avoid losing phase gain. In practice, all of the other criteria will become limiting before this one.

Several of these criteria are examined in greater detail below. In practice, the space of allowed offsets is explored empirically; colloquially, we turn the knobs in whatever direction makes the noise go down. During Enhanced LIGO, we operated with a DARM offset of approximately 10 picometers.

3.5.1 Decrease in Arm Power Due to Off-Resonance Operation

The decrease in buildup for a cavity operated off-resonance goes like $(2\mathcal{F}/\pi)^2\phi^2$, where ϕ is the cavity detuning. For $\mathcal{F} = 220$ and $\phi = (2\pi/1064 \text{ nm})(10 \text{ pm})$, the fractional power loss is only 7×10^{-5} .

3.5.2 Decrease in Power Recycling Gain Due to Intentional Offset

Allowing power to escape the power recycling cavity (PRC) through the AS port effectively increases the losses of the PRC, diminishing the power recycling gain.

The carrier power in the PRC is given by

$$P_{BS} = P_{IN} \left| \frac{t_{RM}}{1 - r_{RM}r_{IFO}} \right|^2 \quad (3.9)$$

where t_{RM} is the amplitude transmissivity of the recycling mirror, r_{RM} is its reflectivity, and r_{IFO} is the amplitude reflectivity of the rest of the Fabry-Perot Michelson interferometer. The power-recycling cavity is designed to be critically coupled, so $r_{IFO} \approx r_{RM}$.

With a DC offset in place, the reflectivity of the Michelson becomes $r_M = r_{IFO} \cos \phi_-$, so we can write

$$P_{BS}(\delta x) \approx P_{IN} \frac{T_{RM}}{(1 - R_{RM} \cos(2 \cdot 137 \cdot k \cdot \delta x))^2} \quad (3.10)$$

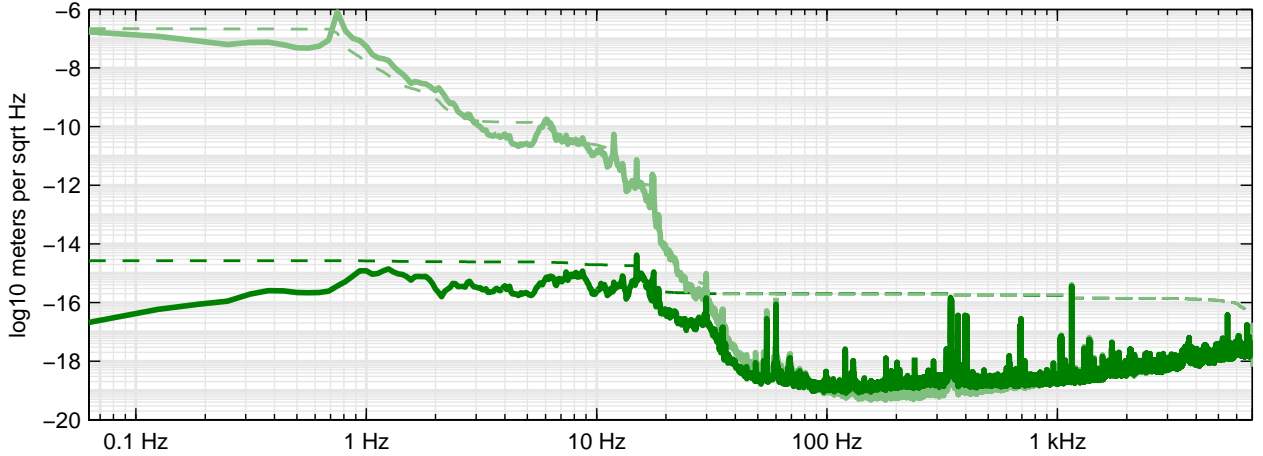


Figure 3.5: DARM motion. The lower trace shows the residual motion of DARM after stabilization by the DARM control loop. The upper trace shows the ‘calibrated’ DARM, in which the effect of the control loop has been removed by multiplying by $(1 + G)$, where G is the open loop gain; this can be interpreted as ‘the motion that would be there if there were no control loop.’ The control loop reduces the RMS DARM motion by ten orders of magnitude in order to hold the interferometer within the linear regime around the operating point. The DARM offset used to implement DC readout must be significantly larger than the RMS residual motion ($\sim 10^{-14}$ m) to avoid nonlinear effects.

The loss of power recycling gain becomes significant for large offsets. For a 10 pm offset, the reduction in power recycling gain is only 1%, but for a 50 pm offset it grows to 20%.

3.5.3 Nonlinearity of the DC Error Signal

Although we operate sufficiently far from the dark fringe that the linear coupling of residual DARM motion to output power is dominant, sufficiently large motion could produce second-order coupling.

To find the nonlinear contribution, we can expand the power at the AS port to include the quadratic term, and then we can compare the quadratic term to the linear term. Here it is easiest to simply work in terms of the phase difference at the beamsplitter, ϕ . Expanding the fringe around the phase offset ϕ_0 ,

$$\sin^2 \phi \approx \sin^2 \phi_0 + 2(\cos \phi_0 \sin \phi_0)\delta\phi + (\cos^2 \phi_0 - \sin^2 \phi_0)(\delta\phi)^2 + \dots \quad (3.11)$$

where $\delta\phi = \phi - \phi_0$, we find that the ratio of the quadratic term to the linear term is

$$\frac{\cos^2 \phi_0 - \sin^2 \phi_0}{2 \cos \phi_0 \sin \phi_0} \approx \frac{1}{2} \cot \phi_0. \quad (3.12)$$

We are interested in the frequency domain contribution of the quadratic part. The spectrum of $(\delta\phi(t))^2$ is the autoconvolution of the spectrum of $\delta\phi(t)$. In practice, most of the spectral power in $\delta\phi(t)$ is at very low frequency (below 1 Hz). Rather than actually compute the autocorrelation, it suffices in practice to multiply the amplitude spectral density of $\delta\phi(t)$ by twice the standard deviation $\delta\phi_{RMS} = \sqrt{\langle(\delta\phi(t))^2\rangle}$ to estimate the amplitude spectral density of $(\delta\phi(t))^2$:

$$\delta\phi(f) * \delta\phi(f) \approx 2\delta\phi_{RMS}\delta\phi(f) \quad (3.13)$$

Using this we can estimate the spectrum of the quadratic contribution as

$$\frac{\text{quadratic}}{\text{linear}} \approx \delta\phi_{RMS} \cot \phi_0. \quad (3.14)$$

DARM motion of 0.1 pm RMS is equivalent to a $\delta\phi_{RMS}$ of

$$\delta\phi_{RMS} = \delta x_{RMS} \times g_\phi \times 2\pi/\lambda \quad (3.15)$$

$$\approx 0.1 \times 10^{-12} \text{ m} \times 137 \times 2\pi/\lambda \quad (3.16)$$

$$\approx 80 \times 10^{-6} \text{ radians} \quad (3.17)$$

while the static DARM offset of 10 pm becomes

$$\phi_0 \approx 10 \times 10^{-12} \text{ m} \times 137 \times 2\pi/\lambda \quad (3.18)$$

$$\approx 8 \times 10^{-3} \text{ radians}. \quad (3.19)$$

and the ratio of the quadratic contribution to the linear contribution is

$$\frac{\text{quadratic}}{\text{linear}} \approx \delta\phi_{RMS} \cot \phi_0 \approx \frac{\phi_{RMS}}{\phi_0} \approx \frac{1}{1000}. \quad (3.20)$$

The ratio of the quadratic contribution to the linear contribution is approximately equal to the ratio of the RMS DARM motion to the static DARM offset. For a reasonable DARM offset, the quadratic contribution is a factor of 1000 below the linear contribution. We would need to worry about fringe wrapping before the quadratic contribution would become significant; the nonlinear response of DC readout due to fringe curvature is negligible.

Chapter 4

Output Mode Cleaner

4.1 Introduction

The optical fields in the interferometer are intended to exist in only the fundamental Gaussian spatial mode. A critically coupled resonant cavity, the input mode cleaner, is used to attenuate any higher order spatial modes produced by the laser before the field is incident on the interferometer. Despite having an essentially pure input beam, imperfections in the interferometer optics leads to the production of higher order spatial modes in the interferometer; this effect is particularly egregious for the RF sidebands in the power recycling cavity[72]. As a result, the output beam (depicted in figure 4.1) is no longer in the pure Gaussian mode, but also contains spurious higher order modes.

The spurious higher order spatial modes in the output beam are detrimental to interferometer performance as they generally produce no useful signal, but contribute additional photon shot noise, increase the power that needs to be detected, and exacerbate noise couplings. To mitigate these effects, an *output mode cleaner* (OMC) was installed at the output port. This critically-coupled optical filter cavity attenuates higher order spatial modes before the beam is detected by a pair of photodiodes. In DC readout, the OMC is also used to remove the RF sidebands, which are still needed in the interferometer to sense other degrees of freedom, but would only be detrimental to the DC readout signal.

4.2 Physical Design of the Cavity

A four-mirror bow-tie arrangement was chosen for the mode cleaner design¹, depicted in figure 4.2a. This non-colinear design prevents direct reflection of rejected light back into the interferometer. A design with an even number of mirrors was preferred so that odd-parity transverse modes are degenerate, reducing the density of higher-order-mode resonances. A sufficiently high angle of incidence of the beam on the mirrors is necessary to minimize the

¹The Enhanced LIGO OMC design and construction was lead by Sam Waldman as part of LIGO's Interferometer Sensing and Control (ISC) group.

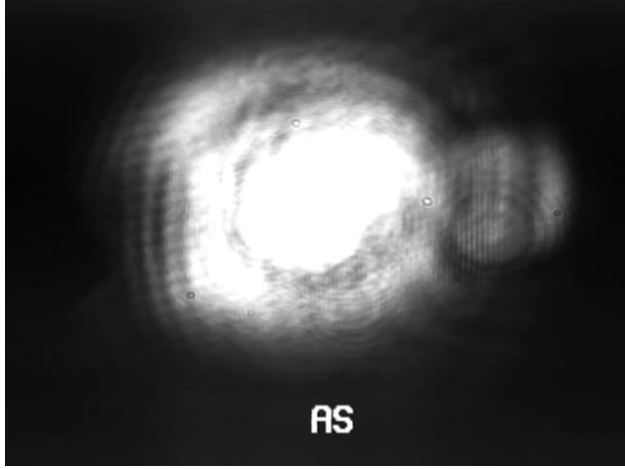


Figure 4.1: Image of the beam spot at the L1 output port taken using a CCD camera. This image is saturated in the central portion but emphasizes the spurious higher order modes surrounding the fundamental Gaussian, including contributions from both the carrier and the 25 MHz sidebands.

effects of small-angle scattering, subject to the constraint that too great an angle of incidence will introduce excessive astigmatism to the beam.

The cavity was constructed by rigidly mounting the cavity optics and photodetectors to a baseplate, similar² to the LISA optical bench design[75]. The baseplate is a slab of Corning ULE glass 450mm × 150mm × 39mm; components were bonded using Optocast 3553LV-UTF-HM UV-cure epoxy.

Two of the cavity mirrors are outfitted with position actuators: a fast, short-range ($\lesssim 0.1$ μm) PZT, and a slow, long-range ($\approx 20\mu\text{m}$) thermal actuator consisting of a 1 inch long segment of aluminum tube warmed by a resistive heater.

To isolate the mode cleaner from environmental disturbances, the optical bench was hung from an actively-damped double-pendulum suspension system[76, 77], which was in turn suspended by an in-vacuum active isolation system[44, Chapter 5].

The photodiodes were also mounted on the OMC baseplate, and read out by in-vacuum preamplifiers. The output from the mode cleaner was split via a 50/50 beamsplitter and directed to two Perkin Elmer 3mm diameter InGaAs photodiodes (part number C30665GH), with measured quantum efficiency > 0.95 at 1064 nm. The photocurrent was converted to voltage across 100Ω transimpedance. Subtraction of the signals from the two photodiodes produces a diagnostic “nullstream” containing the anti-correlated component of the PD signals. The rigid mounting of the PDs to the OMC baseplate reduces the possibility of beam motion coupling to photocurrent through photodiode nonuniformities, and the in-vacuum preamplifiers reduce the likelihood of electronic or triboelectric noises.

²One important difference is that the LIGO OMC uses an epoxy adhesive to attach the optics to the baseplate, while the LISA optical bench uses hydroxide-catalysis bonding[73, 74].

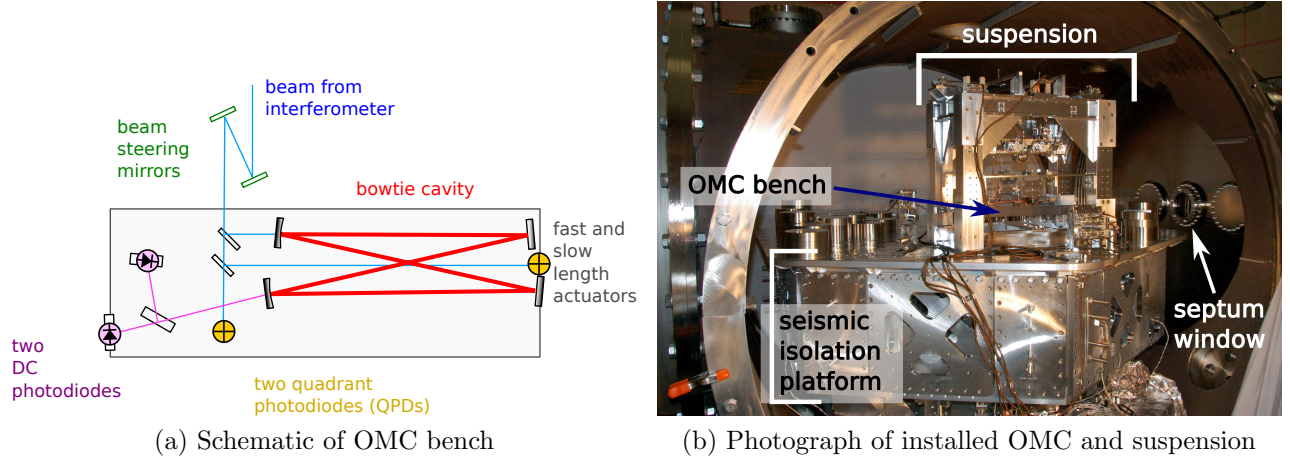


Figure 4.2: (a) Diagram illustrating the design of the monolithic OMC bench; (b) Photograph of the installed output mode cleaner, suspension, and seismic isolation platform. The OMC is located in a dedicated vacuum chamber, separated from the main vacuum enclosure by a septum window, allowing rapid venting cycles during commissioning.

A photograph showing the installed OMC, suspension, and in-vacuum seismic isolation platform is presented in figure 4.2b.

4.3 Requirements

The OMC is required to sufficiently filter the light present at the output port such that contributions from the RF sidebands and higher-order spatial modes become negligible. To exclude the RF sidebands, the cavity length is chosen such that the RF sideband frequencies are anti-resonant in the cavity, which yields minimum transmission.

Table 4.1: Designed and measured properties of the Hanford and Livingston output mode cleaners.

parameter	design	H1	L1	units
perimeter (p)	1.042	1.077	1.016	m
beam waist (w)	477	496	463	μm
Finesse (\mathcal{F})	400	360	360	
FSR	287.7	278.3	295.2	MHz
cavity pole	360	390	410	kHz
g-factor	0.739	0.725	0.722	
HOM freq shift	69.4	67.2	71.8	MHz
transmission	1	≥ 0.95	≥ 0.90	

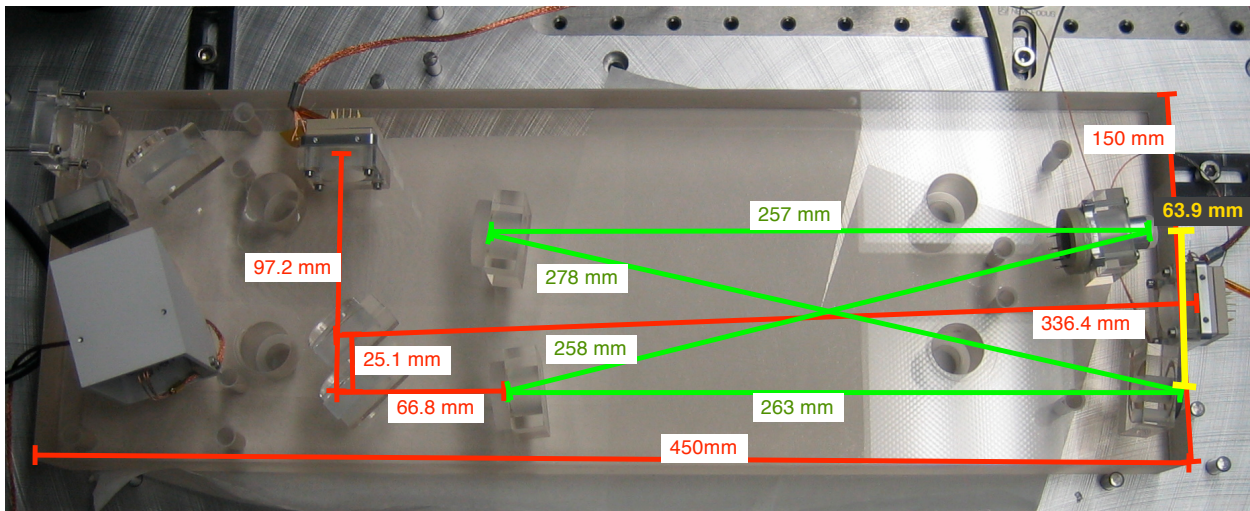


Figure 4.3: Photograph of the Output Mode Cleaner used at Livingston (*ex situ*). Only one of the two DC photodiodes is installed in this photo. Photometry by Sam Waldman; this diagram has document number D0901817.

4.4 Choosing the OMC Finesse

All else being equal, we want the best possible filtering capability from the OMC.

The transmission of a lossless critically-coupled cavity is given by

$$T = \frac{1}{1 + \frac{4}{\pi^2} \mathcal{F}^2 \sin^2 \phi} \quad (4.1)$$

where \mathcal{F} is the cavity finesse and ϕ is the cavity's detuning from resonance. Since the cavity will be locked to resonance for the laser carrier, to find the attenuation of other modes, we set ϕ to the detuning of these modes.

The maximum attenuation of a mode is given by $(4/\pi^2)\mathcal{F}^2$.

After filtering by the OMC, we want the shot noise contributions from unneeded modes to be negligible, and the contribution from noises on these fields to also be negligible. Almost any cavity would be sufficient to reduce excess shot noise contributions. The need for a high finesse OMC comes from the need to eliminate audio frequency noises carried on the RF sidebands and higher-order spatial modes.

Consider the contribution of intensity noise on the RF sidebands. Any residual intensity noise on the RF sidebands will contribute directly to the DC readout signal. Assume that the carrier has about 100 mW power and that the RF sidebands have about the same amount of power, and assume that the laser intensity noise is 10^{-7} RIN. The shot noise RIN on 100 mW is (per equation E.12) $\sqrt{2h\nu/P} \approx 2 \times 10^{-9}$. Thus we need to attenuate the RF sidebands by at least a factor of 100.

The RF sidebands will not be exactly anti-resonant in the cavity but will actually lie at about $0.1fsr$ away from the carrier. Thus the attenuation is diminished by approximately $\sin^{-2}(0.1\pi) \approx 10$. So we need attenuation of 1000. But we really want at least a factor of 10 margin, so we'll want maximum attenuation of 10000. This means we need a finesse of at least 160.

On the other hand, higher finesse lead to greater net power loss as the beam travels through the cavity, as the intra-cavity loss is multiplied by each effective roundtrip in the cavity. To choose the finesse, we assume a roundtrip intra-cavity power loss of 100pm and set the constraint that the net power efficiency of the OMC should exceed 99% (not actually achieved). This leads to the design choice of a finesse of 400.

4.5 Choosing the OMC Length and Geometry

The cavity length is chosen to provide adequate attenuation of the RF sidebands, and its geometry (*g*-factor) is chosen to sufficiently attenuate higher-order modes. The optimal *g*-factor depends on the specific details of the frequency and spatial spectrum of modes at the output port. These depend strongly on the details of the interferometer optics, alignment, and thermal state.

To deal with these unknown factors, we designed the OMC using a model in which the power in each higher order mode (of order n) was proportional to $1/n^2$ and the RF sidebands had their nominal power. The designed and as-built properties of the output mode cleaner cavities are given in Table 4.1. One disadvantage of the chosen design is that the 4-th order mode is nearly degenerate with the fundamental mode. We did experience problems with accidental degeneracy in one of the mode cleaners, which was addressed by changing the operating temperature of the thermal actuator (which had a small coupling to the effective radius of curvature of the mirror). The next version of the output mode cleaner will be designed with a slightly different *g*-factor to avoid this problem.

4.6 OMC Feedback Control Systems

The mode cleaner was controlled and the DC readout signals were acquired using a prototype of the advanced LIGO real-time digital signal processing system, consisting of a Linux-based computer equipped with analog-to-digital and digital-to-analog converters and interfaced to other systems via reflected memory over a fiber ring and EPICS over ethernet, operating at 32768 samples per second (Hz) The LIGO Realtime Code Generator[78, 79] allowed fast prototyping and implementation of complex servos. All servos involving the OMC were implemented using this digital system.

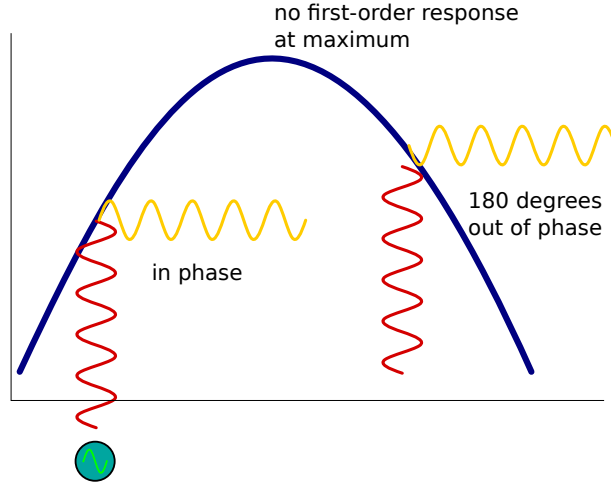


Figure 4.4: Cartoon view of dither locking. The dither locking technique allows a system to be locked to a quadratic operating point. For example, dither locking is used to control the OMC cavity length, where, near resonance, transmission is a quadratic function of cavity displacements. A sinusoidal modulation is injected into the parameter we wish to tune (i.e. cavity length), and the output (i.e. transmitted light intensity) is demodulated at the same frequency, producing an error signal. The figure shows the phase-flip that occurs as the system moves through the quadratic point. At the quadratic point, the error signal is zero, while on either side it attains nonzero values with opposite signs.

4.6.1 Length Sensing and Control (LSC)

The cavity length must be controlled to maintain the resonance of the laser carrier. To sense the mismatch between the laser carrier frequency and the cavity length, we modulate the cavity length by a small displacement at high (audio) frequency and monitor the transmitted light intensity for a signal at the same frequency. Because cavity transmission is a quadratic function of the frequency/length mismatch, there will be no first-order response in the transmission when the laser light is perfectly resonant in the cavity. If, on the other hand, the cavity is slightly off resonance, there will be linear dependence of the transmitted intensity on the modulation of the cavity length; a cartoon of this effect is shown in figure 4.4. Because the sign of this linear coupling changes as the cavity goes through resonance, the signed amplitude of the modulation in the transmitted light provides an error signal for the cavity tuning. Effectively, we sense the first derivative of the transmission with respect to cavity length.

Modeling the Dither Locking

Suppose $f(x)$ is a function we wish to maximize; in this case, f gives the power transmitted through the OMC as a function of length offset. We let $x = x_0 + A \cos \omega t$, where A is the

amplitude of the dither and ω is its frequency. We can expand f as a power series around x_0 :

$$f(x) \approx f(x_0) + f'(x_0)(x - x_0) + f''(x_0)(x - x_0)^2 + \dots \quad (4.2)$$

$$\approx f(x_0) + f'(x_0)A \cos \omega t + f''(x_0)A \cos^2 \omega t + \dots \quad (4.3)$$

The amplitude of the $\cos \omega t$ term is proportional to the first derivative of f at the current operating point. (There are also contributions from higher derivatives, but we assume the lower derivatives dominate.)

Noise limits

Suppose the OMC has coefficient of finesse F and P watts on the photodiode. The dither amplitude is A and dither frequency is ω . What is the sensing noise limit?

The background is Gaussian white shot noise, equally distributed into the two demodulation quadratures. So the noise floor of the demodulated signal is $(1/\sqrt{2})\sqrt{2h\nu P}$.

The transmission of the OMC goes like $T(x) = 1/(1 + Fx^2)$ which has first derivative $T'(x) = 2Fx/(1 + Fx^2)^2 = -2Fx + O(x^2)$. Thus the optical gain is $-2FA$ watts per meter.

The fast PZT actuator is dithered at 10 kHz and this signal is synchronously demodulated in the transmitted light. The bandwidth of the servo is about 100 Hz.

4.7 Input Beam Alignment Sensing and Control (ASC)

In addition to controlling the cavity length to keep the carrier resonant, we must control the pointing of the beam incident on the OMC. Aligning the input beam to the OMC is a significant problem, since the OMC can only clean the light insofar as we can identify the mode we want to keep.

The decomposition of a given optical field into Hermite-Gauss eigenmodes is dependent upon a choice of origin and spot size. The OMC cavity will select the projection of the incident field onto its eigenmode. The optics directing the interferometer output beam to the OMC

Several OMC alignment schemes were implemented and utilized.

4.7.1 QPD Alignment

The simplest alignment control simply uses the two quadrant photodiodes (QPDs) mounted on the OMC breadboard. These are simply photodiodes whose surfaces are divided into four quadrants. By subtracting the power seen on one half of the QPD face from the power seen on the other half, we can measure the position of the incident beam.

Alignment servos based on the QPDs have the advantage of being very robust and not requiring that the OMC already be locked, and so are ideal for initial alignment of the OMC

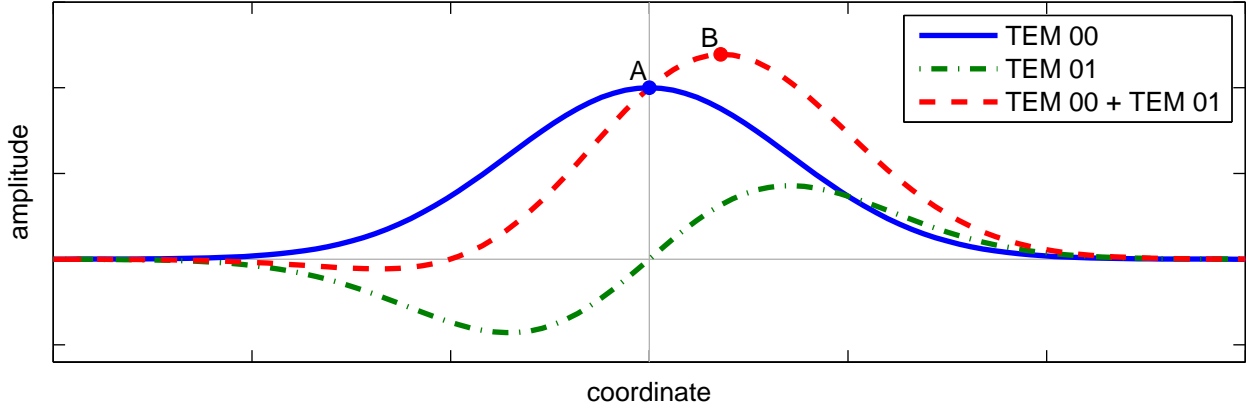


Figure 4.5: The sum of a gaussian and a first-order higher order mode resembles a displaced gaussian. A basic dither alignment scheme, which maximizes the power transmitted through the OMC, would operate near point B, rather than point A.

before locking the cavity. The QPD alignment, however, has no notion of the ideal DC pointing of the beam and is sensitive not just to the carrier, but also the RF sidebands.

4.7.2 Dither Alignment

A second alignment scheme is to dither the two steering mirrors each in pitch and yaw, demodulate the OMC transmitted signal at these frequencies, and feed back to the mirrors—exactly analogous to the operation of the OMC length control system.

The basic dither alignment scheme has some attractive features, but does not work properly in the presence of spurious higher order modes—the exact problem which motivates the use of the OMC in the first place.

Dither alignment works maximizes the power transmitted through the OMC; because this is a quadratic maximum of transmission versus pointing, the linear coupling of beam jitter to the transmitted intensity is nulled. However, this technique cannot distinguish between the optical field coming from the interferometer arms, and any higher order modes of the carrier resonant in the PRC. If there is carrier power in the TEM01 mode, this servo will misalign the input beam slightly, to convert the incident TEM01 mode into the TEM00 mode of the cavity. (The conversion of TEM01 to TEM00 via beam displacement is depicted in figure 4.5.)

4.7.3 Drumhead Dither OMC Alignment System

From the experience with basic dither alignment, it is clear that what is needed is some alignment system which can specifically detect the arm cavity mode. To accomplish this, we ‘tag’ the light in the arm cavity by modulating the arm length at high frequency and looking for this modulation in the light transmitted through the OMC.

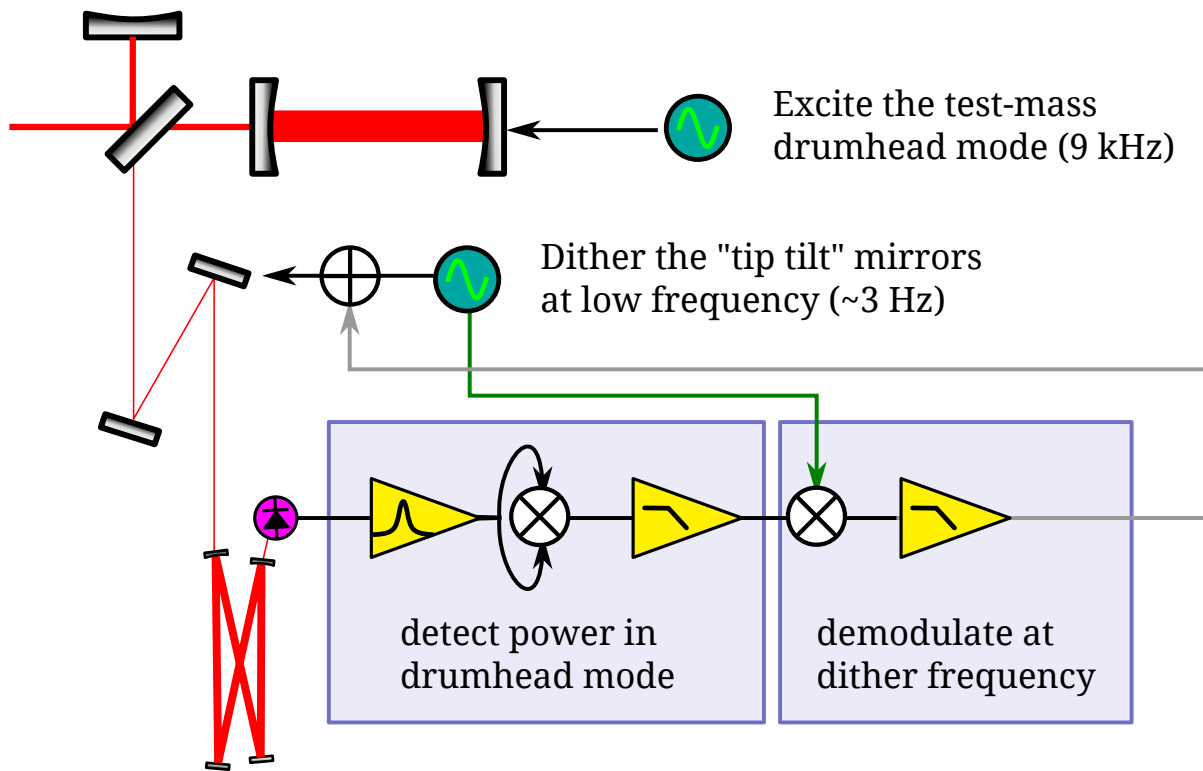


Figure 4.6: The ‘Drumhead dither’ OMC alignment system.

The system was implemented as follows:

1. One of the arm cavity lengths is modulated at high frequency, 9 kHz. Intuitively, this modulation ‘tags’ the carrier light emerging from the arm. The modulation is accomplished with a small drive by feeding the mechanical drumhead mode of the test mass. (This gives rise to the nickname of the method, ‘drumhead dither’.)
2. The spectral power of the 9 kHz line in the OMC photodiode signal is measured by bandpassing the signal around 9 kHz, squaring the result, and then low pass filtering.
3. The four degrees of freedom of the two beam steering mirrors are modulated (dithered) at a frequency slow compared to the low pass filtering in step (2).
4. The measured power in the 9 kHz line is demodulated at the steering mirror dither frequencies, producing alignment error signals which are fed back to the mirrors.

This system is depicted in figure 4.6.

It has been pointed out [80] that even the drumhead dither alignment scheme is not optimal in the sense of producing the best shot-noise-limited SNR.

4.8 Scattering

Viewed from the output port, the interferometer appears almost perfectly reflective. Any light scattered (i.e. retroreflected) by the output optics at a small angle could scatter into the interferometer mode, reflect off of the interferometer, joining (and interfering with) the main interferometer signal and LO beam. Any modulation of the path length between the main interferometer and the backscatterer will change the interference condition, producing intensity variations in the OMC transmitted beam and contaminating the DARM readout.

Measuring the OMC Scattering Reflectivity

The backscattering reflectivity of the OMC can be experimentally measured by intentionally modulating the path length between the interferometer and the OMC. This produces phase modulation in the backscattered field. This phase-modulated field reflects from the interferometer and combines with the local oscillator field.

The backscattered beam has an electric field amplitude of

$$E_s = aE_0 \exp \left\{ i \frac{2A}{\lambda} (2\pi) \sin \Omega t \right\} \quad (4.4)$$

where A is the amplitude (in meters) of motion of the scatterer, Ω is the frequency of motion, and a is the amplitude reflectivity of the scattering source (the scattering coefficient). This

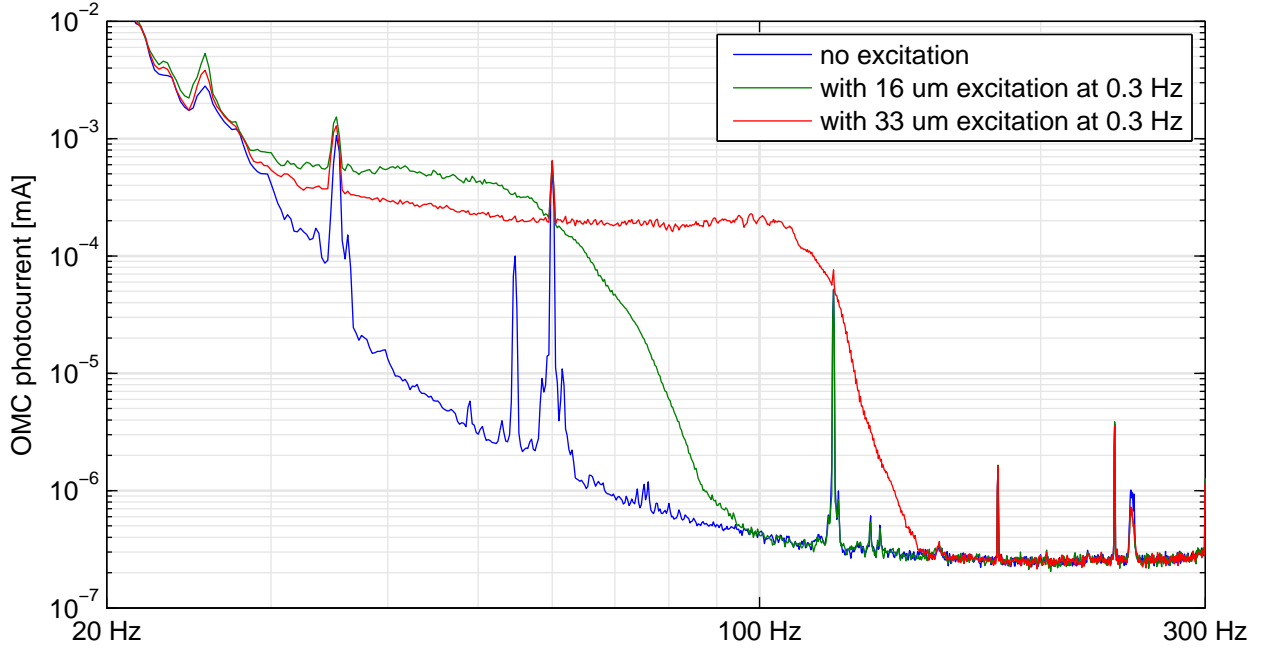


Figure 4.7: Measurement of effective OMC backscattering reflectivity. With the interferometer operating in low-noise mode, we excited (modulated) the position of the OMC in the direction of the incident beam, thus modulating the path length between the interferometer and the OMC. This produces the characteristic ‘scattering shelf’ spectrum in the power at the OMC photodiodes. Integrating the area under the shelf and dividing by the DC power gives the effective backscattering reflectivity. (The photocurrent has been corrected for the suppression of the DARM control loop.)

is phase modulation with a modulation depth of $\Gamma = 4\pi(A/\lambda)$ radians, assuming normal incidence on the scatterer. The photodiode detects the power in the resulting field, which is

$$P = |E_t + E_s|^2 \quad (4.5)$$

$$= |E_t|^2 + |E_s|^2 + 2 \operatorname{Re} E_t E_s \quad (4.6)$$

$$= |E_0|^2 + 2 \operatorname{Re} E_t E_s \quad (4.7)$$

where $E_t = (1 - a)E_0$ is the field that’s transmitted rather than scattered. Using the Jacobi-Anger identity, E_s can be expanded in terms of sinusoids to find the power spectrum of the photodiode signal:

$$P = |E_0|^2 + 2 \operatorname{Re} E_s E_t^* \sum_{n=-\infty}^{\infty} i^n J_n(\Gamma) \exp in\Omega t \quad (4.8)$$

$$= |E_0|^2 + 2|E_0|^2 a(1 - a) \operatorname{Re} \sum_{n=-\infty}^{\infty} i^n J_n(\Gamma) \exp in\Omega t \quad (4.9)$$

We are interested not only in the case of small modulation depth (i.e. small motion of the scatterer), but also very large modulation depths, greater than the wavelength of the light, which produces many higher order harmonics. Spectrally, this looks like a comb of delta functions at integer multiples of Ω , whose amplitudes are given by bessel functions $J_N(\Gamma)$ with $N = f/\Omega$. Any noise on the carrier will get superimposed on each of these spikes, smoothing out the observed spectrum.

Large motion of a backscatterer produces a characteristic ‘shelf’ feature in the PD spectrum (c.f. figure 4.7). This is because the amplitude of Bessel functions $J_N(\Gamma)$ dies off very steeply with N after $N > \Gamma$, creating the characteristic ‘scattering shelf’. The cutoff (‘knee’) frequency therefore occurs when $N \approx \Gamma$; the knee frequency may be calculated as follows:

$$f_{knee} = \Omega N_{knee} \quad (4.10)$$

$$= \Omega \Gamma \quad (4.11)$$

$$= 4\pi \Omega (A/\lambda) \quad (4.12)$$

Another way of seeing this is to consider the (time dependent) phase induced by the scatterer and take its derivative to find the maximum frequency shift due of the backscattered light:

$$\phi = \Gamma \sin \Omega t \quad (4.13)$$

$$f_{instantaneous} = d\phi/dt = \Omega \Gamma \sin \Omega t \quad (4.14)$$

$$\max f_{instantaneous} = \Omega \Gamma \quad (4.15)$$

which gets the same result. An excitation of amplitude A and frequency Ω has maximum velocity $v = A\Omega$. This can be used to eliminate both A and Ω from the knee frequency:

$$f_{knee} = 4\pi(v/\lambda) \quad (4.16)$$

Of course, we are more interested in determining the backscattering reflectivity than details of the resulting spectrum. There are two principle ways to recover the scattering reflectivity: (1) Because $\sum J_N(\Gamma)^2$ over all N equals 1, we can integrate the power spectrum of the photodiode signal to directly measure $2|E_0|^2 a(1 - a)$. We can then divide by the DC term ($|E_0|^2$) to get the scattering coefficient. (2) We can simulate the scattering process in the time domain, find the spectral density of the resulting signal, and fit the model to the observed spectrum.

This procedure was carried out using the actuators in the table supporting the OMC to produce modulations in the direction of the incoming beam of 16 microns at 0.3 Hz and 33 microns at 0.3 Hz; the resulting OMC transmitted spectra are shown in figure 4.7 along with a quiescent spectrum for reference. (The experiment was repeated with modulations in orthogonal directions; as expected, the effect was much less than the modulation in the beam direction.)

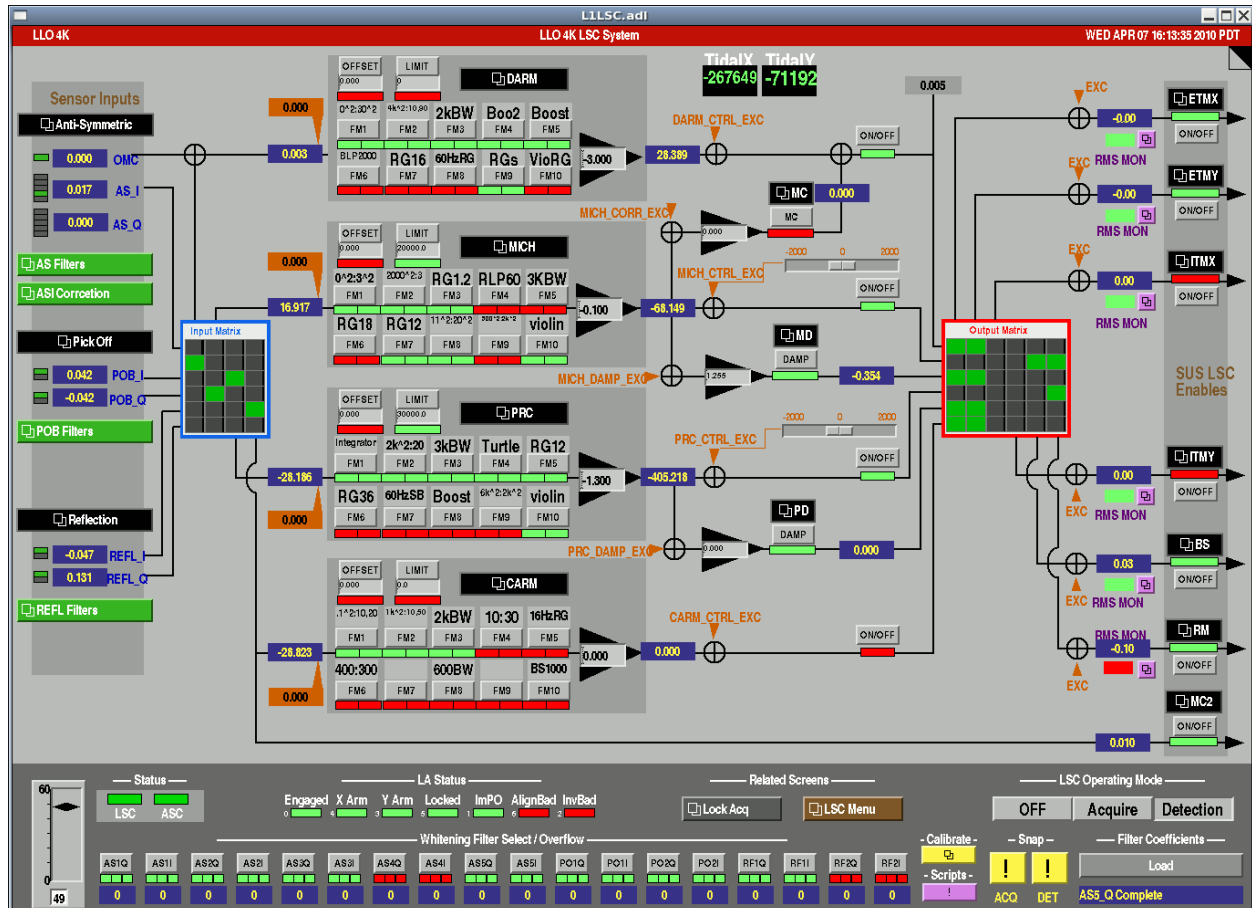


Figure 4.8: The control screen for the Length Sensing and Control subsystem at Livingston. The control screen depicts signal flow in a generally left-to-right manner. Photodiodes at the anti-symmetric (AS), pick-off (PO), and reflected (REFL) ports are indicated on the extreme left. These signals are combined via an input matrix to form the DARM, MICH, PRC, and CARM degrees of freedom. These signals are processed through an array of filter banks defining the control filters. Finally, the signals pass through an output matrix and are then directed to the individual optics.

4.9 Beam Diverter

When the interferometer loses lock, the stored power must be dumped somewhere. Typically, due to the presence of the power recycling mirror, the stored power comes out the output port. This high-power transient is sufficiently strong to burn the detection photodiodes. In order to prevent this, one of the steering mirrors is used as a fast shutter. It is able to zero the transmission through the OMC in approx 2 ms.

4.10 The Front End

To achieve the touted SNR improvement of DC readout it is imperative that the signal not be lost to optical losses, non-optimal photodiode quantum efficiency, or electronics noise.

4.10.1 Photodiodes

Sub-optimal photodiode efficiency counts as a loss just like any other optical loss.

The OMC photodiodes are configured in a reverse-biased, photoconductive arrangement. An ideal photodiode in such a configuration will allow one charge carrier to cross the junction for each incident photon. The ratio of photocurrent to incident power on the photodiode is its *responsivity*. The ratio of a photodiode's actual responsivity to the ideal is its *quantum efficiency*. At 1064 nm the ideal responsivity is

$$\frac{q_e}{h\nu} = \frac{q_e\lambda}{hc} \approx 0.86 \text{ Amps/Watt} \quad (4.17)$$

where $q_e \approx 1.6 \times 10^{-19}$ C is the electron charge.

One lesson (re-)learned during Enhanced LIGO is the need to measure the characteristics of every individual noise-sensitive component installed in the final machine rather than relying on measurements of test samples or typical values. The photodiodes we originally installed turned out to have quantum efficiency $\lesssim 0.60$ while the test articles of the same part number had quantum efficiency within a few percent of unity. Clearly there had been some change in the manufacturing process that resulted in a greatly diminished quantum efficiency. Even for parts which do not show such a dramatic systematic change, characteristics of individual parts come from some distribution, and by measuring a batch of parts, the lowest noise components can be hand picked.

In September 2009 we replaced the bad photodiodes. The replacement photodiodes are Perkin Elmer 3mm InGaAs diodes, part number C30665GH. The measured quantum efficiency was consistent with unity [81].

4.10.2 Electronics

An optical power of 100 mW on the readout photodiodes will produce a photocurrent of $i = q_e\lambda/(hc) \cdot 100 \text{ mW} = 86 \text{ mA}$, which in turn has a shot noise floor of $\sqrt{2q_e i} \approx 500 \text{ pA}/\sqrt{\text{Hz}}$.

Across 100Ω transimpedance, this becomes $50 \text{ nV}/\sqrt{\text{Hz}}$. The noise floor of the readout electronics must be below this level and not be polluted by any baseband $1/f$ flicker noise.

The main strategy is to aggressively amplify the electronic signal as close to the photodiodes as possible, so that noises added downstream become insignificant. To eliminate even triboelectric effects, the first preamp stages are placed in-vacuum. The in-vacuum preamps consist of active filter stages with two zeros at 8 Hz and two poles at 80 Hz, for a factor of 100 amplification at 100 Hz. This is followed by two more pole-zero pairs in satellite amplifiers on the floor outside the vacuum chamber, for a total gain of 10,000 before the long run to the racks.

Chapter 5

DC Readout Performance and Noise Couplings

The coupling of noises from the laser source and RF oscillators to the gravitational wave readout channel differ considerably in RF and DC readouts. In addition, the combination of DC readout with an OMC introduces a greater sensitivity to beam motion (jitter). These couplings are of primary interest in designing the optical readout of a gravitational wave detector.

In this chapter, I sketch the technique for calculating expected noise couplings analytically and numerically, and I will present measurements of these noise coupling measurements made on the two Enhanced LIGO interferometers. I compare the expected and achieved shot-noise-limited sensitivity, verifying that the fundamental and technical shot noise improvements due to homodyne detection and the OMC are realized.

5.1 Sensitivity

The primary figure of merit of a gravitational wave detector is its noise floor, calibrated as a strain spectral density; the noise floor is often referred to as simply the *sensitivity* (despite a lower noise floor indicating better sensitivity). When evaluating DC readout in Enhanced LIGO, we can begin by looking at the noise floor: do we understand the achieved sensitivity? At low frequencies ($f \lesssim 200$ Hz), the interferometer noise floor is limited by displacement noises which will be independent of any readout, while at high frequencies, the noise floor is set by shot noise. The shot-noise-limited sensitivity of a power-recycled interferometer using DC readout is given by a small number of parameters:

- the length of the arm cavities ($L = 3995$ m)
or, equivalently, the free spectral range ($\nu_0 = c/(2L)$)
- the input power to the interferometer (P_{IN})
- the power recycling gain (g_{cr}^2)

- the arm cavity finesse ($\mathcal{F} = 220$)
- the input and output efficiency (ϵ)
- the laser wavelength ($\lambda = 1064 \times 10^{-9}$ m)

where we lump all losses due to absorption, scattering, or imperfect mode-matching, and the photodiode quantum efficiency, into the efficiency ϵ .

The predicted curve is produced by dividing the amplitude spectral density of the shot noise on the detection photodiode (A_{shot}) by the optical gain of the interferometer (S_{DC}). The DC optical gain is (as derived earlier) simply the derivative of the power at the output port with respect to changes in differential arm length, evaluated at the operating DARM offset:

$$A_{shot}(f) = \sqrt{2h(c/\lambda)P_{AS}} \quad (5.1)$$

$$S_{DC}(f) = 2\sqrt{\epsilon P_{IN} P_{AS}} g_{cr} r'_c k (1 + if/f_c)^{-1} \quad (5.2)$$

where $f_c = \nu_0/(2\mathcal{F})$ is the cavity pole, h is Planck's constant, and c is the speed of light. This expression for S_{DC} is in the single-pole approximation, which is valid for frequencies much lower than the arm cavities' free spectral range ($f \ll \nu_0$), and for frequencies above the test mass suspension's pendulum resonance (which may be increased due to radiation pressure).

Combining these two expressions gives the noise floor due to shot noise, calibrated in meters; dividing by the arm length L gives the noise floor in strain:

$$x_{shot}(f) = \frac{1}{2\pi} \sqrt{\frac{\lambda hc}{2\epsilon P_{IN}}} \frac{1}{g_{cr} r'_c} \left| 1 + i \frac{f}{f_c} \right| \quad (5.3)$$

$$h_{shot}(f) = (1/L) x_{shot}(f) \quad (5.4)$$

The shot noise seen at the photodiode has a white spectrum; the entire shape of the shot noise when calibrated as a displacement or strain comes from the calibration (i.e. the optical gain) which in turn is shaped only by the cavity pole. Interferometers using signal recycling will have a more complicated response function.

5.1.1 Measured and Expected Sensitivity

The measured detector noise floors, calibrated as a displacement amplitude spectral density ($m/\sqrt{\text{Hz}}$), along with the expected performance based on equation 5.4 and measured detector parameters, are depicted in figure 5.1. The measured spectra were taken near the time of the detectors' best performance in summer 2010. The parameters used in the model are given in table 5.1.

The comparison reveals that the achieved performance is as expected. However, some comments are in order: The H1 detector was able to operate with about twice as much input

Table 5.1: Interferometer parameters used in the shot noise model.

parameter	symbol	H1	L1
input power	P_{IN}	20.27 W	11.65 W
arm cavity pole	f_c	83.7 Hz	85.6 Hz
finesse	\mathcal{F}_{arm}	224	219
power recycling gain	g_{cr}^2	59	41
carrier fraction after phase modulation	$J_0(\Gamma)^2$	0.94	0.95
input optics		0.82	0.75
interferometer mode-matching		0.92	0.92
output faraday isolator transmission		0.94	0.98
DC readout pickoff fraction		0.953	0.972
OMC mode-matching		0.70	0.95
OMC transmission and PD quantum efficiency		0.95	0.95
net power efficiency	ϵ	0.42	0.56

power as the L1 detector, and had a power recycling gain approximately 40% better than L1's; from this we would expect considerably better shot noise level at H1. However, the H1 detector also experienced anomalously low transmission of the arm cavity mode through the output mode cleaner which contributed to a power efficiency (ϵ) much lower than desired. The poor OMC transmission was due to some combination of poor mode-matching, and high cavity losses which appeared near the end of the science run. These anomalous losses are not understood and are, as of the time of writing, under active investigation.

5.2 Laser and Oscillator Noise Coupling Mechanisms

To compute the frequency response of the interferometer and the expected laser and oscillator noise couplings, we first calculate the amplitudes of the static fields at all points in the interferometer, and then we compute the propagation of small GW signal or noise fields through the interferometer. In general, the small amplitude fields due to GW waves or noises appear in the photodiode signals by beating against the strong static fields, i.e. the laser carrier or the RF sidebands. In other words, the strong laser carrier field or RF sidebands act as local oscillators not just for the intended GW-induced sidebands, but audio-frequency (AF) sidebands introduced through other mechanisms too, including AF sidebands that originate on the light at the input to the interferometer. These noises originating at the input are the subject of this section.

Generically, we refer to any spectral line as a ‘sideband’. For the purpose of analysis, sidebands are divided into radio-frequency (RF) sidebands and audio-frequency (AF) sidebands. The distinction is not actually the frequency of the lines but their magnitude; RF sidebands have some finite amplitude, while audio-frequency sidebands are infinitesimal. When the electric field is incident upon a photodiode, the photodiode will see a beat signal

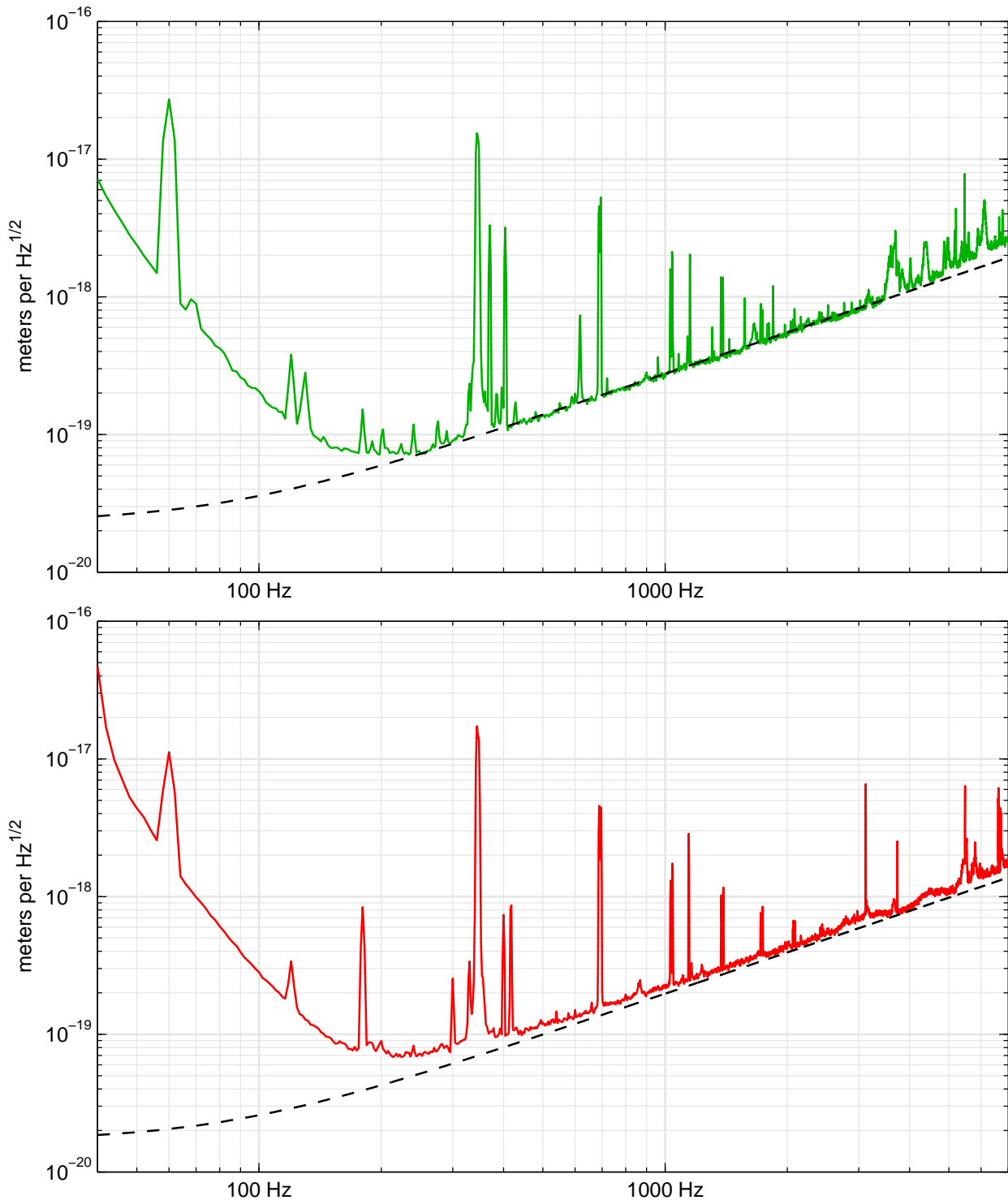


Figure 5.1: Shot noise limited sensitivity of the Livingston and Hanford detectors. The uncertainty in the measured displacement spectra is $\sim 10\%$, and in the modeled curves is $\sim 20\%$.

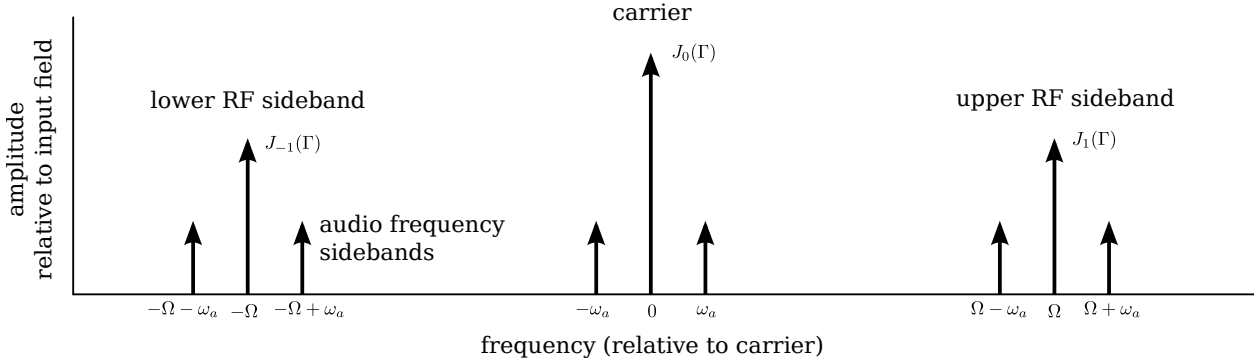


Figure 5.2: Schematic diagram of the laser carrier and RF sidebands, and their associated audio-frequency sidebands.

between every pair of sidebands. In our formalism we make the approximation that the product of any two audio-frequency sidebands is zero. Audio-frequency sidebands are used simply as test fields to evaluate linear transfer functions. They produce signals at PDs by beating against the finite-amplitude RF sidebands.

As detailed in the preceeding chapter, the state of the LIGO interferometer is determined by sampling the electric field at various ports using photodiodes. Pairs of RF sidebands at several distinct frequencies are introduced at the input to the interferometer; interference between these various fields allows the state of the interferometer to be determined. Around the laser carrier, there are two pairs of RF sidebands, each produced through phase modulation: the *resonant sideband* at ~ 25 MHz, which enters the interferometer and emerges at the output port; and the *non-resonant sideband* at ~ 61 MHz, which is mostly reflected by the power recycling mirror.

For an intuitive understanding of the noise couplings to DC readout, we will consider only the resonant sideband, and ignore the residual non-resonant sideband. In numerical simulations, both are included. The arrangement of RF sidebands is depicted in figure ??.

Sidebands are typically created in pairs around a modulated the parent field; and, when incident on a photodiode, they are most conveniently treated in pairs too. Instead of considering the amplitudes of upper and lower sidebands separately, we can instead use a basis where we quantify the sidebands as some amount of amplitude modulation (AM) and some amount of phase modulation.

Optickle

Optickle[82] is an interferometer simulation tool developed by Matt Evans and implemented in Matlab. Optickle uses the first-order approximation described above, and also simulates the effect of optomechanical couplings due to radiation pressure. Optickle was used to make predictions of the laser and oscillator noise couplings in Enhanced LIGO. Optickle was

extended to include the effects of couplings due to servo controls systems by Lisa Barsotti, Nicolás Smith, and myself.

5.2.1 Laser Noises

The Michelson-based design of laser interferometer gravitational wave detectors is attractive due to its high common mode noise rejection. A Michelson interferometer with identical arms would completely isolate the output port from common-mode noises (i.e. noise introduced at the input port). Any asymmetries between the arms will introduce couplings of noises at the input port to the output port. Some such asymmetries are unintentional, such as the difference in finesse or reflectivity of the arms; intentional DARM and MICH asymmetries are introduced in order to allow the local oscillator (RF or carrier) to read the output port.

Laser Intensity Noise

Coupling of laser intensity noise to the output port is one of the easiest couplings to understand. The dominant mechanisms (in the absence of radiation pressure effects) are:

- Below the coupled-cavity pole ($f_{cc} \approx 1$ Hz), carrier power fluctuations are transmitted directly to the output port, attenuated only by the ratio P_{AS}/P_{IN} . Above the coupled cavity pole, transmission of AM on the carrier is attenuated by $1/f$.
- The resonant RF sidebands and any modulation they carry reaches the output port attenuated only slightly, since the Michelson is arranged (via the Schnupp asymmetry) to conduct the RF sidebands to the output port. Because the RF sidebands are not resonant in the arms, noise on the RF sidebands is not attenuated by the coupled-cavity pole; instead they see a much lower finesse power recycling cavity and transmission is essentially flat in the band of interest. Once reaching the output port, however, the RF sidebands are strongly attenuated by the OMC.

At low frequency, the carrier contribution dominates; at higher frequency the residual RF sidebands dominate. This is depicted in figure 5.3.

Laser intensity noise creates a varying radiation pressure force in the arm cavities, which in turn causes displacement noise. To distinguish this effect from the inherent *quantum* radiation pressure noise[83], we refer to this as *technical* radiation pressure noise. For identical arm cavities, the effect would be entirely common mode. Differences in arm cavity finesse and (especially) the intentional differential detuning of the arm cavities produce a (potentially large[84]) coupling of technical radiation pressure noise to DARM.

Laser Frequency Noise

Frequency modulation of a field incident on a photodiode will produce no signal; in order for frequency modulation of the interferometer input field to couple to the DC readout photodiode signal, the frequency modulation must be converted to amplitude modulation

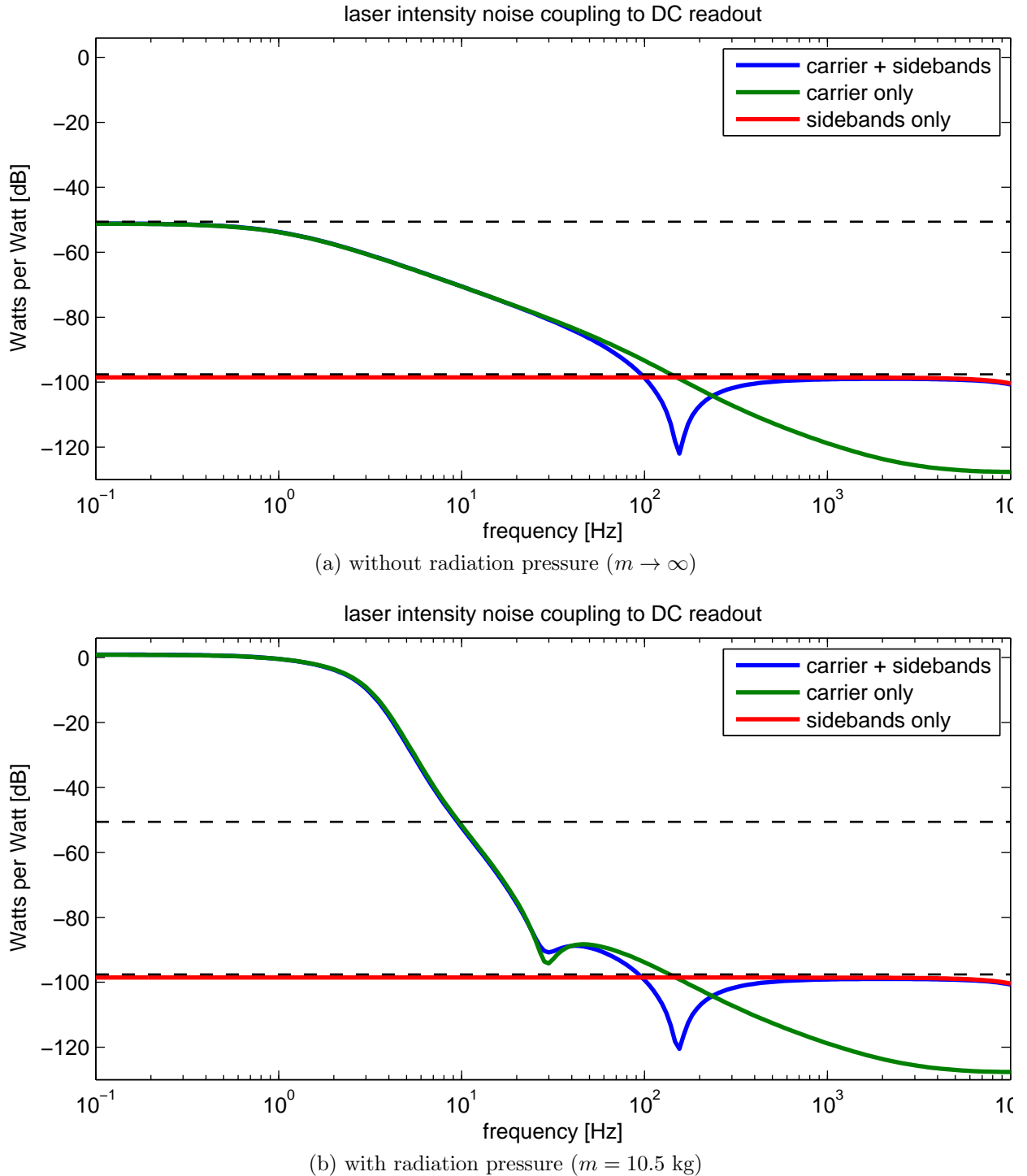


Figure 5.3: Direct contributions of amplitude modulation of the laser carrier and RF sidebands to DC readout, in the absence of radiation pressure. The carrier contribution is shaped by the coupled cavity pole. The RF contribution is due to residual off-resonance transmission through the OMC. Interference between the two coupling mechanisms creates a dip in the total coupling at the crossover frequency.

as the fields travel from the interferometer input to its output. FM to AM conversion is accomplished by rotating sidebands differentially or by rotating the parent carrier, which occurs due to asymmetries between the arms, including the intentional DARM offset (for DC readout), the intentional Michelson (Schnupp) asymmetry, and differences in finesse and losses in the two arms.

5.2.2 Oscillator Noises

Reduced coupling of noises from the RF oscillator is one of the motivations for implementing DC readout. Despite not relying on the RF sidebands directly, behavior of the RF oscillator is still able to enter into the DC readout signal through control loop cross-couplings, leakage of RF sideband power through the OMC, and amplitude modulation of the laser carrier induced via AM on the RF oscillator.

Oscillator AM

Amplitude fluctuations of the RF oscillator produce a fluctuating modulation depth; when the RF oscillator signal fluctuates upwards, more power is diverted from the carrier into the RF sidebands. The result is somewhat similar to laser AM, except that carrier AM and RF AM are anti-correlated instead of correlated.

Unlike laser AM, oscillator AM does not produce equal relative intensity noise (RIN) variations of the carrier and sidebands; this is simply because oscillator AM results in equal and opposite changes of power in the carrier and sideband rather than linear scalings of both. The sideband RIN per oscillator AM is given by

$$\frac{\text{SB RIN}}{\text{OSC AM}} = 2\Gamma_0 \frac{J'_1(\Gamma_0)}{J_1(\Gamma_0)} = \Gamma_0 \frac{J_0 - J_2}{J_1} \quad (5.5)$$

where Γ_0 is the nominal modulation depth, $J_n(z)$ is the n th Bessel function, and $J'_n(z) = (\partial/\partial z)J_n(z)$ is the derivative of the Bessel function.

Oscillator Phase Noise

Phase noise on the RF oscillator produces phase noise on the resulting RF sidebands, but does not affect the laser carrier. Its direct coupling to DC readout is therefore quite small; to couple to DC readout, the phase noise sidebands must be converted to AM through Michelson asymmetries, and then survive attenuation by the OMC.

5.3 Laser and Oscillator Noise Coupling Measurements

Laser and oscillator noise couplings were measured at both the H1 and L1 detectors¹, at a selection of DARM offsets. In this section I explain how the measurements were made and discuss the results.

5.3.1 Laser Noise Coupling Measurements

The LIGO laser source contains an intensity stabilization servo (ISS) which reduces the relative intensity noise (RIN) of the laser power before the laser enters the interferometer. Injecting an excitation into the error point of this servo impresses intensity noise onto the beam. The laser intensity noise coupling was measured by taking synchronous swept-sine transfer functions from a monitor photodiode just after the ISS and the DARM readout.

The laser frequency is stabilized to the mean length of the two arms (CARM) by a high-bandwidth analog servo, the common mode servo. Frequency modulation can be induced by injecting into the error point of this servo. Unlike with the ISS, there is no separate witness sensor to provide a direct measurement of the induced laser frequency modulation. Instead we must make a calibration of the common mode servo error point. The frequency noise coupling is to be calibrated in terms of Hz of frequency noise *before* the stabilizing action of the common mode servo, so we must account for the suppression of the loop. The calibration was done by porting the calibration of DARM to CARM, as follows:

1. Drive the position of one of the end test masses (ETMs) with a sinusoidal modulation at some probe frequency ($f = 7300$ Hz was used). In the absence of loops, this would produce equal DARM and CARM motion.
2. Measure the response in the DARM and CARM readouts. The CARM readout channel is REFL_I, which senses the mismatch between the laser carrier frequency and the CARM length.
3. Apply the DARM calibration. This includes compensation for the DARM control loop.
4. Compensate for the frequency noise suppression of the common mode loop by multiplying by $1 + G$ where G is the (complex) open loop gain of the common mode loop at the probe frequency.
5. Equate the calibrated DARM and loop-corrected CARM. This gives a calibration for CARM in meters at the probe frequency.
6. Multiply by $\delta\nu/\delta L = \nu/L = c/(\lambda L)$ to convert from meters to Hz.
7. Assume a model for the CARM to REFL_I transfer function to propagate the calibration to other frequencies. This transfer function is simply the coupled-cavity pole[47, eq. 3.5].

¹Measurements at Hanford were made by Nicolás Smith.

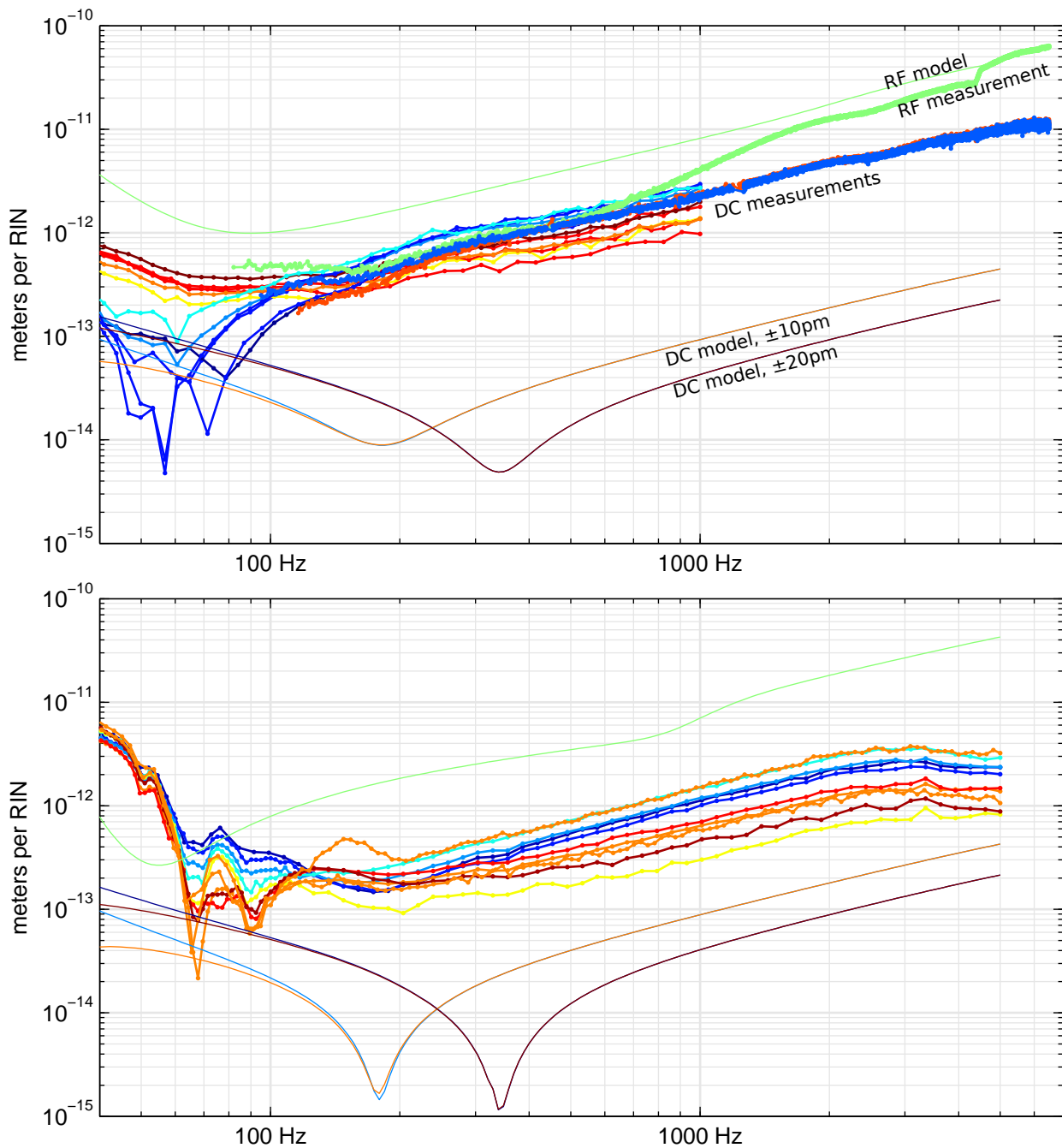


Figure 5.4: Laser intensity noise coupling to DARM. Solid lines are the results of a frequency-domain, plane-wave model; dotted lines are linear transfer function measurements. Color represents the DARM offset, with warm colors for positive offsets and cool colors for negative offsets. The upper plot is Livingston; the lower one is Hanford.

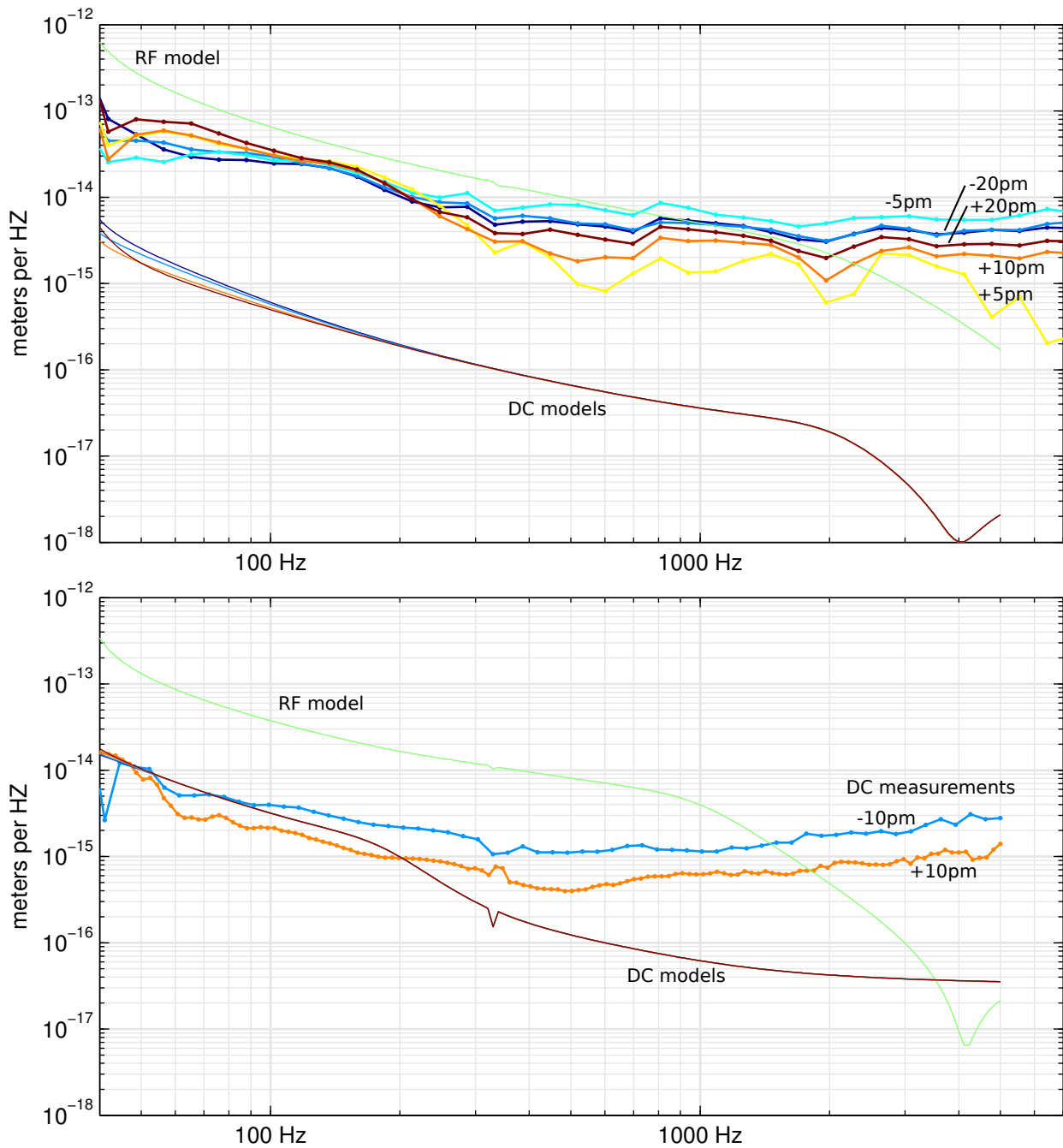


Figure 5.5: Laser frequency noise coupling to DARM

Discussion

In general, the measured laser noise couplings are much higher than the expectations from the Optickle models. The most likely explanation for this disagreement is that the Optickle models include only plane-wave effects; there is no modeling of higher order spatial modes, imperfect mode-matching, etc. The experience with the difficulty of designing an effective alignment servo for the OMC demonstrates the importance of these higher-order modes. Any deviation from perfect alignment of the interferometer itself or the beam into the OMC will lead to coupling of spurious higher-order modes from the power-recycling cavity into the OMC, leading to excess laser noise coupling. These modes are not resonant in the arms so would not experience filtering by the coupled-cavity pole, leading to a broadband increase in the coupling, as observed. To explore this hypothesis, more modeling should be conducted, using a tool which can model higher-order spatial modes.

5.3.2 Oscillator Noise Coupling Measurements

To measure oscillator noise couplings we temporarily switched the source of the 25 MHz oscillator from the Wenzel crystal oscillator to a general purpose (IFR 2023A) RF function generator, which accepts phase and amplitude modulation inputs. The measurements were made by connecting a spare DAC output to the modulation input of the IFR function generator and then taking synchronous swept-sine transfer functions from the modulation drive to the DC readout with the interferometer in its running configuration.

To calibrate the oscillator AM transfer function, we configured the interferometer optics (by misaligning unneeded mirrors) to send a fraction of the input light directly to the OMC and locked the OMC to one of the RF sidebands. Taking the transfer function in this configuration allowed a direct measurement of the AM imposed on the RF sidebands². To calibrate the oscillator PM transfer function, a curve with the same shape as the AM calibration was used, but with the DC value determined by the front panel setting of the phase modulation depth on the function generator. This was checked separately at a few individual frequencies by connecting the output of the function generator directly to an RF spectrum analyzer.

The measured oscillator AM coupling is shown in figure 5.6. The level of the coupling is well described by the Optickle model. Phase noise coupling measurements are given in figure 5.7, compared with measurements made in initial LIGO's RF readout[85]. We see a distinct (factor of 10) advantage of DC readout over RF readout.

5.4 Beam Jitter Noise

Beam jitter is perhaps the most important new noise source introduced in the DC readout system. The cavity converts motion of the incident beam into amplitude modulation, which

²Thank you to Robert Ward for suggesting the technique.

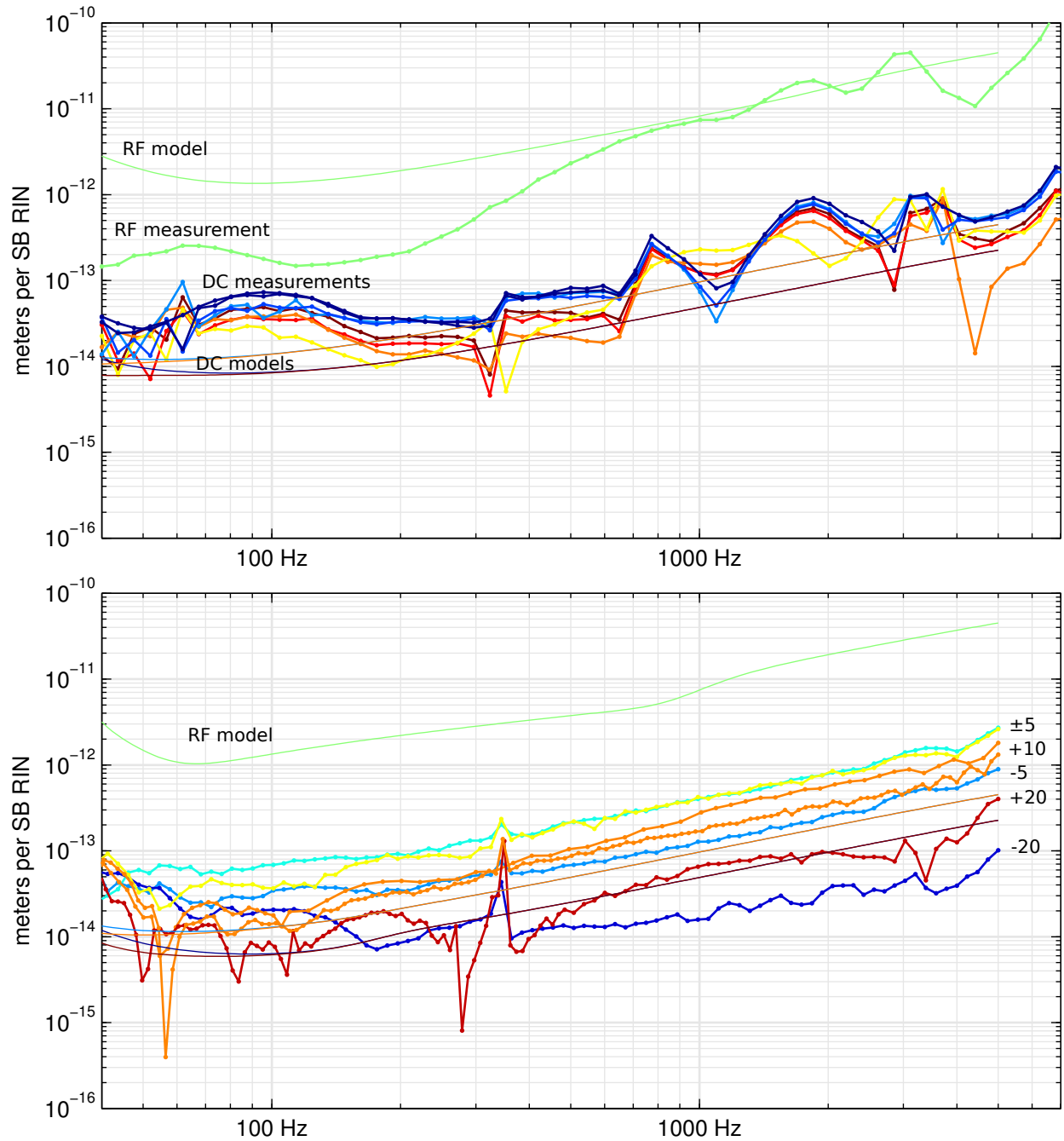


Figure 5.6: Oscillator amplitude noise coupling to DARM

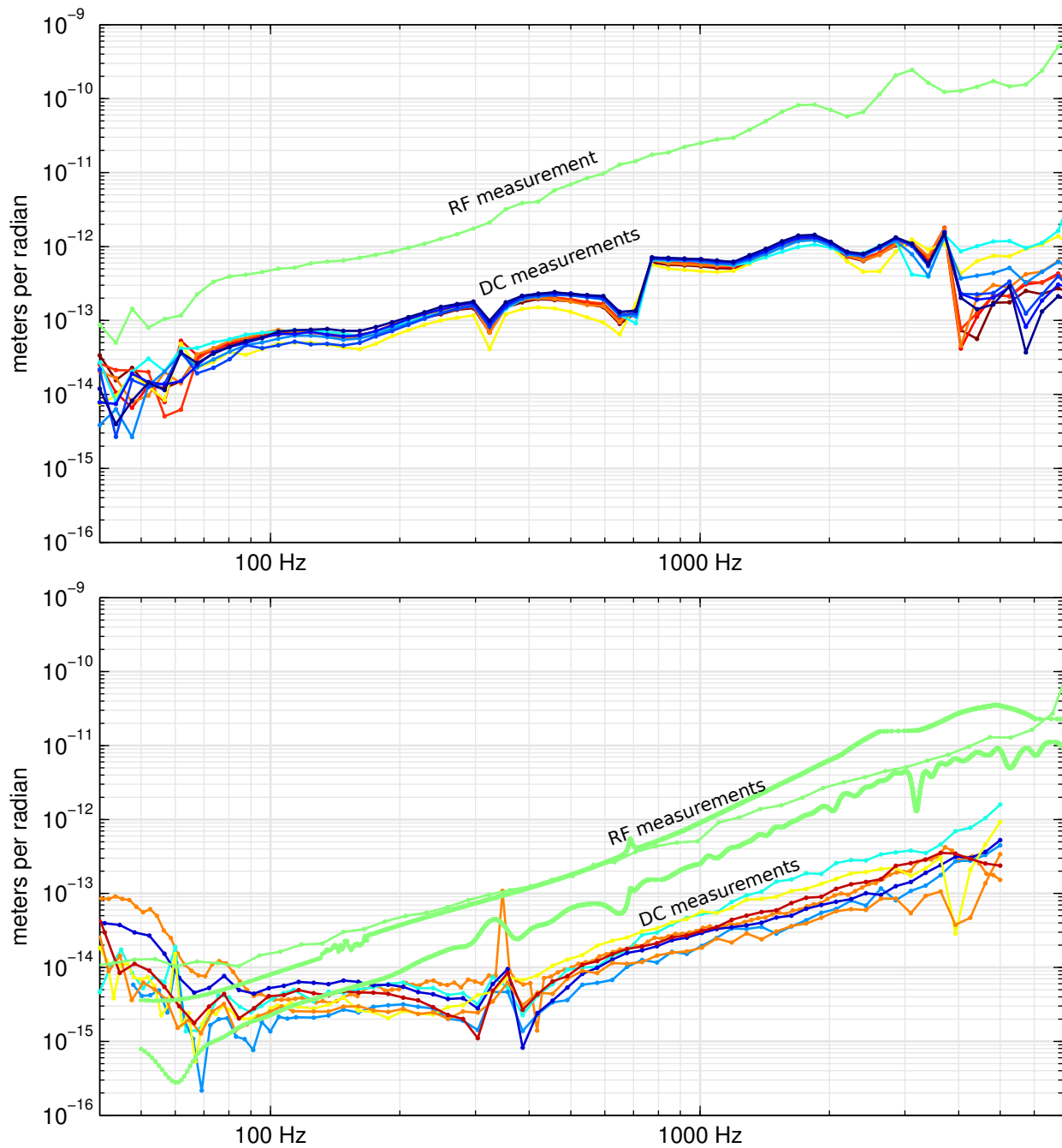


Figure 5.7: Oscillator phase noise coupling to DARM.

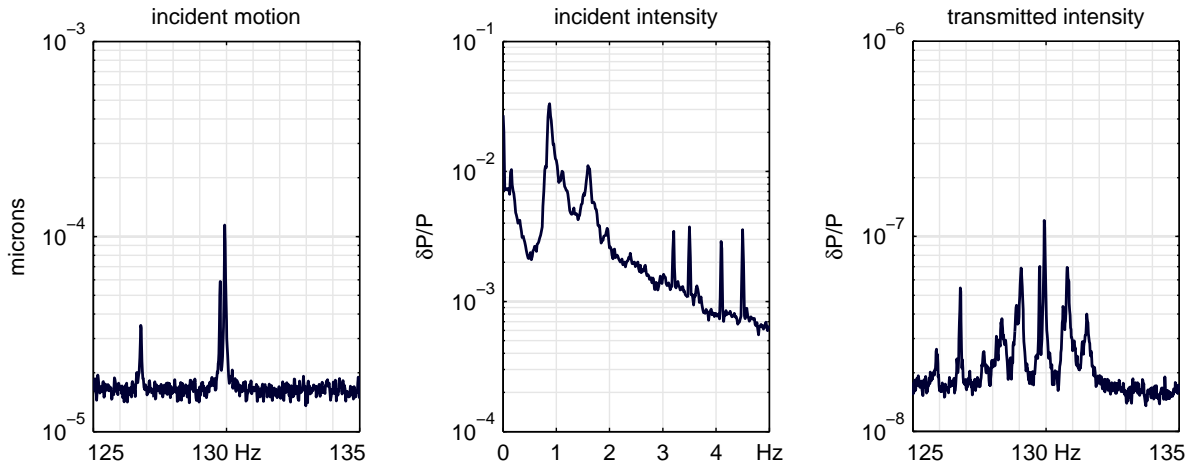


Figure 5.8: Example of linear and bilinear beam jitter coupling in the L1 OMC. Left: the light incident on the OMC shows motion at ~ 130 Hz (arbitrary units). Center: the incident light contains intensity modulations at ~ 0.87 and ~ 1.6 Hz (units: $\log_{10}(\delta P/P)$). Right: the light transmitted through the OMC contains intensity modulations at 130 Hz, 130 ± 0.87 Hz, and 130 ± 1.6 Hz (units: $\log_{10}(\delta P/P)$). (The sources of the incident beam motion and intensity fluctuations have not been identified.)

pollutes the readout. In the ideal case, this would be a quadratic effect, but the presence of spurious higher order modes introduces both linear and bilinear contributions.

We have several means of controlling the beam jitter contribution to the readout. In practice, we utilize all of them:

- *Remove mechanical resonances and increase isolation.* Several prominent beam-jitter peaks in the readout spectrum were removed by replacing a fixed steering mirror with a suspended one; and by adding blade-springs to the steering mirrors for additional vertical isolation.
- *Cancel the motion.* Motion at the 60 Hz power-line frequency is introduced via magnetic coupling to the magnets used to actuate on the suspended steering mirrors. We implemented a feed-forward correction using signals derived from a magnetometer located just outside the vacuum chamber.
- *Place steering optics where their coupling to beam jitter is small.* Beam propagation geometry can magnify the effects of optic motion to beam motion. For a given amount of optic jitter, the coupling to readout noise can be reduced by proper design of the mode-matching telescope. This constraint is at odds with the desire for maximum controllability of the input beam pointing. In practice the requirement is that sufficient actuation range be provided, and that the optics be well separated in Gouy phase to create a non-degenerate control matrix.

- *Reshape the beam.* Linear beamjitter coupling arises due to the presence of carrier-mode junk light in the HG01 mode incident on the mode cleaner. The transmission of this light through the OMC is linearly dependent on the position of the incident beam. By introducing offsets into the interferometer’s global angular sensing and control (ASC) system[86], this HG01 mode light can be cancelled out, nulling the linear sensitivity to beam motion. During Enhanced LIGO this was found to be a highly effective technique, but it was not automated.

An example of the observed beam jitter coupling is shown in Figure 5.8. A prominent spectral line at ~ 130 Hz appears in quadrant photodiode (QPD) signal, indicating relative motion in yaw between the incident beam and the OMC. This line also appears in the signal of the light transmitted through the OMC, indicating some linear coupling of beam jitter to transmission. The transmitted spectrum also contains sidebands around the 130 Hz line at separations of ± 0.875 Hz and ± 1.6 Hz which arise due to gain modulation.

Chapter 6

Conclusion

Over the last several decades, the state of the art of gravitational wave detection has advanced to the point where we are likely to discover gravitational waves with the detectors currently under construction.

Enhanced LIGO successfully demonstrated the viability of DC readout as a low noise interferometer readout technique. The DC readout system (including the output mode cleaner) in Enhanced LIGO alleviated the problems experienced with the heterodyne readout in initial LIGO, allowed us to increase the interferometer input power (increasing the detectors' sensitivity), and delivered the expected shot-noise-limited performance. The dual Enhanced LIGO goals of both increasing the detector sensitivity and gaining early experience with Advanced LIGO technologies were achieved.

During Enhanced LIGO we identified OMC alignment as a particularly important and unexpectedly subtle aspect of the OMC system, and identified and implemented an effective alignment system. We also gained valuable experience in the mitigation of beam jitter coupling.

Measurements of the couplings of laser and oscillator noises reveal that the couplings are generally improved over RF readout. Comparison of measured laser noise couplings with simple plane-wave models reveals that more sophisticated models (most likely incorporating higher-order spatial modes) are necessary to explain the measured couplings. The effect of spurious higher order modes will be mitigated in Advanced LIGO through the use of geometrically stable cavities, better optics, and improved thermal compensation; however, to the extent that the design relies on achieving the noise couplings predicted by a simple plane-wave model, I expect a long period of commissioning in order to achieve it.

Bibliography

- [1] Bernard F. Schutz. Gravitational waves on the back of an envelope. *American Journal of Physics*, 52(5):412–419, 1984.
- [2] Charles W. Misner, Kip S. Thorne, and John A. Wheeler. *Gravitation*. W. H. Freeman, first edition edition, September 1973.
- [3] Sean M. Carroll. Lecture notes on general relativity. December 1997.
- [4] Michele Maggiore. *Gravitational waves*, volume 1. Oxford Univ. Press, November 2008.
- [5] R. A. Hulse and J. H. Taylor. Discovery of a pulsar in a binary system. *Astrophys. J. Lett.*, 195:L51–L53, January 1975.
- [6] J. M. Weisberg and J. H. Taylor. The relativistic binary pulsar B1913+16: Thirty years of observations and analysis. In F. A. Rasio and I. H. Stairs, editors, *Binary Radio Pulsars*, volume 328 of *Astronomical Society of the Pacific Conference Series*, July 2005.
- [7] A. G. Lyne, M. Burgay, M. Kramer, A. Possenti, R. N. Manchester, F. Camilo, M. A. McLaughlin, D. R. Lorimer, N. D’Amico, B. C. Joshi, J. Reynolds, and P. C. C. Freire. A double-pulsar system: A rare laboratory for relativistic gravity and plasma physics. *Science*, 303(5661):1153–1157, February 2004.
- [8] M. Kramer, I. H. Stairs, R. N. Manchester, M. A. McLaughlin, A. G. Lyne, R. D. Ferdman, M. Burgay, D. R. Lorimer, A. Possenti, N. D’Amico, J. M. Sarkissian, G. B. Hobbs, J. E. Reynolds, P. C. C. Freire, and F. Camilo. Tests of general relativity from timing the double pulsar. *Science*, 314(5796):97–102, October 2006.
- [9] E. Mauceli, Z. K. Geng, W. O. Hamilton, W. W. Johnson, S. Merkowitz, A. Morse, B. Price, and N. Solomonson. The Allegro gravitational wave detector: Data acquisition and analysis. *Physical Review D*, 54:1264–1275, July 1996.
- [10] P. Astone, M. Bassan, P. Bonifazi, P. Carelli, M. G. Castellano, G. Cavallari, E. Coccia, C. Cosmelli, V. Fafone, S. Frasca, E. Majorana, I. Modena, G. V. Pallottino, G. Pizzella, P. Rapagnani, F. Ricci, and M. Visco. Long-term operation of the Rome “Explorer” cryogenic gravitational wave detector. *Physical Review D*, 47:362–375, January 1993.

- [11] Kip S. Thorne. Gravitational-wave research: Current status and future prospects. *Reviews of Modern Physics*, 52(2):285–297, April 1980.
- [12] James L. Levine. Early gravity-wave detection experiments, 1960-1975. *Physics in Perspective (PIP)*, 6(1):42–75, April 2004.
- [13] B. Abbott, *et al.* First cross-correlation analysis of interferometric and resonant-bar gravitational-wave data for stochastic backgrounds. *Physical Review D*, 76:022001+, July 2007.
- [14] Rainer Weiss. Electromagnetically coupled broadband gravitational antenna. *Quarterly Progress Reports of the Research Laboratory for Electronics*, 105:54–76, April 1972.
- [15] Robert L. Forward. Wideband laser-interferometer gravitational-radiation experiment. *Physical Review D*, 17(2):379–390, January 1978.
- [16] B. P. Abbott, *et al.* LIGO: the Laser Interferometer Gravitational-wave Observatory. *Reports on Progress in Physics*, 72(7):076901+, July 2009.
- [17] F. Acernese, *et al.* The Virgo 3 km interferometer for gravitational wave detection. *Journal of Optics A: Pure and Applied Optics*, 10(6):064009+, June 2008.
- [18] H. Grote. The status of GEO 600. *Classical and Quantum Gravity*, 25(11):114043+, June 2008.
- [19] G. Hobbs, *et al.* The international pulsar timing array project: using pulsars as a gravitational wave detector. *Classical and Quantum Gravity*, 27, November 2009.
- [20] J. P. Filippini, *et al.* SPIDER: a balloon-borne CMB polarimeter for large angular scales. June 2011.
- [21] Jacob P. Slutsky. *Quantifying the Impact of Data Quality on Searches for Gravitational Waves From Binary Coalescing Systems with LIGO*. PhD thesis, Louisiana State University, June 2010.
- [22] J. Slutsky, L. Blackburn, D. A. Brown, L. Cadonati, J. Cain, M. Cavaglià, S. Chatterji, N. Christensen, M. Coughlin, S. Desai, G. González, T. Isogai, E. Katsavounidis, B. Rankins, T. Reed, K. Riles, P. Shawhan, J. R. Smith, N. Zotov, and J. Zweizig. Methods for reducing false alarms in searches for compact binary coalescences in LIGO data. *Classical and Quantum Gravity*, 27(16):165023+, August 2010.
- [23] B. Knispel, *et al.* Pulsar discovery by global volunteer computing. *Science*, 329(5997):1305, September 2010.
- [24] Bruce Allen and Joseph D. Romano. Detecting a stochastic background of gravitational radiation: Signal processing strategies and sensitivities. *Physical Review D*, 59(10):102001+, March 1999.

- [25] Albert Lazzarini and Rainer Weiss. LIGO science requirements document. Technical Report E950018, LIGO Laboratory, March 1996.
- [26] Stefan Ballmer. *LIGO interferometer operating at design sensitivity with application to gravitational radiometry*. PhD thesis, Massachusetts Institute of Technology, June 2006.
- [27] Alex Abramovici, William E. Althouse, Ronald W. P. Drever, Yekta Gursel, Seiji Kawamura, Frederick J. Raab, David Shoemaker, Lisa Sievers, Robert E. Spero, Kip S. Thorne, Rochus E. Vogt, Rainer Weiss, Stanley E. Whitcomb, and Michael E. Zucker. LIGO: The laser interferometer gravitational-wave observatory. *Science*, 256(5055):325–333, April 1992.
- [28] Rana Adhikari, Peter Fritschel, and Sam Waldman. Enhanced LIGO. Technical Report T060156-01-I, LIGO Laboratory, July 2006.
- [29] Peter Fritschel, Rana Adhikari, and Rai Weiss. Enhancements to the LIGO S5 detectors. Technical Report T050252-00-I, LIGO Laboratory, November 2005.
- [30] Josh R. Smith for the LIGO Scientific Collaboration. The path to the enhanced and advanced LIGO gravitational-wave detectors. *Classical and Quantum Gravity*, 26(11):114013+, June 2009.
- [31] J. Abadie, *et al.* Search for gravitational waves from binary black hole inspiral, merger, and ringdown. *Physical Review D*, 83:122005+, June 2011.
- [32] J. Abadie, *et al.* Search for gravitational waves from compact binary coalescence in LIGO and virgo data from s5 and VSR1. *Physical Review D*, 82(10):102001+, November 2010.
- [33] B. P. Abbott, *et al.* Search for gravitational-wave bursts in the first year of the fifth LIGO science run. *Physical Review D (Particles, Fields, Gravitation, and Cosmology)*, 80(10):102001+, 2009.
- [34] J. Abadie, *et al.* All-sky search for gravitational-wave bursts in the first joint LIGO-GEO-virgo run. *Physical Review D*, 81(10):102001+, May 2010.
- [35] B. P. Abbott, *et al.* Searches for gravitational waves from known pulsars with science run 5 LIGO data. *The Astrophysical Journal*, 713(1):671–685, April 2010.
- [36] J. Abadie, *et al.* All-sky search for periodic gravitational waves in the full s5 LIGO data. October 2011.
- [37] B. Abbott, *et al.* Implications for the origin of GRB 070201 from LIGO observations. *The Astrophysical Journal*, 681:1419–1430, July 2008.
- [38] J. Abadie, *et al.* First search for gravitational waves from the youngest known neutron star. *The Astrophysical Journal*, 722(2):1504+, October 2010.

- [39] B. P. Abbott, R. Abbott, F. Acernese, R. Adhikari, P. Ajith, B. Allen, G. Allen, M. Alshourbagy, R. S. Amin, S. B. Anderson, W. G. Anderson, F. Antonucci, S. Aoudia, M. A. Arain, M. Araya, H. Armandula, P. Armor, K. G. Arun, Y. Aso, S. Aston, P. Astone, P. Aufmuth, and C. Aulbert. An upper limit on the stochastic gravitational-wave background of cosmological origin. *Nature*, 460(7258):990–994, August 2009.
- [40] Maik Frede, Bastian Schulz, Ralf Wilhelm, Patrick Kwee, Frank Seifert, Benno Willke, and Dietmar Kracht. Fundamental mode, single-frequency laser amplifier for gravitational wave detectors. *Opt. Express*, 15(2):459–465, January 2007.
- [41] Katherine Dooley, Muzammil Arain, David Feldbaum, Valery Frolov, Matthew Heintze, Daniel Hoak, Em Khazanov, Antonio Lucianetti, Rodica Martin, Guido Müller, Oleg Palashov, Volker Quetschke, David H. Reitze, Rick Savage, David Tanner, Luke Williams, and Wan Wu. Characterization of thermal effects in the enhanced LIGO input optics. 2011.
- [42] Volker Quetschke. Electro-Optic modulators and modulation for enhanced LIGO and beyond. In *Coherent Optical Technologies and Applications*, pages CMC1+. Optical Society of America, July 2008.
- [43] Rupal Amin. *Modeling thermal phenomena and searching for new thermally induced monitor signals in large scale gravitational wave detectors*. PhD thesis, Louisiana State University, May 2010.
- [44] Jeffrey S. Kissel. *Calibrating and Improving the Sensitivity of the LIGO Detectors*. PhD thesis, Louisiana State University, September 2010.
- [45] J. Sidles and D. Sigg. Optical torques in suspended FabryPerot interferometers. *Physics Letters A*, 354(3):167–172, May 2006.
- [46] Kate Dooley, Lisa Barsotti, and Matt Evans. Angular sensing and control of the enhanced LIGO interferometers. in press.
- [47] Rana Adhikari. *Sensitivity and noise analysis of 4 km laser interferometric gravitational wave antennae*. PhD thesis, Massachusetts Institute of Technology, July 2006.
- [48] Robert L. Ward. *Length Sensing and Control of an Advanced Prototype Interferometric Gravitational Wave Detector*. PhD thesis, California Institute of Technology, Pasadena, CA, February 2010.
- [49] S. Hild, H. Grote, J. Degallaix, S. Chelkowski, K. Danzmann, A. Freise, M. Hewitson, J. Hough, H. Luck, M. Prijatelj, K. A. Strain, J. R. Smith, and B. Willke. DC-readout of a signal-recycled gravitational wave detector. *Classical and Quantum Gravity*, 26(5):055012+, March 2009.

- [50] J. Degallaix, H. Grote, M. Prijatelj, M. Hewitson, S. Hild, C. Affeldt, A. Freise, J. Leong, H. Lück, K. A. Strain, H. Wittel, B. Willke, and K. Danzmann. Commissioning of the tuned DC readout at GEO 600. *Journal of Physics: Conference Series*, 228(1):012013+, May 2010.
- [51] M. Abernathy, F. Acernese, P. Ajith, B. Allen, P. Amaro-Seoane, N. Andersson, S. Aoudia, P. Astone, B. Krishnan, L. Barack, F. Barone, B. Barr, and M. Barsuglia. Einstein telescope design study. Technical Report ET-0106A-10, Einstein Telescope Science Team, May 2011.
- [52] Karsten Danzmann and Albrecht Rüdiger. LISA technologyconcept, status, prospects. *Classical and Quantum Gravity*, 20(10):S1–S9, May 2003.
- [53] B. Lange. The Drag-Free satellite. *AIAA Journal*, 2:1590–1606, September 1964.
- [54] Peter R. Saulson. *Fundamentals of Interferometric Gravitational Wave Detectors*. World Scientific Publishing Company, 1994.
- [55] Daniel Sigg and others. Frequency response of the LIGO interferometer. Technical Report T970084-00, LIGO Laboratory, February 1997.
- [56] Malik Rakhmanov. *Dynamics of Laser Interferometric Gravitational Wave Detectors*. PhD thesis, California Institute of Technology, May 2000.
- [57] Peter Fritschel, Rolf Bork, Gabriela González, Nergis Mavalvala, Dale Ouimette, Haisheng Rong, Daniel Sigg, and Michael Zucker. Readout and control of a power-recycled interferometric gravitational-wave antenna. *Appl. Opt.*, 40(28):4988–4998, October 2001.
- [58] Martin W. Regehr. *Signal Extraction and Control for an Interferometric Gravitational Wave Detector*. PhD thesis, California Institute of Technology, August 1994.
- [59] Eric D. Black and Ryan N. Gutenkunst. An introduction to signal extraction in interferometric gravitational wave detectors. *American Journal of Physics*, 71(4):365–378, 2003.
- [60] R. W. P. Drever, J. L. Hall, F. V. Kowalski, J. Hough, G. M. Ford, A. J. Munley, and H. Ward. Laser phase and frequency stabilization using an optical resonator. *Applied Physics B: Lasers and Optics*, 31(2):97–105, June 1983.
- [61] Eric D. Black. An introduction to Pound-Drever-Hall laser frequency stabilization. *American Journal of Physics*, 69(1):79–87, January 2001.
- [62] Peter R. Saulson. Thermal noise in mechanical experiments. *Physical Review D*, 42(8):2437–2445, October 1990.

- [63] Gabriela I. González and Peter R. Saulson. Brownian motion of a mass suspended by an anelastic wire. *The Journal of the Acoustical Society of America*, 96(1):207–212, 1994.
- [64] T. M. Niebauer, R. Schilling, K. Danzmann, A. Rüdiger, and W. Winkler. Nonstationary shot noise and its effect on the sensitivity of interferometers. *Physical Review A*, 43(9):5022–5029, May 1991.
- [65] Kirk McKenzie, Malcolm B. Gray, Ping K. Lam, and David E. McClelland. Technical limitations to homodyne detection at audio frequencies. *Appl. Opt.*, 46(17):3389–3395, June 2007.
- [66] Peter Fritschel. Shot noise and optical gain of the H1 interferometer. Technical Report T030004-00-D, LIGO Laboratory, January 2003.
- [67] J. Gea-Banacloche and G. Leuchs. Squeezed states for interferometric gravitational-wave detectors. *Journal of Modern Optics*, 34(6):793–811, 1987.
- [68] Simon Chelkowski, Henning Vahlbruch, Karsten Danzmann, and Roman Schnabel. Coherent control of broadband vacuum squeezing. *Physical Review A*, 75(4):043814+, April 2007.
- [69] J. Abadie, *et al.* A gravitational wave observatory operating beyond the quantum shot-noise limit. *Nature Physics*, advance online publication, September 2011.
- [70] Daniel Sigg, Nergis Mavalvala, David McClelland, Ping K. Lam, Roman Schnabel, Henning Vahlbruch, and Stan Whitcomb. Proposal for a squeezed H1 interferometer. Technical Report T070265-D, LIGO Laboratory, October 2008.
- [71] M. Evans, N. Mavalvala, P. Fritschel, R. Bork, B. Bhawal, R. Gustafson, W. Kells, M. Landry, D. Sigg, R. Weiss, S. Whitcomb, and H. Yamamoto. Lock acquisition of a gravitational-wave interferometer. *Opt. Lett.*, 27(8):598–600, April 2002.
- [72] Andri M. Gretarsson, Erika D’Ambrosio, Valery Frolov, Brian O'Reilly, and Peter K. Fritschel. Effects of mode degeneracy in the LIGO livingston observatory recycling cavity. *J. Opt. Soc. Am. B*, 24(11):2821–2828, November 2007.
- [73] Simon Ressel, Martin Gohlke, Dominik Rauen, Thilo Schuldt, Wolfgang Kronast, Ulrich Mescheder, Ulrich Johann, Dennis Weise, and Claus Braxmaier. Ultrastable assembly and integration technology for ground- and space-based optical systems. *Appl. Opt.*, 49(22):4296–4303, August 2010.
- [74] E. J. Elliffe, J. Bogenstahl, A. Deshpande, J. Hough, C. Killow, S. Reid, D. Robertson, S. Rowan, H. Ward, and G. Cagnoli. Hydroxide-catalysis bonding for stable optical systems for space. *Classical and Quantum Gravity*, 22(10):S257–S267, May 2005.

- [75] L. d'Arcio, J. Bogenstahl, M. Dehne, C. Diekmann, E. D. Fitzsimons, R. Fleddermann, E. Granova, G. Heinzel, H. Hogenhuis, C. J. Killow, M. Perreur-Lloyd, J. Pijnenburg, D. I. Robertson, A. Shoda, A. Sohmer, A. Taylor, M. Tröbs, G. Wanner, H. Ward, and D. Weise. Optical bench development for LISA. In *International Conference on Space Optics*. European Space Agency, October 2010.
- [76] Norna A. Robertson, D. Coyne, C. Echols, P. Fritschel, V. Mandic, J. Romie, C. Torrie, and S. Waldman. Conceptual design of a double pendulum for the output modecleaner. Technical Report T060257-03-R, LIGO Laboratory, December 2006.
- [77] Norna A. Robertson, Mark Barton, Derek Bridges, Jay Heefner, Mike Meyer, Janeen Romie, and Calum Torrie. OMC suspension final design document. Technical Report T0900060-v1, LIGO Laboratory, March 2009.
- [78] Rolf Bork and Jay Heefner. ELIGO OMC front end controls design description. Technical Report T0900329, LIGO Laboratory, July 2009.
- [79] R. Bork and M. Aronsson. AdvLigo CDS real-time code generator (RCG) application developer's guide. Technical report, LIGO Laboratory, October 2009.
- [80] Nicolás Smith-Lefebvre, Stefan Ballmer, Matt Evans, Sam Waldman, Keita Kawabe, Valery Frolov, and Nergis Mavalvala. Optimal alignment sensing of a mode cleaner cavity used for optical readout. *Optics Letters*, in press.
- [81] Jamie Rollins, Nicolás Smith, and Sam Waldman. H1 OMC DC PDs. Technical Report T0900420, LIGO Laboratory, September 2009.
- [82] Matthew Evans. Optickle. Technical Report T070260-00, LIGO Laboratory, October 2007.
- [83] Carlton M. Caves. Quantum-Mechanical Radiation-Pressure fluctuations in an interferometer. *Physical Review Letters*, 45(2):75–79, July 1980.
- [84] W. Chaibi and François Bondu. Optomechanical issues in the gravitational wave detector advanced VIRGO. *Comptes rendus de l'Académie des Sciences*, in press.
- [85] Nicolás Smith. Oscillator phase noise coupling. Technical Report T050138, LIGO Laboratory, August 2005.
- [86] L. Barsotti, M. Evans, and P. Fritschel. Alignment sensing and control in advanced LIGO. *Classical and Quantum Gravity*, 27(8):084026+, April 2010.
- [87] Brian J. Meers. Recycling in laser-interferometric gravitational-wave detectors. *Physical Review D*, 38(8):2317–2326, October 1988.
- [88] Charles Fabry. Théorie de la visibilité et de l'orientation des franges d'interférence. *Journal de Physique Théorique et Appliquée*, 1(1):313–332, 1892.

- [89] Charles Fabry and Alfred Perot. On a new form of interferometer. *Astrophys. J.*, 13:265+, May 1901.
- [90] A. E. Siegman. *Lasers*. University Science Books, October 1990.
- [91] A. Gardner Fox and Tingye Li. Resonant modes in a maser interferometer. *Bell System Technical Journal*, 40(2):453–488, March 1961.
- [92] Hermann A. Haus. *Waves and Fields in Optoelectronics*. Prentice-Hall series in solid state physical electronics. Prentice-Hall, September 1983.
- [93] Benjamin S. Sheard, Malcolm B. Gray, Conor M. Mow Lowry, David E. McClelland, and Stanley E. Whitcomb. Observation and characterization of an optical spring. *Physical Review A*, 69(5):051801+, May 2004.
- [94] Thomas R. Corbitt. *Quantum Noise and Radiation Pressure Effects in High Power Optical Interferometers*. PhD thesis, Massachusetts Institute of Technology, August 2008.
- [95] J. Abadie, B. P. Abbott, R. Abbott, M. Abernathy, C. Adams, R. Adhikari, P. Ajith, B. Allen, G. Allen, and E. Amador Ceron. Calibration of the LIGO gravitational wave detectors in the fifth science run. *Nuclear Instruments and Methods in Physics Research Section A: Accelerators, Spectrometers, Detectors and Associated Equipment*, 624(1):223–240, December 2010.
- [96] Evan A. Goetz. *Gravitational Wave Studies: Detector Calibration and an All-Sky Search for Spinning Neutron Stars in Binary Systems*. PhD thesis, University of Michigan, Ann Arbor, Michigan, August 2010.
- [97] H. Kogelnik and T. Li. Laser beams and resonators. *Appl. Opt.*, 5(10):1550–1567, October 1966.
- [98] Albrecht Rüdiger. Phase relationships at a symmetric beamsplitter. December 1998.

Appendix A

Table of Abbreviations

abbrev.	meaning
40m	Caltech 40-meter prototype interferometer
AF	audio frequency
AM	amplitude modulation
AS	antisymmetric (output) port
ASC	angular sensing and control
BS	beamsplitter
CARM	common arm length
CM	common mode
DARM	differential arm length; the gravitational wave readout channel
DC	direct current (i.e. zero frequency)
ETM	end test mass
FSR	free spectral range
FWHM	full width, half max
GW	gravitational wave
IFO	interferometer
ISC	interferometer sensing and control
ISS	intensity stabilization servo
ITMX	input test mass, X arm
LHO	LIGO Hanford Observatory
LIGO	Laser Interferometer Gravitational-wave Observatory
LISA	Laser Interferometer Space Antenna
LISO	program for linear simulation and optimization of analog electronic circuits
LLO	LIGO Livingston Observatory
LSC	length sensing and control
LSC	LIGO Scientific Collaboration
LSU	Louisiana State University
MC	mode cleaner
MICH	Michelson interferometer
MIT	Massachusetts Institute of Technology

OMC	output mode cleaner
PD	photodiode
PM	phase modulation
PRC	power recycling cavity
PSL	pre-stabilized laser
PZT	lead zirconate titanate; piezoelectric transducer
RF	radio frequency
RIN	relative intensity noise ($\delta P/P$)
RMS	root mean square (i.e. standard deviation)
SNR	signal-to-noise ratio
SQL	standard quantum limit
TCS	thermal compensation system
ULE	Corning Ultra Low Expansion glass

Appendix B

Determination of LIGO Cavity Lengths and Mirror Reflectivities

The lengths of cavities and reflectivities of mirrors in LIGO are all driven by a small number of design decisions. This section is intended to be a brief and friendly derivation of some of these values. Definitive references are [55] or [57]; A more general reference is [16].

As in the preceding sections, I simply use the plane-wave approximation for fields inside cavities. This introduces certain inaccuracies, as, for example, I ignore Gouy phase. Nonetheless, comparison of the values derived here to the actual LIGO design shows good agreement.

It is useful to draw a distinction between macroscopic and microscopic lengths. Macroscopic lengths are those derived here and used in detector engineering, with magnitudes ranging from kilometers down to centimeters or millimeters. Microscopic lengths are those on the order of the wavelength of light and smaller, sometimes *much* smaller. Microscopic lengths are never determined explicitly; instead they are controlled by servo systems to hold cavities on resonance. When we say that a cavity is a certain macroscopic length, we retain the freedom to adjust the microscopic length to attain resonance.

B.1 Arm Length

How big a detector can you build? The physical length of the detector's arms sets the conversion between displacement and strain. Simply making the arms longer will make any fixed displacement noises into smaller strain noises—so we want the arms as long as possible. How big one can build is usually a result of geography, money, and politics. LIGO got

$$L_+ = 4000 \text{ meters} \tag{B.1}$$

where $L_+ = (1/2)(L_x + L_y)$ is the average arm length.

The cavity length determines the free-spectral-range:

$$\nu_0 \equiv \frac{c}{2L_+} \approx 37.5 \text{ kHz} \quad (\text{B.2})$$

B.2 Bandwidth

In the Fabry-Perot Michelson interferometer design, there is a trade-off between the detector's sensitivity and its bandwidth.¹ As the storage time in the arm becomes longer and longer (either by making the arm longer, or by increasing its finesse), the sensitivity to gravitational waves increases commensurately. However, sensitivity to waves whose period is shorter than the storage time of the arm is attenuated. Thus there is a trade-off between sensitivity and bandwidth. One must choose a bandwidth. LIGO chooses:

$$f_c = 90 \text{ Hz} \quad (\text{B.3})$$

Together, the free spectral range and the arm cavity pole determine the cavity finesse:

$$\mathcal{F} = \frac{f_{FSR}}{2f_c} \approx 210 \quad (\text{B.4})$$

B.3 Test Mass Reflectivities

Knowing our desired finesse allows us to choose the mirror reflectivities. The finesse is uniquely determined by the fraction of circulating power that remains in the cavity after each roundtrip, which is given by a product of the mirror reflectivities and $r_L = \sqrt{1 - L}$ where L represents losses due to scattering, absorption, etc.

$$\mathcal{F} \approx -\frac{\pi}{\log r_1 r_2 r_L} \quad (\text{B.5})$$

This relation fixes the product $r_1 r_2$, leaving the ratio r_1/r_2 as a free parameter. This ratio determines the coupling of the cavity, from maximally over-coupled ($r_2 \rightarrow 1$), to critically coupled ($r_1 = r_2$), or to cavity at all ($r_1 \rightarrow 1$). How do we choose the coupling? Intuitively, we want to couple as much light as possible into the cavity. In one point of view, this is so there is as much light as possible present inside the cavity to be phase modulated by the gravitational wave. The power gain inside the cavity is given by

$$g^2 = \frac{1 - r_1^2}{(1 - r_1 r_2)^2}$$

¹Advanced LIGO will include an additional mirror, a *signal recycling mirror*[87] at the output of the interferometer, forming an additional resonant cavity at the anti-symmetric port. This cavity allows the interferometer DC sensitivity to be increased without decreasing its bandwidth.

To maximize this, we want r_1 as small as possible, so we make the ETM as reflective as possible. It turns out that maximal over-coupling is the way to go. The best super-polished mirrors we could buy have transmissivities of 10 ppm, which gives

$$r_2 = \sqrt{1 - 10 \times 10^{-6}} \approx 0.999995 \quad (\text{B.6})$$

Solving equation 1, we find:

$$r_1 \approx 0.985 \quad (\text{B.7})$$

B.4 Power Recycling and the Recycling Mirror

With the Fabry-Perot Michelson interferometer tuned to the dark fringe, all of the light not lost in the arm cavities is reflected back towards the laser source. To send this light back into the interferometer, we add a power recycling mirror, which forms a resonant cavity with the FP Michelson. We choose the reflectivity of the recycling mirror to make the cavity critically-coupled for the carrier.

With the Michelson on a dark fringe, the Michelson reflectivity is given by the cavity reflectivity on resonance:

$$r_c = \frac{r_1 - r_2 r_L}{1 - r_1 r_2 r_L} \quad (\text{B.8})$$

where r_L represents losses in the arm cavity.

We choose:

$$r_{RM}^2 = 0.97 \quad (\text{B.9})$$

The recycling mirror transmission is chosen to match the losses of the rest of the system.

B.5 Power Recycling Cavity Length

We need to have some radio-frequency sidebands in order to implement the heterodyne scheme that is used to control most of the interferometer. Its frequency is chosen to be several tens of MHz, and to be approximately² anti-resonant in the arm cavities. We choose:

$$f_{RF} \approx 24.5 \text{ MHz}$$

The RF sidebands must fit in the power recycling cavity. The resonant conditions for the carrier and for the sideband in the PRC are slightly different. Because the carrier is resonant in the (strongly over-coupled) arm cavities, it sees a sign flip in reflection from the arms that is not seen by the sideband. The carrier is actually *anti*-resonant in the PRC until the arms come into resonance and this extra sign flip comes into play. The minimum

²If the sideband were perfectly anti-resonant in the arms, then the first harmonic would be resonant, which is undesirable.

length of the PRC that satisfies this requirement occurs when the carrier accumulates π radians more phase than the lower sideband over a round-trip traversal of the cavity. The upper sideband, in turn, acquires π radians more than the carrier, putting it 2π above the lower sideband, making them simultaneously resonant. The carrier gets its final π radians on reflection from the over-coupled arm.

Instead of relying on intuitive arguments, we can write down equations for the conditions of resonance:

$$\exp \{i(2l/c)\omega_0\} = -1 \quad (\text{B.10})$$

$$\exp \{i(2l/c)(\omega_0 \pm \omega_{rf})\} = +1 \quad (\text{B.11})$$

Solving these³, we find a nice relationship between the cavity length and the RF wavelength $\lambda_{rf} = c/f_{rf} \approx 12$ meters:

$$2l_+ = \lambda_{rf} \left(m + \frac{1}{2} \right)$$

where m is any integer. The length corresponding to $m = 0$ is inconveniently short, so we choose $m = 1$, giving a power recycling cavity length of:

$$l_+ = 9.18 \text{ meters}$$

The PRC length is set to allow simultaneous resonance of the carrier and sidebands in the power recycling cavity.

B.6 The Schnupp Asymmetry

Now that we have the RF sidebands resonant in the recycling cavity, we need to get them to the output port.

A Michelson with identical arms has no frequency selectivity; in principle even white light would experience bright and dark fringes. Introducing an offset breaks this degeneracy, as the offset allows higher frequency waves to accumulate more phase than slower frequencies. Introducing a macroscopic difference in the arm lengths separates the carrier fringes from the sideband fringes. In the longer arm, now, the lower sideband accumulates less phase than the carrier, and the upper sideband accumulates a bit more. When the beams from the two arms recombine, the phase difference now depends on the frequency. With such an asymmetry, the Michelson can be simultaneously reflective of the carrier and partially transmissive of the sidebands.

How much sideband transmission do we need? The Michelson is acting as the second mirror in a resonant cavity. If we want to have perfect transmission of the sideband to the output port, then the power recycling cavity must be critically coupled for the sideband.

³Remember the multivaluedness of the logarithm, i.e. $\log 1 = i2\pi n$ for all integers n .

This occurs when the Michelson transmission of the sideband is equal to the transmissivity of the RM. This scheme for getting the sideband to the “dark” port is attributed to Lisa Schnupp, and the offset is called the Schnupp asymmetry.

The Michelson reflectivity for the sideband is:

$$r_M = \cos \frac{2\pi f_{rf} l_-}{c} \quad (\text{B.12})$$

(The fringe of the lower sideband lags that of the carrier, and the upper sideband leads the carrier. But because the carrier itself is on a dark fringe, the transmission of both the upper and lower sidebands turns out to be the same.)

Solving $r_M^2 = 0.97$ in order to match the RM, we find a Schnupp asymmetry of

$$l_- = 34 \text{ cm} \quad (\text{B.13})$$

The Schnupp asymmetry sets the coupling of the RF sidebands to the antisymmetric port.

Appendix C

Fabry-Perot Cavities

In this appendix I derive the basic properties of Fabry-Perot cavities [88, 89] in the plane wave approximation. Excellent references with further detail include [90], [91], and the general optics reference [92].

C.1 Fabry-Perot Field Equations

We begin by writing down the relationships between the fields at each interface. For simplicity, we treat each mirror as a single (thin) interface. Let r_1 and t_1 be the amplitude reflectivity and transmissivity for the input mirror, and r_2 and t_2 describe the output mirror. I use the phase convention where transmission through a mirror conveys 90° of phase,

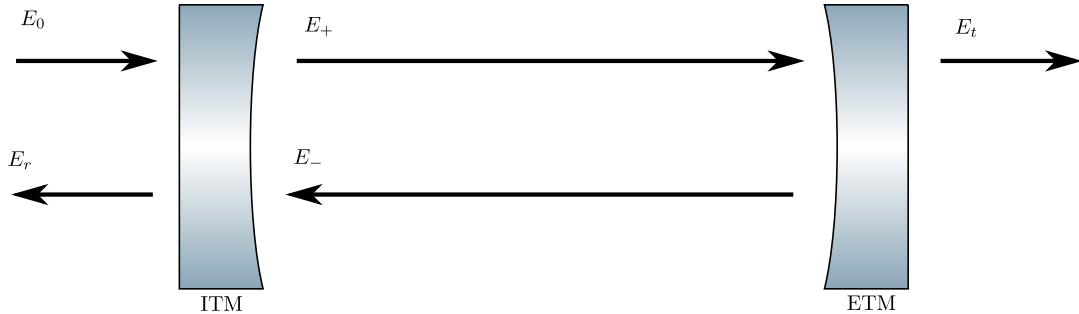


Figure C.1: Fabry-Perot cavity. When used as an arm cavity, the two mirrors are known as the input (ITM) and end (ETM) test masses. Here E_0 indicates the amplitude of the incident electric field, E_r the reflected field, E_+ the forward-going intra-cavity field, etc.

i.e. a factor of i in the amplitude:

$$E_+ = it_1 E_0 + r_1 E_- \quad (\text{C.1})$$

$$E_- = r_2 e^{i2\phi} E_+ \quad (\text{C.2})$$

$$E_t = it_2 e^{i\phi} E_+ \quad (\text{C.3})$$

$$E_r = r_1 E_0 + it_1 E_1 \quad (\text{C.4})$$

Solving these equations algebraically for E_r and E_t in terms of the incident field E_0 , we find the transmission and reflectivity of the cavity:

$$t_c \equiv \frac{E_t}{E_0} = \frac{-t_1 t_2 \exp i\phi}{1 - r_1 r_2 \exp i2\phi} \quad (\text{C.5})$$

$$r_c \equiv \frac{E_r}{E_0} = \frac{r_1 - (r_1^2 + t_1^2) r_2 \exp i2\phi}{1 - r_1 r_2 \exp i2\phi} \quad (\text{C.6})$$

where $\phi = (2\pi/\lambda)L$ is the phase accumulated by the field as it travels from the first mirror to the second mirror. This phase depends on both the laser wavelength and the distance between the mirrors:¹

$$\phi = \pi(\nu/\nu_0) \quad (\text{C.7})$$

$$\nu_0 = c/(2L) \quad (\text{C.8})$$

where $\nu = c/\lambda$ is the laser frequency, L is the cavity length, and ν_0 is the *free spectral range*, which describes the spacing between adjacent resonances.

C.2 The Cavity Pole

It is often useful to write the cavity reflectivity in the form of a rational transfer function,

$$r_c(s) = \prod_{n=-\infty}^{\infty} \frac{s - z_n}{s - p_n} \quad (\text{C.9})$$

where $s = i\omega$, $\{z_n\}$ are the zeroes of $r_c(s)$, and $\{p_n\}$ are the poles. To find the poles and zeroes, make the substitution $\phi = -is/(2\nu_0)$ and solve for the zeroes of the numerator and denominator of equation C.6 separately. We find:

$$p_n = -\omega_{fsr} (\log(r_1 r_2) + in) \quad \forall n \in \mathbb{Z} \quad (\text{C.10})$$

$$z_n = +\omega_{fsr} (\log(r_1/r_2) + in) \quad \forall n \in \mathbb{Z} \quad (\text{C.11})$$

¹There is an additional contribution to the phase, the Guoy phase shift, due to geometric effects; this is described in chapter 4. Also note that some references use the *round-trip* phase rather than the *one-way* phase used here.

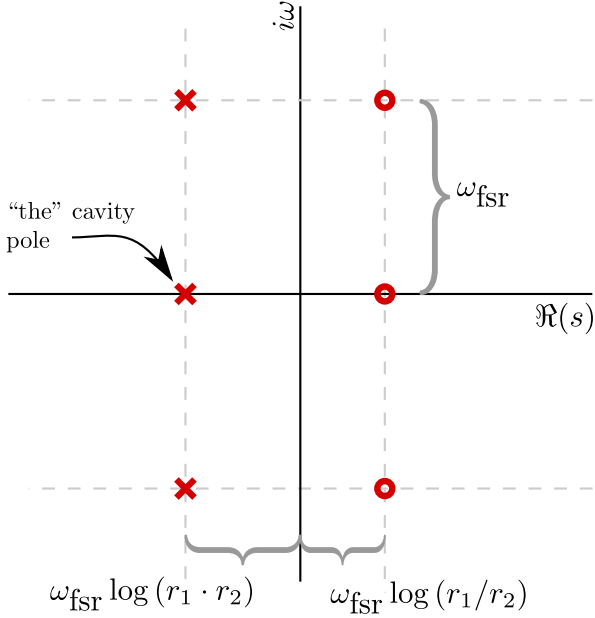


Figure C.2: Pole-zero map of the cavity amplitude reflectivity. Poles are designated with \times and zeros with \circ ; r_1 is the amplitude reflectivity of the input coupler, and r_2 is the amplitude reflectivity of the output coupler. Losses can be lumped into r_2 . Notice that the free spectral range (angular frequency ω_{fsr}) sets the scale of the entire diagram, and the function is periodic in $i\omega$: there is an infinite line of poles and an infinite line of zeros. Two limiting cases are worth considering: (1) A critically-coupled cavity has $r_1 = r_2$, which brings the line of zeros onto the imaginary axis. On resonance, $i\omega$ travels through these zeros and the cavity reflectivity vanishes. This models the desired behavior of mode cleaner cavities. (2) A maximally over-coupled cavity has $r_2 = 1$, in which case the line of poles and line of zeros are equally spaced from the imaginary axis. This models the LIGO arm cavities. The cavity's amplitude transmission has the same poles as the reflectivity but no zeros.

where $\omega_{\text{fsr}} \equiv 2\pi\nu_0$. The location of the poles and zeroes are illustrated in figure C.2.

Because this function is periodic in $i\omega$, we can in many circumstances regard the laser carrier as having a frequency $\nu = 0$ rather than $\nu = n\nu_0$ for some very large n .

C.3 Phase Gain

Our interest in using Fabry-Perot cavities as the arms of a gravitational wave detector is in having the light traverse the length of the arm multiple times, multiplying the effect of any optical path length perturbations caused by a GW. We can derive the magnitude of this *phase gain* by examining how the phase of the light reflected from the cavity changes as the intra-cavity phase ϕ changes, for small variations from resonance.

Suppose $z(t) = A(t) \exp\{i\phi(t)\}$ is an arbitrary complex-valued function with amplitude $A(t)$ and phase $\phi(t)$. By taking the logarithm before taking the derivative, we can separate the amplitude and phase:

$$\frac{\partial}{\partial t} \log z(t) = \left(\frac{\partial}{\partial t} \log A(t) \right) + i \left(\frac{\partial}{\partial t} \phi(t) \right) = \frac{1}{z(t)} \frac{\partial}{\partial t} z(t) \quad (\text{C.12})$$

This gives us an expression for the rate of change of the phase of a function:

$$\frac{\partial}{\partial t} \arg z(t) = \text{Im} \frac{1}{z(t)} \frac{\partial}{\partial t} z(t) \quad (\text{C.13})$$

We can find the phase gain of a Fabry-Perot cavity by applying this expression to the cavity reflectivity as a function of intra-cavity phase, $r_c(\phi)$:

$$g_\phi = \text{Im} \frac{r'_c}{r_c} \quad (\text{C.14})$$

where $r'_c(\phi) \equiv (1/2)(\partial/\partial\phi)r_c(\phi)$; the factor of 1/2 is to convert from round-trip phase to one-way phase. Because the derivative of the amplitude of r_c vanishes on resonance, we can simply take the magnitude of r'_c/r_c rather than the imaginary part. Explicitly taking the derivative of equation C.6, we find

$$r'_c(\phi) = \frac{1}{2} \frac{d}{d\phi} r_c(\phi) = -i \frac{(1 - r_1^2) r_2 \exp 2i\phi}{(1 - r_1 r_2 \exp 2i\phi)^2} \quad (\text{C.15})$$

Conventionally the symbol r'_c (as in [55]) indicates the magnitude of this expression at resonance ($\phi = 0$):

$$r'_c = \frac{(1 - r_1^2) r_2}{(1 - r_1 r_2)^2} \quad (\text{C.16})$$

Another way to calculate the phase gain is to use the rational transfer function expression, equation C.9. To model the situation near resonance, we need only consider the nearest pole and zero:

$$r_c(s) \approx \frac{s - z_0}{s - p_0} = \frac{s - \omega_{fsr} \log(r_1/r_2)}{s + \omega_{fsr} \log(r_1 \cdot r_2)}$$

Recall that the phase at frequency ω imparted by a pole at frequency ω_c is $\arctan(-\omega/\omega_c)$; a zero at the same frequency subtracts this same phase. For a maximally over-coupled cavity (i.e. with $r_2 = 1$), the cavity pole and cavity zero are equal and opposite, so contribute equal phase (\arctan is odd). Use $\omega = 2\nu_0\phi$ to express the detuning phase ϕ as an equivalent detuning frequency.

Changing the one-way phase of the arm by ϕ results in a phase change of

$$\phi_r = 2 \tan^{-1} \left(2\nu_0 \frac{\phi}{\omega_c} \right) \quad (\text{C.17})$$

where $\omega_c \equiv 2\pi f_c$ is the cavity pole and $\mathcal{F} = (1/2)(\nu_0/f_c)$ is the cavity finesse (which will be introduced in section C.5). Taking the derivative, we find the phase gain:

$$g_\phi = \frac{1}{2} \frac{d\phi_r}{d\phi} = \frac{2\nu_0}{\omega_c} \left[1 + \left(\frac{2\nu_0\phi}{\omega_c} \right)^2 \right]^{-1} = \frac{2\mathcal{F}}{\pi} \left[1 + \left(\frac{\omega}{\omega_c} \right)^2 \right]^{-1} \quad (\text{C.18})$$

The phase gain on resonance is $2\nu_0/\omega_c = 2\mathcal{F}/\pi \approx 140$. This phase gain decreases as we detune the cavity further from resonance, but it is not seriously diminished until the cavity detuning approaches the cavity pole.

C.4 Intra-Cavity Power Buildup

The power buildup in the cavity is given by

$$\frac{P_+}{P_{IN}} = \frac{|E_+|^2}{|E_0|^2} = \frac{T_1}{1 - 2r_1r_2 \cos 2\phi + (r_1r_2)^2} \quad (\text{C.19})$$

which may be re-written (using the identity $\cos 2\phi = 1 - 2\sin^2 \phi$) as

$$\frac{P_+}{P_{IN}} = \frac{g^2}{1 + F \sin^2 \phi} \quad \text{with } F = \frac{4r_1r_2}{(1 - r_1r_2)^2} \quad \text{and } g = \frac{t_1}{1 - r_1r_2} \quad (\text{C.20})$$

where F is the *coefficient of finesse* and g is the *amplitude gain*.

The form of this expression is often referred to in the literature as an Airy function, though it is distinct from the well-known special function of the same name. Making the small angle approximation $\sin \phi \approx \phi$ we see that each resonance is locally Lorentzian.

C.5 Finesse (\mathcal{F})

The tightness of the resonance is quantified as the *finesse* (\mathcal{F}), which is defined as the ratio of the cavity free spectral range to the full-width-half-max of the resonance,

$$\mathcal{F} \equiv \frac{\nu_0}{\nu_{\text{FWHM}}} = \frac{1}{2} \frac{\nu_0}{f_c} \quad (\text{C.21})$$

where the FWHM is given by twice the cavity pole (f_c). The finesse is related to the coefficient of finesse (F) by

$$\mathcal{F} = \frac{\pi}{2} \frac{1}{\sqrt{\arcsin(1/F)}} \approx \frac{\pi}{2} \sqrt{F} \quad (\text{C.22})$$

where the approximation holds for high-finesse cavities.

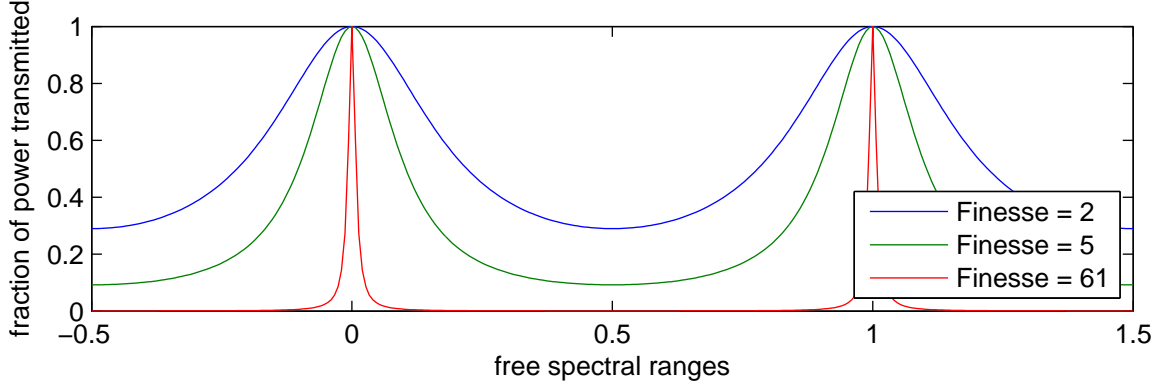


Figure C.3: Power transmission coefficients for three critically-coupled cavities.

The finesse (\mathcal{F}) of an optical cavity is analogous to the quality factor (Q) of an oscillator. The Q factor is the ratio of the frequency of an oscillator to its full-width-half-max bandwidth; to compute finesse, the free spectral range (spacing between resonances) is used instead of the oscillator frequency.

C.6 Impedance Matching

From the point of view of a beam incident upon a cavity, the cavity is either under coupled, critically coupled, or over coupled. This coupling is determined by the comparison of the transmissivity of the input coupler compared to all other losses in the system. For a two-mirror, lossless cavity, the cavity is under coupled if $t_1 < t_2$, critically coupled if $t_1 = t_2$, and over coupled if $t_1 > t_2$.

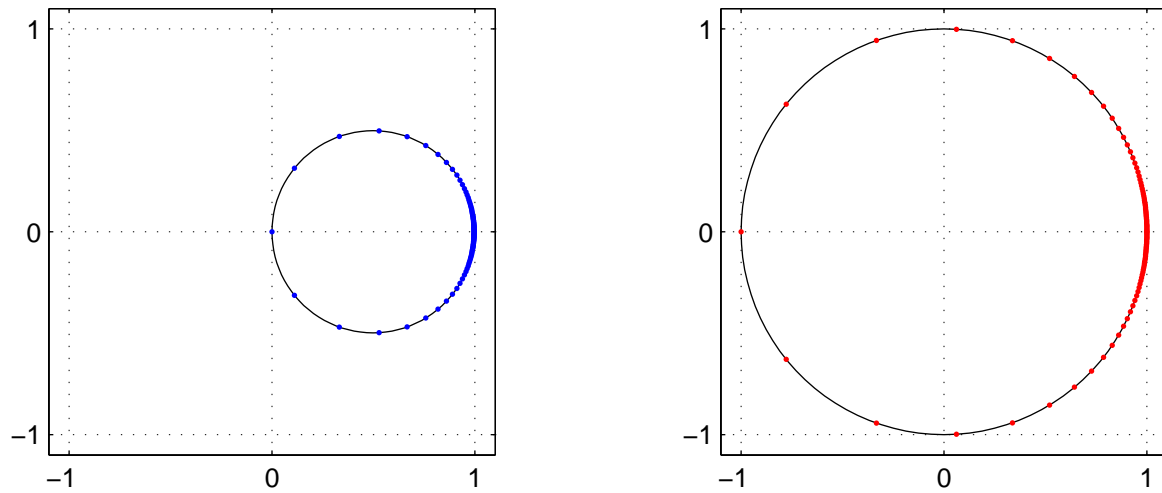
C.6.1 Critically-Coupled Cavities

Maximum power is transferred into a critically coupled cavity; no power is reflected. In this case, the prompt reflection from the input coupler is exactly canceled by an equal-amplitude, opposite-phase leakage beam from the field inside the cavity. Because an (ideal) critically coupled resonator is perfectly transmissive for light at the resonant frequency, they are used as filter cavities.

The transmission of power through a filter cavity may be found by multiplying equation ?? by the output coupler power transmissivity $T = t_1^2 = t_2^2$:

$$T_c = \frac{1}{1 + F \sin^2 \phi} = \begin{cases} 1 & \text{at resonance (maximum transmission)} \\ 1/(1 + F) & \text{at anti-resonance (minimum transmission)} \end{cases} \quad (\text{C.23})$$

where we see that the (coefficient of) finesse quantifies the attenuation of non-resonant modes (in addition to the width of the resonance).



(a) Critically coupled cavity. Note that $r = 0$ on resonance. Cavities of this type are used as filter cavities.

(b) Maximally over-coupled cavity. Note that $r = -1$ on resonance. Cavities of this type are used for the LIGO arms.

Figure C.4: Reflection coefficients for two cavities, plotted on the complex plane, over a free spectral range $0 \leq \phi < \pi$. The x axis represents the real part, and the y axis the imaginary part of the cavity reflection coefficient. The dots are spaced with uniform $\Delta\phi$. They appear more closely spaced when the phase of the cavity reflectivity changes slowly; they appear sparsely spaced where the reflected phase changes quickly, as the cavity goes through resonance.

The power buildup inside a critically-coupled two-mirror cavity is simply the inverse of the mirror transmission:

$$g^2 = \left(\frac{t_1}{1 - r_1 r_2} \right)^2 = \frac{t^2}{(1 - r^2)^2} = \frac{1}{T}$$

This can also be seen from a very simple argument: if the power emerging from the output coupler is equal to P_{IN} , then the power inside the cavity must be P_{IN}/T .

C.6.2 Over-Coupled Cavities

The LIGO arms are strongly over-coupled cavities. A lossless maximally over-coupled cavity (i.e. with $t_2 = 0$) acts as a perfect reflector.

For high-finesse, highly-overcoupled cavities, the cavity power buildup g^2 is approximately equal to the square root of the coefficient of finesse, or $(2/\pi)$ times the finesse:

$$g^2 \approx \sqrt{F} \approx \frac{2}{\pi} \mathcal{F} \quad (\text{C.24})$$

This can be seen by setting $r_2 = 1$ and using $\sqrt{x} \approx 1 + (x - 1)/2$ for $x \approx 1$:

$$g^2 \Big|_{r_2 \rightarrow 1} = \frac{1 - r_1^2}{(1 - r_1)^2} = \frac{1 + r_1}{1 - r_1} \approx \frac{2\sqrt{r_1}}{1 - r_1} = \sqrt{F} \Big|_{r_2 \rightarrow 1} \quad (\text{C.25})$$

Another useful approximation is:

$$g^2 \approx \frac{4}{T_1}$$

Appendix D

The Optical Spring

When detuned from resonance, the power circulating within a Fabry-Perot cavity varies linearly with small deviations from that detuning. This gives rise to a displacement-dependent force, which can be described via a spring constant. This effect is called the *optical spring*¹. Optical springs has been observed and studied in several experiments [93].

For frequencies that are slow compared to the cavity pole, we can calculate the behavior of the spring using a quasi-static approximation, simply using the derivative of the power buildup versus cavity detuning.

The power circulating in a cavity is:

$$\frac{P_+}{P_{IN}} = \frac{g^2}{1 + F \sin^2 \phi} \quad (\text{D.1})$$

where P_{IN} is the incident power, P_+ is the forward-circulating power, $g^2 = (t_1)^2 / (1 - r_1 r_2)$ is the power buildup on resonance, $F = 4r_1 r_2 / (1 - r_1 r_2)^2$ is the coefficient of finesse², and ϕ is the one-way phase detuning of the cavity, which is related to cavity length x as $\phi = (2\pi/\lambda)x$.

For a given power circulating in the cavity, the radiation pressure force due to the intra-cavity power on each of the mirrors is $f = 2P/c$. We can find the spring constant by taking the derivative:

$$k \equiv -\frac{\partial f}{\partial x} = -\frac{\partial}{\partial x} \frac{2P}{c} = -\frac{2}{c} \frac{\partial \phi}{\partial x} \frac{\partial P}{\partial \phi}$$

Working out the derivative, we find:

¹This is the longitudinal optical spring; an *angular* optical spring also arises, due to interactions between off-center radiation pressure and cavity geometry [45].

²The finesse (\mathcal{F}) is related to the coefficient of finesse (F) via $\mathcal{F} \approx \frac{\pi}{2}\sqrt{F}$.

$$\frac{\partial}{\partial \phi} P_+ = -2Fg^2 \frac{\cos(\phi) \sin(\phi)}{(1 + F \sin^2 \phi)^2} P_{IN} \quad (\text{D.2})$$

$$= -2Fg^2 P_{IN} \phi + O(\phi^3) \quad (\text{D.3})$$

Putting it all together, we get:

$$k = 2Fg^2 \left(\frac{2P_{IN}}{c} \right) \left(\frac{2\pi}{\lambda} \right) \frac{\cos(\phi) \sin(\phi)}{(1 + F \sin^2 \phi)^2} \quad (\text{D.4})$$

$$\approx 2Fg^2 \left(\frac{2P_{IN}}{c} \right) \left(\frac{2\pi}{\lambda} \right) \frac{\phi}{(1 + F\phi^2)^2} \quad (\text{D.5})$$

$$\approx 2Fg^2 \left(\frac{2P_{IN}}{c} \right) \left(\frac{2\pi}{\lambda} \right) \phi + O(\phi^3) \quad (\text{D.6})$$

where, of course, $\phi = (2\pi/\lambda)\delta x$, where x is the (one-way) detuning length. If a mirror is displaced by (δx) , the spring constant is:

$$k \approx \frac{64\mathcal{F}^2 g^2 P_{IN}}{c\lambda^2} (\delta x)$$

Putting in some numbers for the Enhanced LIGO arms:

$$\begin{aligned} \mathcal{F} &= 220 \\ g^2 &= 137 \\ P_{IN} &= 400 \text{ Watts} \\ \lambda &= 1064 \text{ nm} \\ \hline \delta x &= 5 \text{ pm} \\ k &\approx 2500 \text{ N/m} \end{aligned}$$

For comparison, the mechanical restoring force has a spring constant of approximately

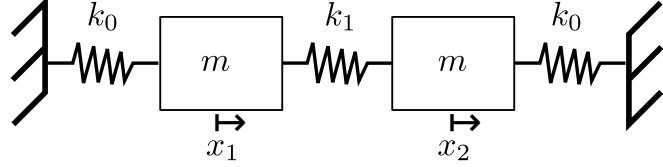
$$k_m = m\omega^2 \approx (10.5 \text{ kg}) (2\pi \cdot 0.75 \text{ Hz})^2 \approx 230 \frac{\text{N}}{\text{m}}$$

It can also be handy to put Eq. D.5 into terms of the unitless detuning parameter $\delta_\gamma = \sqrt{F}\phi$, where $\delta_\gamma \equiv \frac{\delta}{\gamma}$, where δ is the cavity detuning (in radians/sec), and γ is the line-width (cavity pole) in the same units. If we further assume that the cavity is strongly-overcoupled, we can use the relations $g^2 = \sqrt{F} = \frac{2}{\pi}\mathcal{F} = 4/T_1$. With these substitutions (and $\lambda = 2\pi c/w_0$), we recover expression (3.14) given in Thomas Corbitt's thesis [94]:

$$K_0 \approx \frac{64P_{IN}w_0}{T^2 c^2} \frac{\delta_\gamma}{(1 + \delta_\gamma^2)^2} \quad (\text{D.7})$$

Coupled oscillators

Consider a system of two masses, connected to each other via a spring with spring constant k_1 and each connected to the wall via a spring of spring constant k_0 . (Later, k_0 will represent the pendula by which the optics are suspended, and k_1 will represent the optical spring.)



By inspection, the equations of motion are:

$$m\ddot{x}_1 = -k_0x_1 + k_1(x_2 - x_1) \quad (\text{D.8})$$

$$m\ddot{x}_2 = -k_0x_2 - k_1(x_2 - x_1) \quad (\text{D.9})$$

which may be written in matrix form as

$$\ddot{\mathbf{x}} = \frac{1}{m} \begin{bmatrix} -(k_0 + k_1) & k_1 \\ k_1 & -(k_0 + k_1) \end{bmatrix} \mathbf{x} \quad (\text{D.10})$$

Because of the form of the matrix³, we can immediately see that it has eigenvectors corresponding to common and differential motion, with eigenvalues $\{-k_0, -(k_0 + 2k_1)\}$.

Applying this diagonalization, we find:

$$\ddot{\mathbf{x}}' = \frac{1}{m} \begin{bmatrix} -k_0 & 0 \\ 0 & -(k_0 + 2k_1) \end{bmatrix} \mathbf{x}' \text{ where } \mathbf{x}' = \begin{bmatrix} 1 & 1 \\ 1 & -1 \end{bmatrix} \mathbf{x}$$

The presence of the coupling k_1 only affects the differential mode.

The mechanical (force to position) transfer function of the differential mode of a detuned resonant cavity is shown in figure D.1, both using the analytic formulism developed above and using a numerical model implemented with Optickle.

³The matrix $\begin{bmatrix} a & b \\ b & a \end{bmatrix}$ has eigenvectors $\begin{pmatrix} 1 \\ 1 \end{pmatrix}$ and $\begin{pmatrix} 1 \\ -1 \end{pmatrix}$ with eigenvalues $(a+b)$ and $(a-b)$.

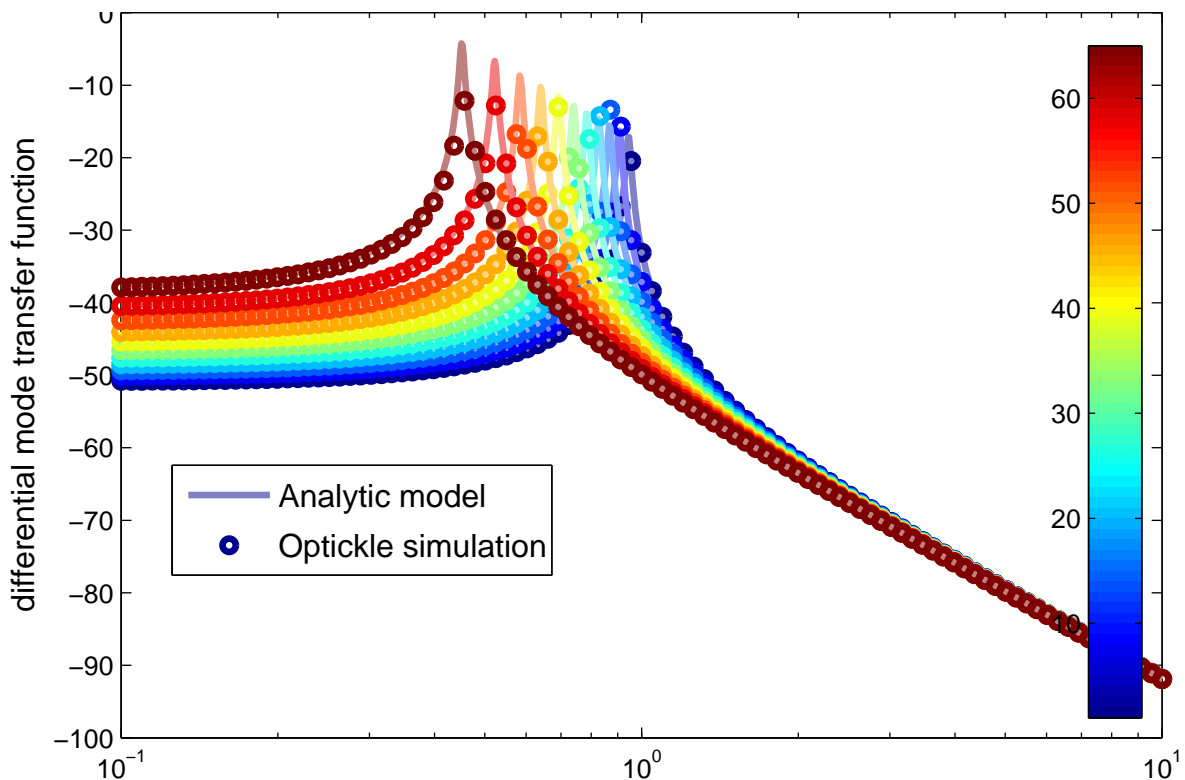


Figure D.1: The optical spring effect: As a cavity is detuned from resonance, the resonance of the differential mode deceases. This figure compares the results of a numerical (Optickle) model with analytic results. The units of the y-axis are $20 \log_{10}(\text{displacement}/\text{force})$; the x-axis is Hz; color indicates cavity detuning in picometers.

Appendix E

Additional Notes

E.1 The Jacobi-Anger Identity

Taking the generating function of the Bessel functions

$$\exp\left\{\frac{1}{2}z(t - t^{-1})\right\} = \sum_{m=-\infty}^{\infty} t^m J_m(z) \quad (\text{E.1})$$

we can make the substitution $t = \exp\{i\omega t'\}$. This gives the Jacobi-Anger expansions, which are useful for expanding sinusoidal phase modulation in terms of sidebands around the carrier:

$$e^{i\Gamma \cos \Omega t} = \sum_{n=-\infty}^{\infty} (i^n) J_n(\Gamma) \exp\{in\Omega t\} \quad (\text{E.2})$$

$$e^{i\Gamma \sin \Omega t} = \sum_{n=-\infty}^{\infty} J_n(\Gamma) \exp\{in\Omega t\} \quad (\text{E.3})$$

E.2 Comparison of Phase Modulation (PM) and Amplitude Modulation AM)

Suppose we have a signal consisting of a carrier (at frequency ω and with unit amplitude) and two sidebands, of amplitudes a (lower) and b (upper), separated from the carrier by a frequency Ω :

$$E(t) = (1 + a \exp(-i\Omega t) + b \exp(i\Omega t)) \exp(i\omega t) \quad (\text{E.4})$$

To find the power in this signal, we take the modulus squared, $P = E^*E$ where $*$ is the complex conjugate:

$$\begin{aligned} P &= (1 + |a|^2 + |b|^2) \\ &\quad + (a^* + b) \exp(-i\Omega t) + (a + b^*) \exp(i\Omega t) \\ &\quad + (ab^*) \exp(-2i\Omega t) + (a^*b) \exp(2i\Omega t) \end{aligned} \quad (\text{E.5})$$

The condition for the 1Ω variation in the power to vanish is $a = -b^*$, i.e. the real parts of the amplitudes of the sidebands must be opposite, and the imaginary parts must be equal. So we can extract the amplitude and phase modulation indices:

$$\begin{aligned} m_{AM} &= (a + b^*) \\ m_{PM} &= (a - b^*) \end{aligned} \quad (\text{E.6})$$

What is the condition for the 2Ω signal to vanish? With just two sidebands, it will always be present (though at second order in the sideband amplitude). In true phase modulation, the 2Ω signal is cancelled by the interaction of (the infinite number of) higher-order sidebands. As best I can tell, there is no simple arrangement of this cancellation other than via a magical property of the Bessel functions.

E.3 Comparison of Phase Modulation (PM) and Frequency Modulation (FM)

There is not really any difference between phase modulation and frequency modulation. Frequency modulation with modulation depth m_{FM} [Hz] at a frequency f [Hz] has the form

$$y(t) = \exp\{i\omega t\} \exp\left\{i \int_0^t 2\pi m_{FM} \Re\left\{e^{i2\pi ft'}\right\} dt'\right\} \quad (\text{E.7})$$

where ω [radians/second] is the carrier frequency. We can simply do the integral and get:

$$y(t) = \exp\{i\omega t\} \exp\left\{i \frac{1}{f} m_{FM} \Re\left\{ie^{i2\pi ft}\right\}\right\} \quad (\text{E.8})$$

which is just phase modulation at frequency f [Hz] with modulation depth $(i/f)m_{FM}$ (in radians). The relation between phase modulation and frequency modulation is therefore:

$$m_{PM} = \left(\frac{i}{f}\right) m_{FM}$$

The i signifies a phase shift of 90 degrees in the modulation (turning cos to sin).

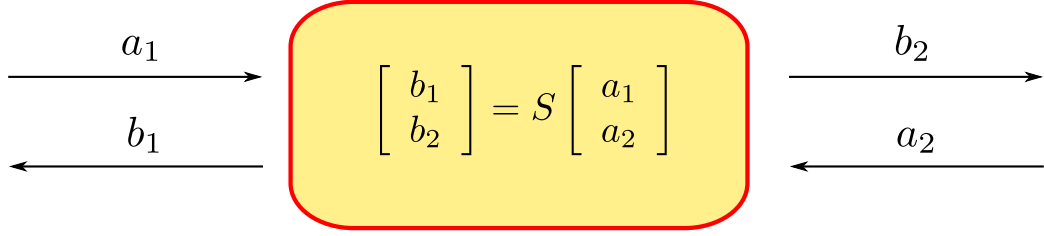


Figure E.1: The scattering matrix S gives the amplitudes of the outgoing fields b_1 and b_2 in terms of the in-going fields a_1 and a_2 .

E.4 Calibration

The calibration of the LIGO interferometers into real units (of mirror displacement or gravitational wave strain) during Initial LIGO is described in [95]; the Enhanced LIGO procedure was essentially the same. An alternate calibration procedure using radiation pressure is described in [96].

E.5 Only the Signal Field Matters

Suppose we have two electric fields incident on a photodiode: the signal field A_s and the local oscillator field A_{LO} . The power seen by the photodiode is

$$|A_s + A_{LO}|^2 = |A_s|^2 + |A_{LO}|^2 + 2\text{Re}A_s^*A_{LO}$$

In the small-signal regime, $|A_s| \ll |A_{LO}|$. The signal on the photodiode is proportional to $A_s A_{LO}$ while the shot noise is proportional to $\sqrt{|A_s|^2 + |A_{LO}|^2} \approx A_{LO}$. The detected SNR is independent of the local oscillator strength.

E.6 Optical Phase Conventions

In writing down the relationships between optical field amplitudes upon reflection from or transmission through a mirror, we must first choose a phase convention. What happens to the phase of the field upon reflection? Upon transmission? For a real mirror, made up of many layers of dielectric coating on both sides of a thick substrate, and given particular reference points at which to compute the fields, the phases upon reflection and transmission depend on all of this structure. But for tractability, and for no real loss of modeling fidelity, we can discard the particulars as unknown ‘microscopic phase’ and adopt instead an idealized model of a mirror that has the right power reflectivity and transmission and does not violate conservation of energy. There are two such conventions in common use. We can call them the “engineers’ convention” and the “physicists’ convention.”

The complex reflection and transmission coefficients are encoded in the S-matrix, which

gives the amplitudes of the fields going *out* of some optical element in terms of the fields going *in* (depicted in figure E.1).

In the physics convention, transmission through a mirror conveys no phase; reflection from one direction is real and positive ($+r$), but reflection from the other direction gives a minus sign ($-r$). The physics convention essentially models a mirror as a single dielectric boundary. The S-matrix for the physics convention is:

$$S_{\text{physics}} = \begin{pmatrix} -r & t \\ t & r \end{pmatrix} \quad (\text{E.9})$$

In the engineering convention, reflection from either side of a mirror has the same real, positive reflectivity ($+r$), but transmission through the mirror gives a phase of 90 degrees, a coefficient of it , giving an S -matrix of:

$$S_{\text{engineering}} = \begin{pmatrix} r & it \\ it & r \end{pmatrix} \quad (\text{E.10})$$

The (initial) LIGO test masses actually have amplitude reflectivity coefficients close to -1 at the high-reflectivity (HR) side, so that the electric field on the surface of the optic on the high-power side is very near zero.

E.7 Gaussian Beams

The general picture of Gaussian beams is shown here:

It is convenient to introduce the complex beam parameter q . In terms of q :

$$\frac{1}{q(z)} = \frac{1}{R(z)} - i \frac{\lambda}{\pi w^2(z)} \quad (\text{E.11})$$

where $R(z)$ is the radius of curvature of the phase fronts at a position z along the optical axis, and $w(z)$ is the spot size at that location. We can also write: $q(z) = iz_R + (z - z_0)$.

For a mode to resonate in an optical cavity, the spherical surface of the mirrors must match the spherical phase front of the beam at the location of the mirror.

Suppose mirror 1 has curvature R_1 and coordinate z_1 , and similarly for mirror 2. We would like to solve for the waist location and Rayleigh range.

References: Kogelnik and Li [97], Siegman [90], [98, 91].

E.8 Laser Modes

The eigenmodes of an optical cavity formed from spherical lenses are the Hermite-Gauss (if the cavity has rectangular symmetry) or Laguerre-Gauss (for axial symmetry) modes. The amplitude distribution at the beam waist is a Gaussian multiplied by a Hermite or

Laguerre polynomial. These are exactly the same families of functions as the energy eigenstate wavefunctions of the simple harmonic oscillator in quantum mechanics.

E.9 Shot Noise

The root-mean-square of a Poisson process with current I and quantum q measured over a bandwidth of Δf is

$$\sigma = \sqrt{2qI\Delta f}$$

Here I could be the electric current in Amps (=Coulombs/second) and q the charge of an electron. For light incident on a photodiode, the photon shot noise can be considered as an energy current, with $I \leftarrow P$ being the DC power, and $q \leftarrow h\nu$ being the energy per photon.

The amplitude spectral density of this process is white, with amplitude $\sqrt{2qI}$ in units of [I] per square root of Hz. For power P , the shot noise amplitude spectral density is

$$\text{shot noise ASD} = \sqrt{2h\nu P} \quad [\text{Watts}/\sqrt{\text{Hz}}] \quad (\text{E.12})$$

which gives a relative intensity noise of $\sqrt{2h\nu/P}$.

Vita

Tobin Fricke was born in Los Angeles, California in 1980 to Oscar and Julie Fricke. After graduating from Mission Viejo High School in 1998, he studied electrical engineering and computer science (EECS) and mathematics at the University of California, Berkeley and physics at the University of Rochester. Following his doctoral work at Louisiana State University, Tobin will begin an appointment at the Max Planck Institute for Gravitational Physics in Hannover, Germany.